

Modeling of Strain Effects in Multi-component Semiconductors

By

Mehrdad Arjmand

A dissertation submitted in partial fulfillment of

the requirements for the degree of

Doctor of Philosophy
(Engineering Mechanics)

at the

University of Wisconsin- Madison

2017

Date of final oral examination: 10/27/2016

The dissertation is approved by the following members of the Final Oral Committee:

Susan Babcock, Professor, Materials Science and Engineering

Walter Drugan, Professor, Engineering Mechanics

Dane Morgan, Professor, Materials Science and Engineering

Donald Stone, Professor, Materials Science and Engineering

Izabela Szlufarska, Professor, Materials Science and Engineering

Modeling of strain effects in multi-component semiconductors

Mehrdad Arjmand

Under supervision of Prof. Izabela Szlufarska

At the University of Wisconsin-Madison

Abstract

Strain affects the properties of crystalline material by changing the atomic symmetry. Controlling the strain in semiconductors helps to tune properties of material and design new material. For instance, strained semiconductor heterostructures have improved the efficiency of traditional solar cells remarkably. Another example of strain application is in electronic devices. Strained heterostructure nanowires provide a better control on electronic properties of gates used in transistors. Gate-all-around nanowires are promising candidates to power microprocessors in future. Strain is also used to make quantum dot structures from semiconductors. These quantum dots are used in quantum computing, diode lasers and sensors.

Once the stored strain in a structure reaches a critical limit, it relaxes by triggering different phenomena in the structure. For instance, strain causes morphology change, plastic deformation, phase separation and intermixing, fracture, buckling, bulging and peeling. In order to use these strained structures for design purposes, it is critical to understand these different relaxation phenomena and be able to control them.

Modeling provides a powerful framework to understand different relaxation mechanisms and provide guidance to control these strain induced phenomena. In this thesis, I have developed a continuum based model called “phase field” to study morphology change, plastic deformation and phase separation in multi-component semiconductors during growth and annealing processes. The advantage of phase field approach compared to some other modeling techniques is that it

includes the effects of both thermodynamics and kinetics. Also, I have developed a continuum based elasto-plasticity model to study the effects of plastic relaxation in semiconductor nanowires. This model can particularly be useful for piezoelectric and surface stability analysis of nanowires.

Acknowledgement

I would like to thank my advisor, Prof. Szlufarska for giving me the opportunity to join her group. I am grateful for her kind support, guidance and confidence in me over the past 5 years. In these years, I learned how to conduct research, collaborate with other researchers and also grew in different aspects of life. I am thankful to her for sending me to different conferences and workshops across the country. I achieved speaking experience, self-confidence and networking skills. Foremost, I would like to thank Prof. Szlufarska for her support beyond the school work to help me pursue my dreams and achieve my goals in life.

Many thanks to the current and former members of Computational Materials Group who made a lot of good memories in my mind. Special thanks to Prof. Morgan for several useful discussions and for his constructive suggestions over these years. I need to thank Drs. Deng, Swaminathan, Young and Luo for their knowledge and help.

I am grateful to National Science Foundation and University of Wisconsin Materials Research Science and Engineering Center (MRSEC) for their support (DMR-1121288). Also, I am thankful to MRSEC for providing me with many outreach opportunities, personal development workshops and seminars, industry interactions and valuable leadership experience. I would like to thank Profs. Kuech, Babcock and Mawst for their guidance. Finally, I would like to thank my friend, Dr. Forghani for his encouragement both in research and personal life.

I would like to thank the other members on my thesis committee, Profs. Drugan, Plesha and Stone. Specially, I am grateful to Prof. Drugan from whom I learned a lot about mechanics. I appreciate his patience for bearing with my numerous questions both in and outside the class.

Many thanks to my friends all around the world who supported me in these years. More specifically, I need to thank my friends in Madison who helped me to go through this journey and enjoy this chapter of my life. Looking back in time, I remember spending numerous days, evenings and weekends studying and discussing science with my great friend, Chandler Benjamin

and those moments are considered among the best occasions of my journey as a graduate student. I want to express my deep gratitude, honor and respect to my best friend in life, Ali Bastani who was always there for me as a friend, but unfortunately passed away during my studies. I am sure he would be delighted if he could see my graduation!

Finally, I would like to acknowledge my father, my mother and my two brothers for their unconditional love, encouragement and support. Their presence provides meaning to my life! I would like to thank my lovely brothers, Masoud and Mehran for always being there. I am proud of you brothers! Lastly, I would like to deeply appreciate sincere prayers of my parents that always gives me hope, encouragement and assurance, even though they are living in the other side of the planet.

Table of Contents

Abstract	i
Acknowledgement	iii
List of Figures	viii
List of Tables	xv
Chapter 1 Introduction	1
1.1 Motivation.....	1
1.2 Scope of the thesis.....	8
1.3 Organization of this document.....	9
1.4 Reference	12
Chapter 2 Background	14
2.1 Semiconductors and their applications.....	14
2.2 Defects in semiconductors	15
2.2.1 Point defects (zero dimensional).....	15
2.2.2 Extended defects	18
2.3 Heteroepitaxy	19
2.4 Strain-related phenomenon in growth of semiconductor heterostructures.....	21
2.4.1 Elastic relaxation (morphology change)	21
2.4.2 Plastic relaxation.....	23
2.4.3 Phase separation / intermixing	25
2.4.4 Fracture	26
2.5 Film deposition techniques	28

2.5.1 Physical vapor deposition	28
2.5.2 Chemical vapor deposition	30
2.6 Simulation methods to study growth and annealing of semiconductor heterostructures	31
2.7 Reference	36
Chapter 3 Method	38
3.1 Phase field method.....	38
3.2 Numerical methods to solve governing equations	50
3.2.1 Finite difference method.....	50
3.2.2 Finite element method	53
3.3 Reference	61
Chapter 4 Effects of confinements on morphology of $\text{In}_x\text{Ga}_{1-x}\text{As}$ thin film grown on sub-	
micron patterned GaAs substrate: elastoplastic phase field model	63
4.1 Abstract.....	63
4.2 Introduction.....	64
4.3 Elastoplastic phase field model.....	70
4.4 Results.....	80
4.4.1 Low indium concentration $\text{In}_x\text{Ga}_{1-x}\text{As}/\text{GaAs}$ ($x < 0.4$)	81
4.4.2 High indium concentration $\text{In}_x\text{Ga}_{1-x}\text{As}$ ($x > 0.4$)	88
4.5 Conclusions.....	98
4.6 Reference	100
Chapter 5 Control of surface induced phase separation in immiscible semiconductor alloy	
core-shell nanowires	104
5.1 Abstract.....	104
5.2 Introduction.....	104

5.3 Model	105
5.4 Results	112
5.5 Summary and conclusions	123
5.6 References	124
Chapter 6 Analytical elastoplastic analysis of heteroepitaxial core-shell nanowires	126
6.1 Abstract	126
6.2 Introduction	126
6.3 Model	129
6.4 Results	137
6.5 Conclusions	152
6.6 Reference	153
Chapter 7 Concluding remarks and future directions.....	155
7.1 Implication of modeling on growth and annealing of heterostructures	155
7.2 Possible improvements in future modeling efforts	155
7.3 Papers and manuscripts	157
7.4 Conference presentations	157
7.4.1 Oral presentations	157
7.4.2 Poster presentations	158

List of Figures

- Fig. 1.1 a) Homoepitaxy: film and substrate have the same lattice parameter at equilibrium. No strain is stored in the film. b) Heteroepitaxy: film and substrate have different lattice parameters at equilibrium and hence the structure is strained..... 2
- Fig. 1.2 a) Lattice parameter for three different material: A, B and C. Lattice parameter for A and B are equal, but lattice parameter of C is larger than lattice parameter of A and B. b) Volmer-Weber or island growth mode. c) Frank Van der Merwe or layer-by-layer growth mode. d) Stranski-Krastanov or mixed epitaxial growth mode. Material C is under strain due to lattice mismatch with the substrate. 4
- Fig. 1.3 a) Lattice parameter for four different material: A, B, C and D are shown where $a_A < a_B < a_C < a_D$. Different Relaxation mechanisms for heteroepitaxial thin films: b) Elastic relaxation of the film by morphological changes at the surface. c) Plastic relaxation of thin film due to misfit strain. This type of deformation usually starts at the interface. d) Surface induced phase separation. e) Crack formation in the film under tensile strain. 7
- Fig. 2.1 Schematic representation of the incorporation of extrinsic point defect Si (green) for Ga (blue) and As (red) in GaAs. Elastic strain introduces by the impurity is not shown in this schematic picture..... 16
- Fig. 2.2 Formation of vacancies in Ga (V_{Ga}) and As (V_{As}) sites. 17
- Fig. 2.3 Formation of Ga_{As} and As_{Ga} anti-sites in GaAs structure..... 17
- Fig. 2.4 Plot of bandgap as a function of the lattice parameter of common semiconductors (red dots). Solid black lines between each two dot show the alloy that can have specific bandgap based on the lattice parameter of the alloy. The areas between three or more dot represent compound alloys of more than three materials. The green dashed line represent the lattice

- parameter of commercially available substrates. Courtesy of Prof. Thomas Kuech from University of Wisconsin – Madison..... 19
- Fig. 2.5 a) Heteroepitaxial growth: film and substrate have different lattice parameters a_{film} and $a_{\text{substrate}}$. b) Coherent growth of thin film on substrate (pseudomorphic growth). c) Incoherent growth of thin film on substrate due to formation of misfit dislocations at the film/substrate interface..... 20
- Fig. 2.6 a) Relaxed heterostructure. b) Strained heterostructure. c) Film with a square wave surface profile. The surface profile has wavelength of λ and magnitude of c 22
- Fig. 2.7 Critical thickness for SiGe/Si. Curves 1 and 2 represent critical thicknesses for 90° and 60° dislocations and curve 3 represents experimental observations. The figure is taken from [10]..... 24
- Fig. 2.8 Graphical summary of the predictions for films under tensile strain [19,20]. The graph shows misfit strain as a function of film thickness. Above line A, crack propagates. Above line B, film fractures spontaneously. Below line C, it is energetically favorable for the film to elastically relax. Dashed line shows relaxation critical thickness..... 27
- Fig. 2.9 Schematic view of evaporative PVD growth. The chamber is usually under high vacuum. A physical process is used to produce vapor from solid source of material. Material vapor is then deposited on substrate. 29
- Fig. 2.10 Schematic view of CVD growth. The chamber is under vacuum. Reactant gases flow into the chamber and products leave the chamber after the reaction is done at the surface. The reaction at the surface produces the desired deposit. 30
- Fig. 2.11 a) Schematic view of different sub-domains inside the main domain. For evolution problems, in addition to solving governing equations in each sub-domain, boundary conditions between all sub-domains (such as displacement field, traction vector, etc.) are

needed at each time step to track the boundaries. b) Schematic view of sharp transition of a variable at an interface from 0 to 1. 33

Fig. 3.1 a) Phase field variables: constant values inside a domain, continuous transition at the interfaces. b) Schematic view of transition of a phase field variable at an interface from 0 to 1..... 39

Fig. 3.2 Phase transformation from cubic to tetragonal structure. Since tetragonal structure has three different orientations that are energetically equivalent, three order parameters (η_1 , η_2 and η_3) are needed to model the transformation. a_c , a_t and c_t are lattice parameters of cubic and tetragonal structure [19]. 40

Fig. 3.3 a) Bulk free energy density as a function of molar fraction (x). There are two minima at x_B^{a1} and x_B^{a2} where a common tangent between those minima represents the energy of stable phases in between these two minima. b) Bulk free energy density as a function of order parameter (η) with minima at $\eta = \pm 1$ [19]..... 42

Fig. 3.4 Double-welled free energy density function [9]. This free energy density function describes a case where there are two thermodynamically stable phases at $\varphi=0$ and $\varphi=1$. The barrier height of free energy functional $W/64$ is calculated from interfacial thickness and interfacial energy as shown in Eqs. (3-12) and (3-13). 44

Fig. 3.5 Meshing is a process of dividing a domain in small elements where there are grid points at the corners of each element. h_i and h_j show the length of each element in x and y directions. $U(i,j)$ represents the value of function U at grid point (i,j) 51

Fig. 3.6 a) 2D domain of variable $\varphi(x,y)$ with a 3-node mesh. ϕ_1 , ϕ_2 and ϕ_3 are nodal values of the variable φ . b) Elements with different sizes can be used in the same domain. To solve the problem, one needs to fully populate the domain with elements. 54

Fig. 3.7 Triangular elements: a) 3-node element with a linear interpolation function. b) 6-node element with a quadratic interpolation function. c) 10-node element with a cubic

interpolation function. Interpolation functions with higher orders provide higher accuracy to numerical approximations. 56

Fig. 3.8 a) An arbitrary point P is chosen inside the element. By connecting point P to the corners of the element, three subdomains are formed. A_1 , A_2 and A_3 are the areas of these triangular subdomains. L_2 is the ratio between A_2 and A (total area of element). L_2 is zero when point P is chosen on the line that connects corners 1 and 3. L_2 is one when point P is chosen at corner 2. b) L_2 has three values in this element. $L_2=0$, $L_2=0.5$, and $L_2=1$. c) L_2 has four values in this element. $L_2=0$, $L_2=0.5$, and $L_2=1$ 57

Fig. 4.1 a) Schematic cross-sectional view of the patterned substrate showing deposition flux non-uniformity. The distance between two walls is $0.5 \mu\text{m}$. Width of SiO_2 pattern is also $0.5 \mu\text{m}$ but is not plotted to scale b) Boundaries in the simulation domain: b1 (the lower boundary of the substrate), b2 and b3 (outer boundaries of the wall and the substrate), b4 (outer/top boundary of the gas phase region), b5 (substrate/film interface), b6 and b7 (interface between wall and film/gas). The coordinate system originates at the interface between film and the substrate. 71

Fig. 4.2 Growth of $\text{In}_{0.1}\text{Ga}_{0.9}\text{As}/\text{GaAs}$ inside a SiO_2 pattern is shown in plots (a)-(d). Overflow deposition flux causes formation of two wide islands across the pattern..... 83

Fig. 4.3 Growth of $\text{In}_{0.25}\text{Ga}_{0.75}\text{As}/\text{GaAs}$ inside a SiO_2 pattern is plotted in a-f. ATGS instability occurs across the pattern. Small islands coalesce to form two islands near the walls driven by the effects of overflow flux. 85

Fig. 4.4 a) Von Mises stress contour after 5×10^8 simulation steps. Maximum Von Mises stress is 3.56 GPa. Yield strength equals to 5.5 GPa. Current flow strength is 5.5 GPa. Stresses below 0.05 GPa are shown in white. b) Von Mises stress (σ_{VM} - black) and components of stress tensor (σ_{xx} - blue, σ_{yy} - green, σ_{xy} - red). c) Strain components: ϵ_{tot} (blue) is the total strain in x direction, ϵ_{xx} (green) is elastic strain in x direction and ϵ^* (red) is the eigenstrain of

In_{0.25}Ga_{0.75}As/GaAs inside a SiO₂ pattern along AB line. Dashed lines in plots b and c separate substrate, gas and the film. 88

Fig. 4.5 Growth of In_{0.5}Ga_{0.5}As/GaAs inside a SiO₂ pattern is depicted in plots a-f. ATGS instability happens across the pattern. Small islands coalesce and form one big island, away from the walls. Plastically deformed regions for plot f is shown in plot g. 91

Fig. 4.6 a) Von Mises stress contour after 1.6×10^7 steps. Maximum Von Mises stress is 4.45 GPa. Initial yield strength equals to 3.5 GPa. Current flow strength is 4.45 GPa. Stresses below 0.1 GPa are shown in white, plastically deformed region is plotted in magenta. A small section of the pattern showing the stress in the island is magnified b) Von Mises stress (σ_{VM} – black) components of stress tensor (σ_{xx} – blue, σ_{yy} – green, σ_{xy} – red). c) ϵ_{tot} (blue) is the total strain in x direction, ϵ_{xx_el} (green) is elastic strain in x direction, ϵ_{xx_pl} (green) is plastic strain in x direction, and ϵ^* (red) is the eigenstrain of In_{0.75}Ga_{0.25}As/GaAs inside a SiO₂ pattern along AB line. Dashed lines in plots b and c separate substrate, gas and the film. 95

Fig. 4.7 Growth of InAs/GaAs inside a SiO₂ pattern are shown in a-d. No ATGS instability happens across the pattern. Islands are only formed at the walls. 96

Fig. 5.1 Excess Gibbs free energy of GaAsSb at 650 °C (solid line). Ninth order polynomial has been used to fit the function (dashed line). 108

Fig. 5.2 GaAsSb core-only nanowire during annealing a) before annealing, b) after 7×10^4 s and c) after 5×10^5 s of annealing at 650 °C. Separated phases are GaSb-rich phase (red) and GaAs-rich phase (blue). d) Contribution of different energy components before annealing and after annealing for 5×10^5 s. 114

Fig. 5.3 Composition of GaAsSb alloy core-shell nanowire with a GaAs thin shell after annealing for a) 7×10^4 s and b) 5×10^5 s. Separated phases are GaSb-rich phase (red) and GaAs-rich phase (blue). c) Contributions of different energy components to the total energy before annealing and after annealing for 5×10^5 s. 116

- Fig. 5.4 Composition of GaAsSb core-shell nanowire with GaAs thick shell after annealing for a) 7×10^4 s and b) 5×10^5 s. Separated phases are GaSb-rich phase (red) and GaAs-rich phase (blue). c) Contribution of different energy components before annealing and after annealing for 5×10^5 s. d) Effect of shell thickness on suppression of phase separation. The thicker the shell, the lower the phase separation. 120
- Fig. 5.5 a) Effect of misfit strain between the core and the shell on phase separation in the core. Compressive strain suppresses phase separation more than tensile strain. Maximum suppression of phase separation happens for -2.53% misfit strain. b) Comparison between the effect of shell thickness on phase separation with and without intermixing allowed between the core and the shell. Intermixing increases the amount of phase separation taking place in the core when shells are sufficiently thick, but even in that case the shell is still able to suppress a significant amount of phase separation..... 123
- Fig. 6.1 (Color online) Schematic view of a nanowire cross-section: a) Before yield: due to symmetry, only normal components of stress (σ_{rr} , $\sigma_{\theta\theta}$, and σ_{zz}) are nonzero. b) After yield: under high misfit strain, plastic deformation takes place in the structure. Elastoplastic region in the shell is shown in red while misfit dislocations at the core-shell interface are shown in dark blue. c) Shear stress S_{rz} as a function of radial position. Zero on the horizontal axis is defined at the center of the nanowire. 129
- Fig. 6.2 (Color online) Comparison of analytical solution (no plasticity) with FE simulations. a) Radial σ_{rr} , circumferential $\sigma_{\theta\theta}$ and axial σ_{zz} components of stress. b) Tresca and Von Mises effective stress compared with the yield strength. Zero radial position corresponds to the center of the core and 1000 nm corresponds to the surface of the shell..... 139
- Fig. 6.3 (Color online) Comparison of a) stress components b) plastic strain components between analytical solutions (Anl.) and FE simulations. Radial position of zero nanometers corresponds to the center of the core and 1000 nm corresponds to the surface of the shell. 141

Fig. 6.4 (Color online) Von Mises vs. Tresca yield criteria: a) Stress field. b) Plastic strain field. Radial position of zero nanometers corresponds to the center of the core and 1000 nm corresponds to the surface of the shell.	143
Fig. 6.5 Dependence of the thickness of the elastoplastic region ($b-c$) on a) the core radius, b) the shell thickness.	145
Fig. 6.6 Dependence of thickness of the elastoplastic region on the ratio χ (defined in text). a) χ varies between 0 to 5. b) χ varies between 0.25 to 1.	147
Fig. 6.7 (Color online) a) Dependence of strain energy per interfacial area on ratio χ (defined in text). b) Strain energy density across the nanowire. Zero radial position corresponds to the center of the core and 1000 nm corresponds to the surface of the shell.....	149
Fig. 6.8 (Color online) Dependence of a) the thickness of the elastoplastic region and b) strain energies on the misfit strain.	151

List of Tables

Table 4.1 Elastic constants, yield strength, surface energy, diffusion coefficient and growth conditions for different indium concentrations.	78
Table 4.2 Energy comparison between $\text{In}_{0.25}\text{Ga}_{0.75}\text{As}$ and $\text{In}_{0.5}\text{Ga}_{0.5}\text{As}$ thin films grown on GaAs. Surface energy refers to the energy of the film surface in contact with the gas phase. Interface energy refers to the energy between film and the walls.	92
Table 4.3 Energy comparison for $\text{In}_x\text{Ga}_{1-x}\text{As}$ thin films ($x = 0.5, 0.75$ and 1) grown on GaAs. Surface energy refers to the energy of the film surface in contact with the gas phase, which has two contributions, one from free energy density and the other one from gradient energy. Interface energy refers to the energy between film and the walls.	97
Table 6.1 Elastic constants, yield strength, and lattice mismatch for different InAs and GaAs.	138

Chapter 1 **Introduction**

1.1 **Motivation**

Semiconductors can be divided in two categories, elemental and compound. Silicon (Si) as an elemental semiconductor is the dominant material in chip fabrication while compound semiconductors are widely used in lasers and high efficiency electronic devices. Compound semiconductors have also shown better efficiencies in solar cells [1,2]. Despite the advantages offered by compound semiconductors, high material cost compared to elemental semiconductors has prevented them to be commonly used in industry in areas that more economic solutions such as silicon are available.

Electronic, optic, and thermodynamic properties of semiconductors are affected by strain [3-6]. One way to implement strain to semiconductors is by directly applying external force such as bending the structure. The advantage of this approach is the possibility to control and tune the applied strain and stress fields externally but there is a drawback associated with this approach. External application of stress and strain becomes increasingly more difficult by reducing the size due to physical limitations. For instance, direct application and control of stress and strains in nanoscale structures it is much more difficult compared to macroscale structures.

In single crystalline semiconductor nanostructures, strain can be applied during growth through a mechanism that is called epitaxy. Epitaxy is the growth on a crystalline substrate of a crystalline substance that mimics the orientation of the substrate (Merriam Webster). If the film and substrate are made of the same material or have the same lattice parameter, this process is called homoepitaxy and in this case no strain is generated between the film and the substrate. If the film and substrate are made of different materials and have different lattice parameters, the growth process is called heteroepitaxy and the strain that is introduced in the film is called a misfit strain. Structures that made by heteroepitaxy are called heterostructures. Fig. 1.1 shows a schematic view of epitaxial growth. The strain that is produced in heterostructures can be

controlled by choosing the lattice parameter of the substrate. Silicon is usually used as substrate in heterostructures due to low cost and good electronic properties. However, Si is not a good candidate for optical devices since it does not emit light under normal conditions. Hence, compound semiconductors such as GaAs are used for optical applications. Since elemental semiconductors, such as silicon and germanium (Ge), and compound III-V semiconductors such as gallium-arsenide (GaAs) and indium-arsenide (InAs) offer only a few lattice constants, a limited number of options are available to tune the strain in these heterostructures. Expanding the palate of material by making new binary (SiGe), ternary (InGaAs), quaternary (GaAsBiP) and more complex alloys will provide more flexibility to tune the strain in heterostructures.

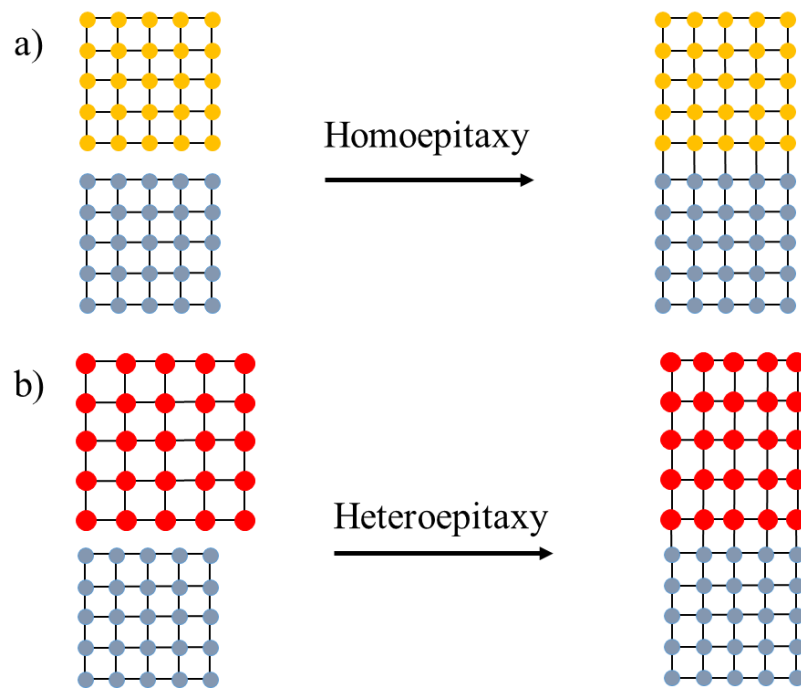


Fig. 1.1 a) Homoeptaxy: film and substrate have the same lattice parameter at equilibrium. No strain is stored in the film. b) Heteroepitaxy: film and substrate have different lattice parameters at equilibrium and hence the structure is strained.

There are three main epitaxial growth modes for semiconductor heterostructures: Island growth (Volmer–Weber) [7], layer-by-layer growth (Frank–Van Der Merwe) [8] and mixed growth (Stranski–Krastanov) [9]. These growth modes are determined based on the surface and interfacial energies between film and the surface, strain energy inside the film due to difference between lattice parameter of the film and the substrate (see Fig. 1.2a) and also diffusivity of atoms at the surface. As plotted in Fig. 1.2, wetting angle θ is related to the surface (γ_{SA} and γ_{SB}) and interfacial (γ_{AB}) energies through Young's equation [10] : $\gamma_{SA} = \gamma_{AB} + \gamma_{SB} \cos \theta$. The following criteria determines which growth mode is present.

- I. The Volmer–Weber growth mode (Fig. 1.2b) happens once at least one of the two following conditions is met:
 - a) $\gamma_{SA} \geq \gamma_{AB} + \gamma_{SB}$
 - b) Slow surface diffusion compared to deposition flux (kinetically limited).
- II. The Frank–Van Der Merwe growth mode (Fig. 1.2c) happens when both of the following conditions are met:
 - a) $\gamma_{SA} < \gamma_{AB} + \gamma_{SB}$
 - b) Fast surface diffusion compared to deposition flux (close to equilibrium).
- III. The Stranski–Krastanov growth mode (Fig. 1.2d) starts with a layer-by-layer growth and so the conditions mentioned for Frank–Van Der Merwe growth should hold. After growth of a few layers, strain leads to instability and causes formation of islands in this growth mode. I will discuss the effect of strain energy and its competition with surface energy to form surface undulations in chapter 2.

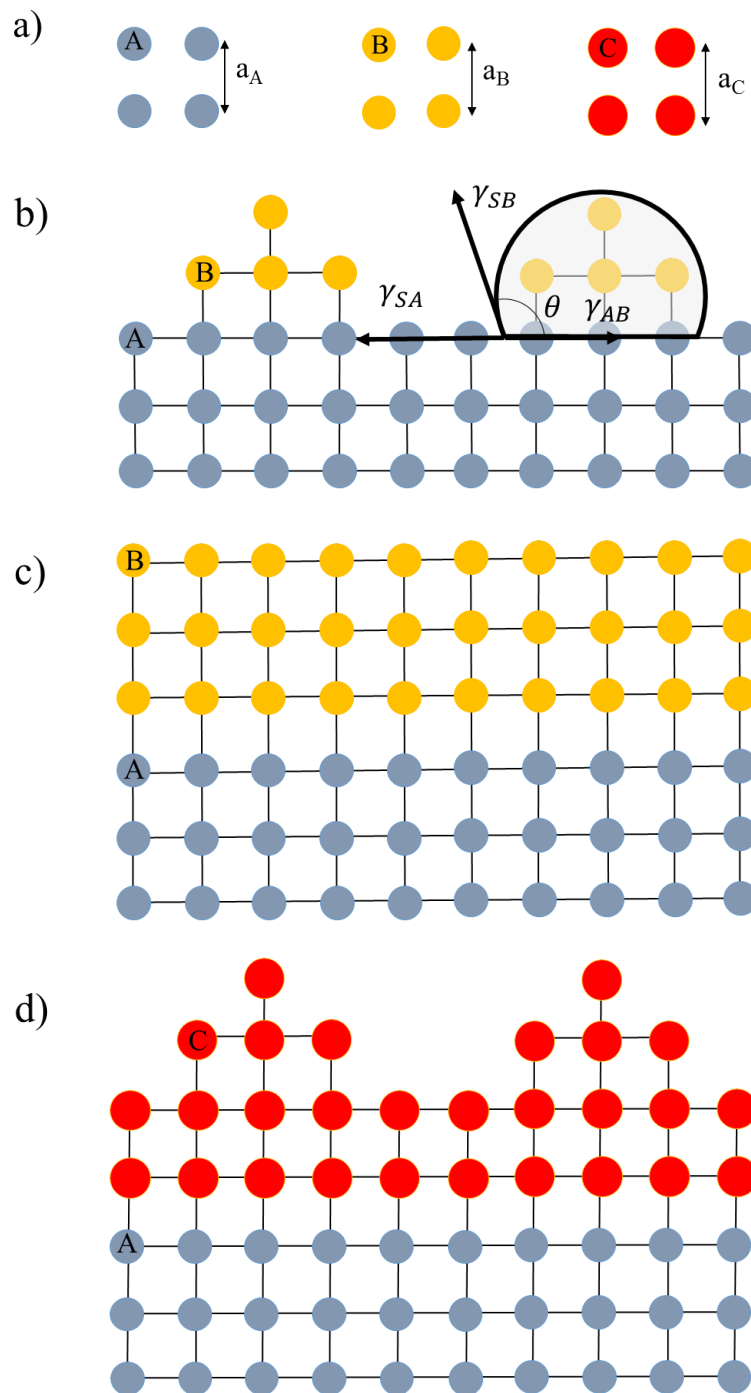


Fig. 1.2 a) Lattice parameter for three different material: A, B and C. Lattice parameter for A and B are equal, but lattice parameter of C is larger than lattice parameter of A and B. b) Volmer-Weber or island growth mode. c) Frank Van der Merwe or layer-by-layer growth mode. d)

Stranski-Krastanov or mixed epitaxial growth mode. Material C is under strain due to lattice mismatch with the substrate.

One of the most important impacts of strain on semiconductors is on the electronic band structure and bandgap of these structures [11-13]. By changing the crystalline symmetry of semiconductors, appropriate strain can be used to tune the bandgap and band structure of semiconductor structures. For instance, it has previously been shown that strain can change the band structure of Ge to change the indirect bandgap to direct one [14]. Also in case of III-V semiconductors for instance InGaAs alloy, strain is used to design devices with a specific bandgaps.

Despite many advantages that are provided by strain engineering in semiconductor heterostructures to modify material properties, there are some strain-induced phenomena that can also happen because of the strain. The driving force for these phenomena is relaxation of the strain energy stored in the system due to misfit strain. Fig. 1.3a shows structures with different lattice parameters where $a_A < a_B < a_C < a_D$. For thin films when thickness of the film is below a critical limit, growth is pseudomorphic and strain is stored in the film and substrate as shown in Fig. 1.1b. Once the thickness of the film passes a critical limit (elastic critical thickness), it has been observed in many heterostructures that the surface morphology of the film changes to relax the strain energy as shown in Fig. 1.3b, which leads to formation of islands on the surface. Elastic relaxation of thin films is a technique to make quantum dots and since individual dots are not deposited in this approach, this mechanism is called self-assembly [15-18]. However, elastic relaxation on the surface is not desirable for some device applications where the goal is to have a flat film such as quantum wells [19,20]. Formation of defects is another mechanism to reduce the strain energy in the system [21-23]. In heterostructures, the interface between the substrate and the film is a common place where misfit dislocations are initiated (see Fig. 1.3c) since strain

energy density in the film has its maximum value at the interface. These defects usually form when the thickness of the film passes a critical limit (plastic critical limit) [24]. Defects in general are not desirable since they deteriorate the material properties of the semiconductors. Another way that strain energy is released in heteroepitaxial systems is by phase separation (see Fig. 1.3d). Phase separation has been observed in compound thin film alloys during growth and annealing processes in forms of compositional modulations and clusters [25-27]. Fracture is another mechanism to relax the strain energy in the epitaxial structures as shown in Fig. 1.3d that happens when substrate is applying a tensile strain to the film. Crack formation in general is not desirable since it can deteriorate some of the mechanical and electronic properties of the film [20,28,29]. In addition to the above phenomena, buckling, peeling and bulging can relax strain in heterostructures. These strain relaxation mechanisms have been observed in heteroepitaxial semiconductors. Since these phenomena substantially affect mechanical, optical and electronic properties of semiconductor devices, it is crucial to understand and control them [20].

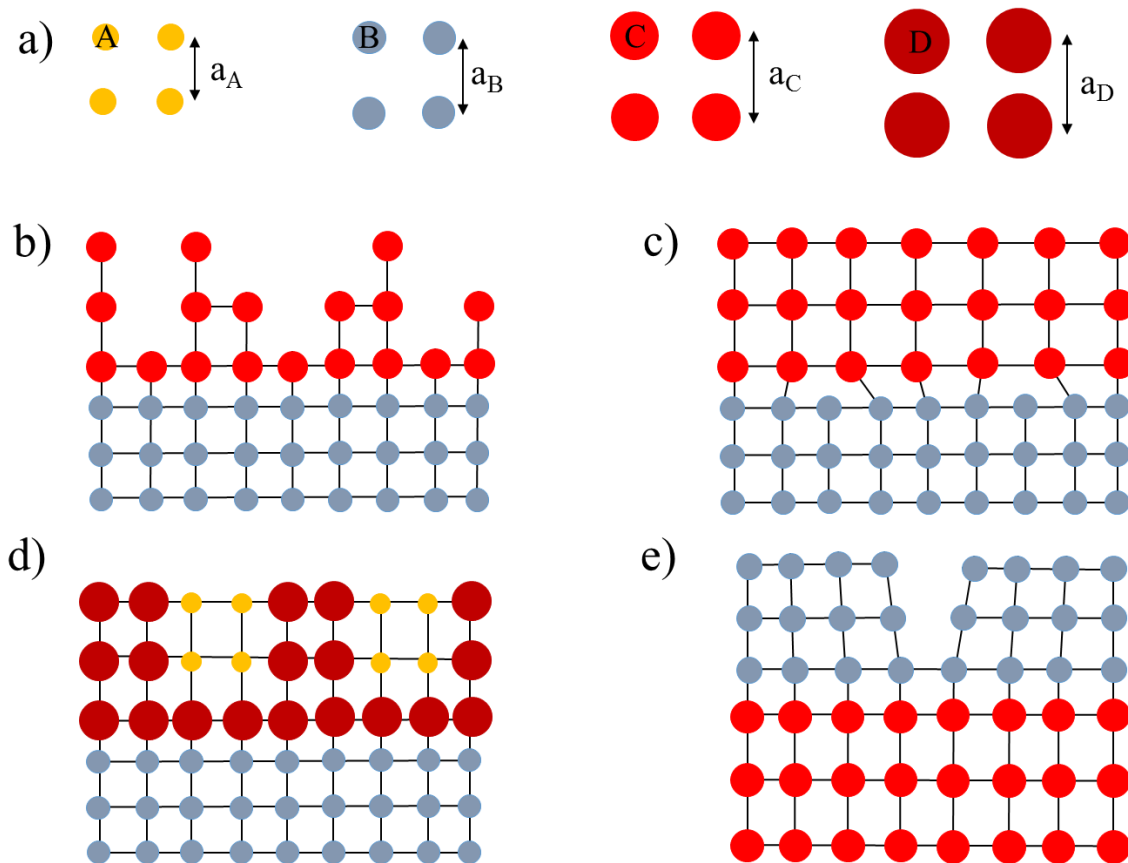


Fig. 1.3 a) Lattice parameter for four different material: A, B, C and D are shown where $a_A < a_B < a_C < a_D$. Different Relaxation mechanisms for heteroepitaxial thin films: b) Elastic relaxation of the film by morphological changes at the surface. c) Plastic relaxation of thin film due to misfit strain. This type of deformation usually starts at the interface. d) Surface induced phase separation. e) Crack formation in the film under tensile strain.

There are two main approaches to the growth of semiconductor heterostructures: physical vapor deposition (PVD) and chemical vapor deposition (CVD). In PVD, vapors of constituent materials that are usually made inside the chamber (from solid sources) are deposited on the substrate through a condensation process. No chemical reaction occurs in this process. Molecular beam epitaxy (MBE) is one of the most well-known PVD growth techniques. Since in MBE films

are grown at very low pressure, the concentration of impurities in the chamber is very low and hence high quality films can be grown. However, PVD is usually expensive and time consuming and hence is not usually used in industry. In CVD, reactant gases are introduced into the chamber. By setting the appropriate environmental condition (temperature, pressure, etc.), chemical reactions happen on the wafer substrate leading to the growth of thin film. Metal organic vapor phase epitaxy (MOVPE) is one of the dominant CVD growth techniques especially for III-V alloys. Although the films that are grown by CVD may have some contamination due to chemical reactions in the chamber, but the faster and more economic growth process has turned them into the dominant growth process in the industry.

1.2 Scope of the thesis

This thesis focuses on development of theoretical and analytical models to investigate and control the strain-induced phenomena in semiconductor heterostructures during growth and annealing processes. There are different physical phenomena that affect the growth and annealing of thin films, which can be divided in two general categories: thermodynamic and kinetic. Bulk free energy and interfacial energy between different components and phases in material system, and strain energies due to misfit strain and plastic deformations in the system are examples of thermodynamic phenomena. Bulk and surface diffusivities of different species in the material system, and the rate and the distribution of deposited material are kinetic terms that affect the growth and annealing of heterostructures. Our model captures the effects of both thermodynamics and kinetics. I will use this model to investigate and control growth and annealing processes of semiconductors.

The first application of the model is to provide an understanding to control growth of thin films in patterned surfaces. This is important since aligned islands can be used as quantum dots in devices and ordering of quantum dots in devices is critical to the performance of the device. Previous experimental researches have studied the growth of thin films inside surface patterns

and have observed alignment of islands near the edge of trenches for some composition of the alloy. Given that these films are strained, formation of islands is usually the first strain relaxation mechanism while plastic deformation is another mechanism that usually happens afterwards during the growth. Since growth process usually happens away from equilibrium condition, kinetic effects such as deposition flux and overflow flux can also play an important role and hence need to be included. So the goal of this study is to investigate the effect of different parameters on formation of islands during growth of thin films inside surface patterns.

Second application of the model includes the annealing of immiscible alloy semiconductors at high temperatures. It has been observed experimentally that surface-induced phase separation happens in compound semiconductor thin films (with miscibility gap in their phase diagram), however I want to study phase separation in nanowires. Surface-induced phase separation is more important in nanowires compared to thin films due to larger surface to volume ratio in nanowires. In addition, I would like to find a method to control this phase separation. One of the methods to control the phase separation is by applying strain to the nanowire and hence a shell has been included around nanowire core.

Third part of the thesis provides an analytical model to find stress and strain fields in plastically deformed core-shell heterostructures. Although core-shell nanowires have less strain energy due to heteroepitaxy compared to the thin films with similar dimensions, but they also deform plastically when misfit strain between core and shell is large enough. This plastic deformation usually happens at the interface between core and the shell. Plastic deformation affects the strain and stress field and hence changes the piezoelectric and optoelectronic properties of these structures.

1.3 Organization of this document

Chapter 1 provides introduction and motivation to the study. Chapter 2 contains relevant background information about semiconductors and their applications. I talk about semiconductors

and their application. Then I discuss the effect of strain on changing electronic properties of semiconductors. I introduce heteroepitaxy as one of the mechanisms to grow single crystalline structures and also as a method to apply strain to semiconductors. Then I discuss some of the consequences of applying strain to semiconductor structures such as formation of defects, morphological roughness, phase separation and cracking. An overview of different experimental methods to grow epitaxial layers will be followed by a review on different simulation methods to study semiconductor heterostructures. Chapter 3 provides some details about phase field modeling and the numerical approach to solve the governing equations. I explain the general governing equations and boundary conditions used in the model. Then I discuss some methods that can be used to solve these governing equations. In chapter 4, I investigate the role of misfit strain, surface patterns and kinetics due to deposition on growth of heteroepitaxial III-V semiconductors thin films inside patterned substrates. This study enables us to understand the coupled effects of kinetics and thermodynamics during the growth in patterned substrates. Also, this study can provide us some guidance to better understand the self-assembly process of quantum dots. In chapter 5, I investigate the role of coating around nanowires to control phase separation of alloys during annealing. Looking at the phase diagram of many of III-V semiconductor material such as InGaAs, AlGaAs, and GaAsSb, one can find a miscibility gap indicating that under thermodynamic equilibrium these alloys tend to phase separate. Phase separation typically happens at high temperatures where atoms have enough mobility. Controlling the phase separation is important because it can deteriorate some of the electronic properties of the material such as photoluminescence intensity. Chapter 6 provides an analytical formulation for plastic deformation in core-shell nanowires. Plastic deformation at the interface of the substrate and the structure (thin film, nanowire, etc.) is one of the most important issues caused by heteroepitaxy. This plastic deformation changes the displacement, strain and stress field of the structure. These plastic deformations have been observed experimentally, however the analytical

study of these heteroepitaxial systems has been limited to the analysis of elastic regime till the onset of yield. In this chapter, I develop an analytical model that is able to predict not only the onset of plastic deformation, but also evolution of stress and strain fields beyond the yield regime. In chapter 7, I will conclude the work and will provide some suggestions for future studies for each of the projects.

1.4 Reference

- [1] F. Dimroth, *Phys Status Solidi C* **3**, 373 (2006).
- [2] K. Tanabe, *Energies* **2**, 504 (2009).
- [3] S. Adachi, *Physical properties of III-V semiconductor compounds : InP, InAs, GaAs, GaP, InGaAs, and InGaAsP* (Wiley, New York, 1992).
- [4] D. G. Zhao, S. J. Xu, M. H. Xie, S. Y. Tong, and H. Yang, *Appl. Phys. Lett.* **83**, 677 (2003).
- [5] F. Greuter and G. Blatter, *Semicond. Sci. Technol.* **5**, 111 (1990).
- [6] H. P. He, F. Zhuge, Z. Z. Ye, L. P. Zhu, F. Z. Wang, B. H. Zhao, and J. Y. Huang, *J. Appl. Phys.* **99**, 023503 (2006).
- [7] K. Oura, V. G. Lifshits, and A. A. Saranin, *Surface Science: An Introduction* (Springer, Berlin, 2003).
- [8] A. Pimpinelli and J. Villain, *Physics of Crystal Growth* (Cambridge University Press, Cambridge, 1998).
- [9] I. N. Stranski and L. Krastanow, *Akademie der Wissenschaften Wien* **146**, 797 (1938).
- [10] T. S. Chow, *J Phys-Condens Mat* **10**, 445 (1998).
- [11] G. Gui, J. Li, and J. X. Zhong, *Phys Rev B* **78**, 075435 (2008).
- [12] A. M. Smith and S. M. Nie, *Acc. Chem. Res.* **43**, 190 (2010).
- [13] J. A. del Alamo, *Nature* **479**, 317 (2011).
- [14] K. Kusova, P. Hapala, J. Valenta, P. Jelinek, O. Cibulka, L. Ondic, and I. Pelant, *Adv Mater Interfaces* **1**, 1300042 (2014).
- [15] Y. A. Vlasov, N. Yao, and D. J. Norris, *Adv. Mater.* **11**, 165 (1999).
- [16] M. Kroutvar, Y. Ducommun, D. Heiss, M. Bichler, D. Schuh, G. Abstreiter, and J. J. Finley, *Nature* **432**, 81 (2004).
- [17] H. T. Jiang and J. Singh, *Phys Rev B* **56**, 4696 (1997).

- [18] J. Tersoff, C. Teichert, and M. G. Lagally, *Phys. Rev. Lett.* **76**, 1675 (1996).
- [19] E. A. Fitzgerald, S. B. Samavedam, Y. H. Xie, and L. M. Giovane, *J Vac Sci Technol A* **15**, 1048 (1997).
- [20] L. B. Freund and S. Suresh, *Thin film materials : stress, defect formation, and surface evolution* (Cambridge University Press, Cambridge, England ; New York, 2009), 1st pbk. edn.
- [21] B. W. Dodson and J. Y. Tsao, *Appl. Phys. Lett.* **51**, 1325 (1987).
- [22] R. Beanland, D. J. Dunstan, and P. J. Goodhew, *Adv Phys* **45**, 87 (1996).
- [23] Y. B. Bolkhovityanov and L. V. Sokolov, *Semicond. Sci. Technol.* **27**, 043001 (2012).
- [24] J. W. Matthews, A. E. Blakeslee, and S. Mader, *Thin Solid Films* **33**, 253 (1976).
- [25] E. Luna, M. Wu, J. Puustinen, M. Guina, and A. Trampert, *J. Appl. Phys.* **117**, 185302 (2015).
- [26] K. C. Hsieh, K. Y. Hsieh, Y. L. Hwang, T. Zhang, and R. M. Kolbas, *Appl. Phys. Lett.* **68**, 1790 (1996).
- [27] M. Tang and A. Karma, *Phys. Rev. Lett.* **108**, 265701 (2012).
- [28] V. K. Yang, M. Groenert, C. W. Leitz, A. J. Pitera, M. T. Currie, and E. A. Fitzgerald, *J. Appl. Phys.* **93**, 3859 (2003).
- [29] H. P. Liaw and R. F. Davis, *J. Electrochem. Soc.* **131**, 3014 (1984).

Chapter 2 **Background**

2.1 **Semiconductors and their applications**

Semiconductors are considered as foundation of modern electronics. There are two types of semiconductor materials: elemental and compound. Elemental semiconductors such as Si and Ge are most commonly studied and used materials due to abundance, low price and easy processing. However, there are some drawbacks associated with elemental semiconductors such as having an indirect band gap, which prevents them from being used in optical applications. Compound semiconductor alloys are made from mixture of elements such as III-V, II-VI and IV-IV material in periodic table. Although compound semiconductors are expensive and difficult to process, but they provide some electronic and optoelectronic properties that are superior to properties of elemental semiconductors. Compound semiconductor materials are very interesting due to flexibility for tuning their band gap simply by changing the composition [1]. Specifically, III-V semiconductors are very interesting due superior electronic and optic properties compared to IV-IV alloys. Therefore, many researchers have studied III-V semiconductors both experimentally and theoretically. One of the most popular III-V alloys is GaAs. Electron mobility of GaAs is six times higher than mobility of Si, which allows faster electronic operations. Unlike silicon, gallium arsenide has a direct band gap that makes it a good candidate for optoelectronic applications. Also, GaAs has a wider band gap compared to Si that enables GaAs to operate under higher temperatures with lower noise compared to Si. However, GaAs is expensive and challenging to process (e.g., it is brittle) and so it is only used when Si is not sufficient for the specific application.

In this chapter, I first introduce electronic structure of semiconductors. Then I discuss different types of defects that are formed in semiconductor structures. Afterwards, I present some of the strain-related phenomena in heterostructures. Then I discuss some of the techniques that are used to grow semiconductor structures. Finally, I explain some of the modeling approaches

that have been used to investigate electronic structure, morphology and defect structures of semiconductors.

2.2 Defects in semiconductors

Defects in materials can be classified based on their dimensionality. There are zero dimensional (point defects such as vacancies and interstitials), one dimensional (line defects such as dislocations), two dimensional (plane defects such as grain boundaries and interfaces) and three dimensional (volume defects such as precipitates) defects.

2.2.1 Point defects (zero dimensional)

There are two main types of point defects: intrinsic and extrinsic. Intrinsic point defects are the ones that only consist of native atoms of the material of interest while external defects are usually dopants that are incorporated into the system that I study.

Extrinsic point defects are usually in the form of dopants that are atoms that replace one of the host atoms of the structure. For instance is GaAs structure, depending on the growth condition, sometimes these dopants are incorporated into the structure unintentionally. One type of impurities that has been observed in Hydride vapor phase epitaxy (HVPE) is Si. Si atoms would replace Ga and/or As lattice sites. Given that Si has four atoms in the valence band, it will cause a local negative or positive charge when it is substituted with Ga and As, accordingly. The Si defects are shown in Fig. 2.1 with green color. When Si sits on Ga site, it has an extra electron and hence creates an n-type material while sitting in As site will create an extra hole and subsequently a p-type material. Growth condition plays an important role in formation of this kind of defects. For instance in HVPE, researchers have found that high gas pressure of As precursor has an important effect on reduction of the Si impurities in the structure.

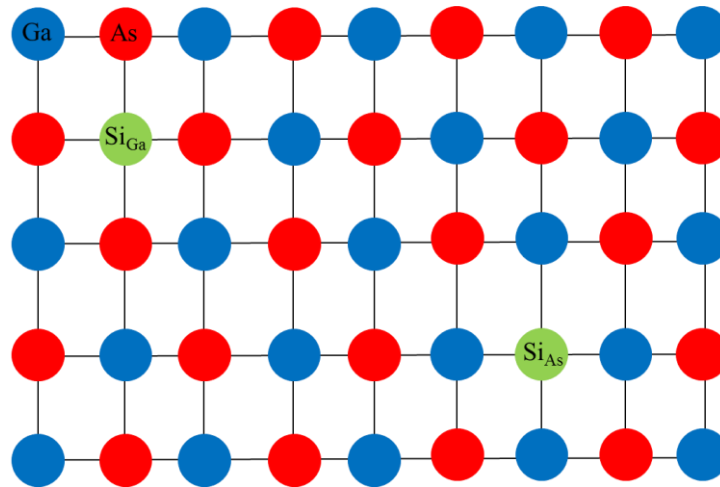


Fig. 2.1 Schematic representation of the incorporation of extrinsic point defect Si (green) for Ga (blue) and As (red) in GaAs. Elastic strain introduced by the impurity is not shown in this schematic picture.

Intrinsic point defects are usually in the form of vacancies or antisites from the native atoms of the structure. The simplest form of intrinsic point defect is a vacancy. In compound systems such as GaAs, there are two types of vacancies: Ga vacancies (V_{Ga}) and As vacancy (V_{As}) as shown in Fig. 2.2. More complex form of vacancies can also exist in the structure where two or more vacancies are formed next each other. Another form of intrinsic point defect is called an anti-site. This is when a Ga atom occupies a site of an As atom or vice versa. These defects are labeled as Ga_{As} or As_{Ga} , respectively, and are shown in Fig. 2.3. For example in GaAs system, As_{Ga} has direct correlation with one of the prominent defects in GaAs structure.

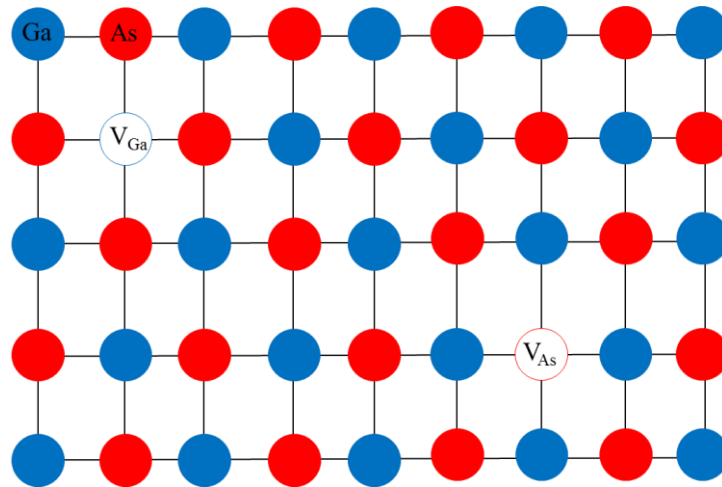


Fig. 2.2 Formation of vacancies in Ga (V_{Ga}) and As (V_{As}) sites.

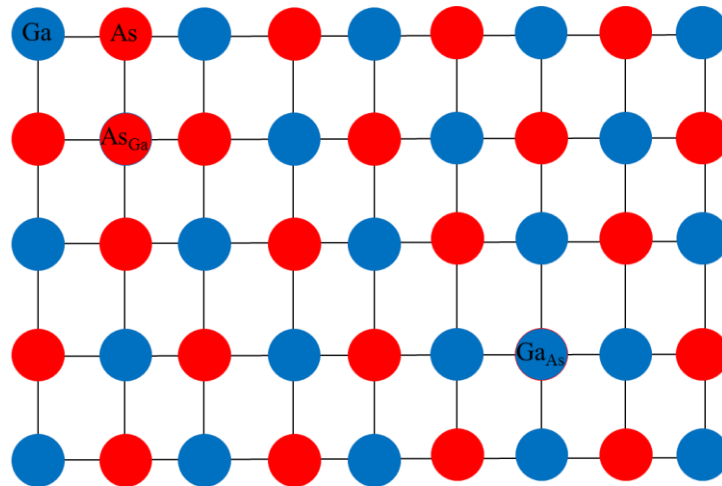


Fig. 2.3 Formation of Ga_{As} and As_{Ga} anti-sites in GaAs structure.

Defects in semiconductors have important effects on electronic structure of these materials. They usually disrupt the crystalline structure and locally alter the bonds in the structure. These local defects usually cause formation of dangling bonds and associated strain field that leads to creation of states in their band gap. These states are usually close to the center of the bandgap and hence are called “deep states” or “deep traps”. The position of trap states in the bandgap

distinguishes them from states that are created by doping since they are close to either valance or conduction band of the structures. Deep traps act as recombination sites for charge carriers. These recombination sites usually reduce the efficiency of the device by removing charge carriers and hence are not favorable. In addition, deep traps can create noise in the current and negatively influence the performance of the device. Since deep traps reduce the lifetime of charge carriers and long lifetime of charge carriers is favorable, one needs to minimize the concentration of deep traps that leads to increase of device efficiency.

2.2.2 Extended defects

In addition to point defects, there are one, two and three-dimensional defects that form in semiconductor structures. For simplicity, I call them extended defects. Dislocation is one type of the extended defects. One of the main causes of formation of dislocations is the heteroepitaxy as I briefly discussed in the first chapter. Heteroepitaxy has many uses such as synthesis of new devices and fabrication of economic semiconductor devices. For instance, heteroepitaxy has enabled researchers to fabricate quantum cascade laser devices. Also, it has provided the capability to choose reasonable substrates to replace the more expensive one to reduce the cost of devices. However, growth of heterostructures can be challenging depending on the strain applied to the film due to the difference between lattice parameter of the film and substrate. Below one can see how the bandgap of most common semiconductors changes as a function of lattice parameter. As it is shown in Fig. 2.4, there is a vast area of materials available, but only a small portion of the alloys are accessible experimentally. Due to limited number of commercially available substrates that are shown by green dashed lines in Fig. 2.4, researchers need to grow heterostructures to explore the ternary and quaternary alloys.

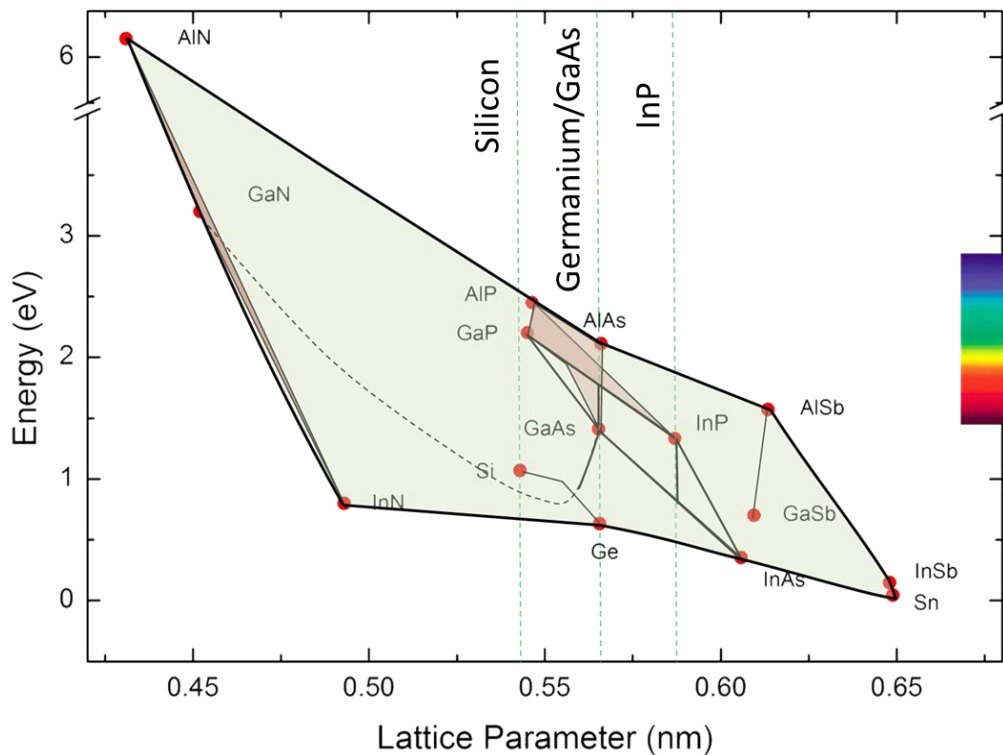


Fig. 2.4 Plot of bandgap as a function of the lattice parameter of common semiconductors (red dots). Solid black lines between each two dot show the alloy that can have specific bandgap based on the lattice parameter of the alloy. The areas between three or more dot represent compound alloys of more than three materials. The green dashed line represent the lattice parameter of commercially available substrates. Courtesy of Prof. Thomas Kuech from University of Wisconsin – Madison.

2.3 Heteroepitaxy

As mentioned in chapter one, heteroepitaxy means growth of film on substrate made from a different material that usually has a different lattice parameter. Due to this difference in lattice parameters, there is a strain stored in the film called misfit strain (Fig. 2.5a) which is defined as:

$$\epsilon_0 = \frac{a_{film} - a_{substrate}}{a_{substrate}}$$

Heteroepitaxial growth of semiconductors usually starts by a pseudomorphic growth. As shown in Fig. 2.5b, film is coherently strained to fit its lattice parameter to that of the substrate and film is also strained out of the plane due to Poisson effect. By increasing film thickness, the strain energy in film increases until it reaches a critical value after which dislocations form (Fig. 2.5c). Formation of dislocation releases the strain energy stored in the system. Misfit strain is usually relaxed by edge dislocations that can be described as an extra half plane of atoms in the substrate or the film depending on their lattice parameters. The extra half plane created by edge dislocation is perpendicular to the Burger's vector. Another type of dislocation is screw dislocation where the extra half plane of atoms is parallel to Burger's vector.

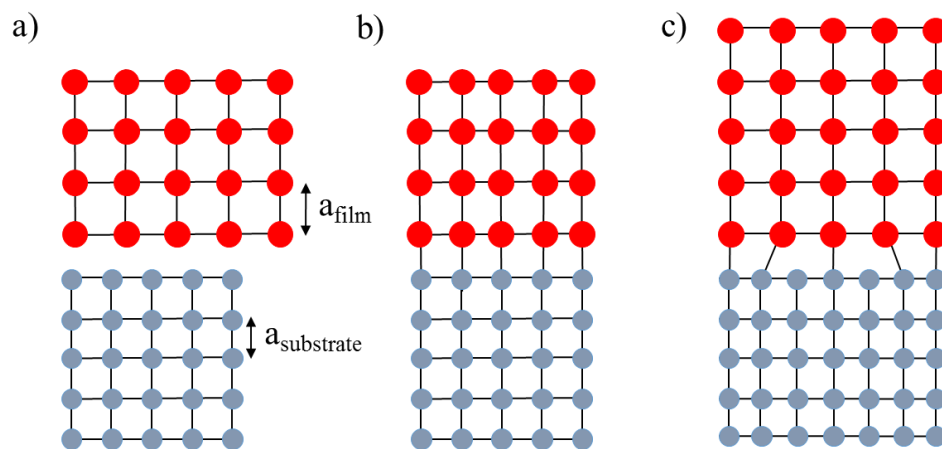


Fig. 2.5 a) Heteroepitaxial growth: film and substrate have different lattice parameters a_{film} and $a_{\text{substrate}}$. b) Coherent growth of thin film on substrate (pseudomorphic growth). c) Incoherent growth of thin film on substrate due to formation of misfit dislocations at the film/substrate interface.

Nucleation of dislocation depends on the crystalline structure of the material. Once they are formed, they usually glide on the close packed planes. For III-V semiconductors such as GaAs with zinc-blend structure, family of $\{111\}$ planes is the closed packed planes. In III-V structures,

60° dislocations with line direction along $\langle 110 \rangle$ are usually formed. The Burger's vector for these dislocations is along $a/2\langle 101 \rangle$ and is inclined 60° from the hetero-interface. Hence, Burger's vector has in plane contributions along $a/4\langle 110 \rangle$ due to misfit dislocations and out of plane contributions along $a/2\langle 001 \rangle$.

Similar to point defects, dislocations also disturb the periodicity of the crystal structure and hence cause formation of deep states in the bandgap. These deep states deteriorate the efficiency of devices and so are not favorable. Threading dislocations in particular have extremely negative effects on performance of semiconductors since they can potentially pass through the entire structure.

2.4 Strain-related phenomenon in growth of semiconductor heterostructures

2.4.1 Elastic relaxation (morphology change)

In previous section, I introduced the misfit strain in heterostructures. This misfit strain is stored in the system as strain energy and once it reaches to a critical level, it relaxes. There are several mechanisms for energy relaxation in heterostructures. I named some on them in the first chapter. Here I explain these mechanisms in more details. One of the methods to partially relax the strain energy is by formation of morphological roughness (undulations) to the surface of the thin film. Researchers have investigated the stability of a flat surface under elastic strain and have found that flat surface is unstable with respect to the growth of perturbations with wavelengths of greater than a critical wavelength. It is found that for strained heterostructures in form of thin films, strain energy and surface energy are the important terms determining the surface undulations [2]. Here I consider a simple energetic analysis to show the nature of instability. Let's consider a simple square shaped wave surface morphology as shown in Fig. 2.6. For this analysis, I consider the effect of surface energy and strain energy. The change in energy between cases shown in Fig. 2.6 b-c can be shown as:

$$\Delta W = -\frac{\sigma^2 c \lambda}{2E} + 2c\gamma \quad 2-2$$

where ΔW is the change in energy, σ is the stress in the film, γ is the surface energy, E is the Young's modulus, $c/2$ is the amplitude of the undulation and λ is the wavelength. For this simple analysis, I have assumed the strain energy to be zero inside the square shaped protrusions. By making Eq. (2-2) equal to zero I found $\lambda = \frac{16\gamma E}{\sigma^2}$. So for wavelengths larger than this value the total energy is going to reduce by formation of undulations and hence it is thermodynamically favorable. Although this is a rough analysis, but it gives an idea why the surfaces of stressed structures are unstable. A more rigorous analysis of stressed surface can be found in research conducted by Srolovitz [2].

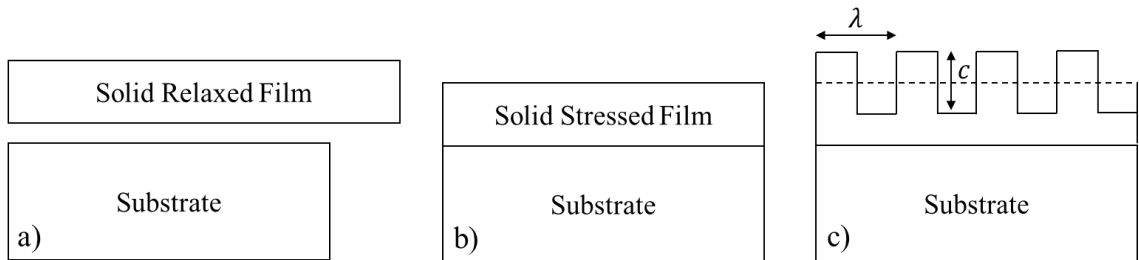


Fig. 2.6 a) Relaxed heterostructure. b) Strained heterostructure. c) Film with a square wave surface profile. The surface profile has wavelength of λ and magnitude of c .

Although these surface roughening may not be favorable for the growth of some devices that need flat surfaces, but it can be useful for the growth of self-assembled quantum dots. Formation of quantum dots (QDs) has been reported in number of experimental and theoretical papers. Notzel *et al.* [3] reported self-organization of QDs of strained InGaAs layers growing on GaAs (311)B using MOVPE technique. After growing AlGaAs buffer layer, InGaAs was deposited. Interestingly, the morphology of the AlGaAs buffer layer was changed due to a lateral mass transport and AlGaAs islands were formed. Deposited InGaAs layer formed clusters and buried

beneath the AlGaAs QDs. It is shown that by controlling the In content and hence the strain, one can control the size and distance between QDs [4]. Vertical control of QDs along with the lateral control provides us with a mechanism to grow three-dimensional arrays. Vertical alignment of dots in growth direction during subsequent deposition of layers and spacers has been observed by different groups for InGaAs/GaAs and Si/SiGe systems [5]. Average size and lateral separation of the islands depends on the strain field in the heterostructure where an InAs island locally changes the lattice parameter of GaAs spacer and hence the next layer of InAs prefers to grow on an area where misfit strain is lower. However this strain field is local and it has been found that the pairing of islands has an inverse relationship with the thickness of spacer layer due to decay of strain field. In addition to vertical ordering, lateral ordering has also been observed for different material systems. For instance, Grundmann *et al.* [6] observed high degree of lateral ordering for vertically aligned QDs where the thickness of spacer is small enough and initial dots are laterally close to each other. Stranski-Krastanow growth mode has been used for growth of QDs where actual control over the position of the islands is needed [7]. In addition to experimental studies about the self-assembly of QDs, theoretical investigations have also been performed. Wise *et al.* [8] modeled the effect of substrate strain patterning on self-assembly of QDs. They showed that strain patterned substrates by embedded inclusions resulted in formation of ordered self-organized QD arrays. However these predictions were only valid for the case where surface energies are isotropic. Cubic surface energy would strongly influence the QD self-assembly and prevent the formation of ordered arrays of pyramids.

2.4.2 Plastic relaxation

Once the film thickness passes a critical value called “ h_c – critical thickness”, strain energy stored in the system reaches a threshold where formation of dislocations becomes favorable energetically. Because of the importance of the critical thickness, many researchers have

investigated it both experimentally and theoretically. Matthews and Blakeslee [9] have derived estimations for h_c assuming equilibrium conditions:

$$h_c = -\frac{b(1-\nu \cos^2 \beta)}{8\pi\epsilon_0(1+\nu) \cos \beta} \ln\left(\frac{h_c}{b}\right) \quad 2-3$$

where b is the Burgers vector, ν is Poisson's ratio, β is the angle between dislocation line and its Burgers vector, and ϵ_0 is the misfit strain between film and substrate. This theory does not consider the initial nucleation energy of dislocations. This simplification in theory leads to some discrepancies between the predictions and experimental results as shown in Fig. 2.7. However this discrepancy has only been observed for epitaxial films with very high quality while the experimental results and theoretical predictions are in good agreement for lower quality of films where some dislocations have already been nucleated in the system.

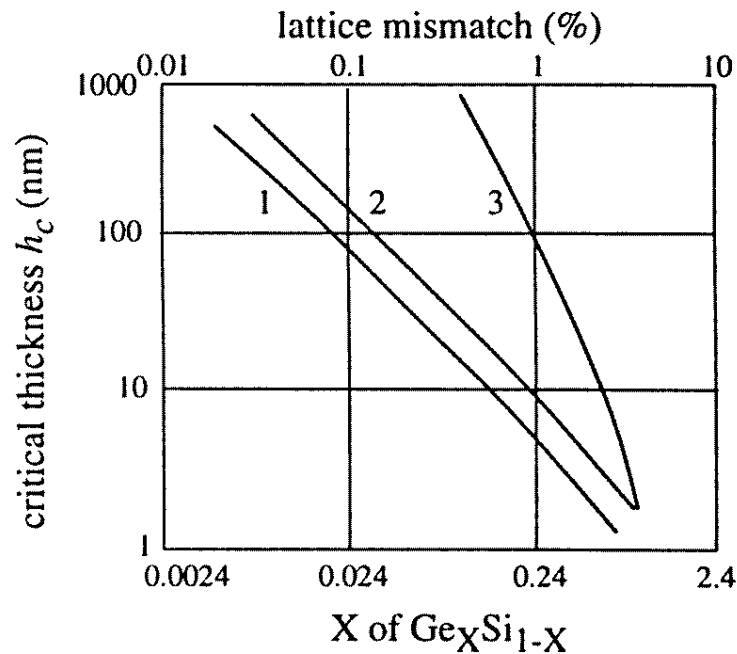


Fig. 2.7 Critical thickness for SiGe/Si. Curves 1 and 2 represent critical thicknesses for 90° and 60° dislocations and curve 3 represents experimental observations. The figure is taken from [10].

Ozkan *et al.* [11] investigated strain relaxation and defect formation mechanisms during surface roughening for SiGe/Si system during annealing. They found that valley regions in undulated surfaces act as dislocation generation sites due to the stress concentration. Fitzgerald *et al.* [12] reported the effect of elastic and plastic strain in surface perturbation of heterostructures. They found that strain levels above 10^{-4} perturb thin film surface to relax the strain energy elastically. Wavelength for these relaxations is short. Besides, they found that misfit dislocations also affect the morphology of thin films, however they cause formation of long wavelength undulations. Hence, one can find the source of undulation based on the wavelength of the surface perturbation.

2.4.3 Phase separation / intermixing

Phase separation or compositional modulations and intermixing are two phenomena that affect the growth and annealing of semiconductors. Phase separation usually takes place in semiconductor alloys that have miscibility gap in their phase diagram, which is the case for many of III-V semiconductors. For instance, Luna *et al.* [13] found spontaneous formation of a lateral composition modulation (LCM) in GaAsBi epilayers grown by Molecular Beam Epitaxy (MBE). Hsieh *et al.* [14] observed LCM in AlGaAs film upon annealing and found that the phase separation was more pronounced near the free surface. The authors proposed a stress-driven vacancy-assisted mechanism to be responsible for this phenomenon. Tang *et al.* [15] used linear stability theory to study the role of free surfaces in spontaneous phase separation of alloys in thin films and found that stress relaxation begins at the surface. Markowitz *et al.* [16] studied AlGaAs nano-whiskers grown by solution-liquid-solid mechanism. Their results show a kinetically driven phase separation during the growth despite the fact that the thermodynamic phase diagram suggests a homogenous growth at the temperature of interest. Therefore, the authors concluded that phase separation is kinetically driven and hence the compositional modulation is metastable. Ueda *et al.* [17] reported epitaxial growth of lattice-matched InGaAsP and InGaP on GaAs

substrate. They observed modulated structures with compositional variations along $\langle 100 \rangle$ and $\langle 010 \rangle$ directions. In addition to phase separation, intermixing can also play a role in reducing the free energy of the system and hence affect the growth and annealing of heterostructures. For instance, Tu and Tersoff [18] developed a sharp-interface continuum based model to study formation of self-assembled QDs alloys from SiGe. Their model shows morphological changes and intermixing as two mechanisms to reduce the total free energy of the structure and the model also shows a strong coupling between morphological changes and intermixing. Phase separation has been initially initiated at the surface of the alloy due to the different surface energies of Si and Ge.

2.4.4 Fracture

If the film is under tensile strain, the relaxation mechanism is usually by formation of cracks. Similarly to a thin film under compressive strain, there is a critical thickness for a film under tensile strain below which film grows pseudomorphically. A number of studies have been reported regarding criteria for fracture during film growth. For instance, Matthews [19] has shown a critical thickness for the propagation of the cracks that is shown in Fig. 2.8. In this figure, line A represents critical thickness for crack propagation. For instance, line A shows that for 1% misfit strain (y axis), crack propagates for films with thicknesses equal or larger than 100 nm (x axis). Line B corresponds to the fracture criterion that usually happens at high misfit strains larger than 5%. Line C represents the equilibrium critical thickness below which it is energetically favorable for the film to be coherently strained to the substrate. Dashed line represents plastic relaxation critical thickness below which there is no plastic deformation. At the strain of about 1%, there is a crossover between crack formation and plastic deformation lines. For strains reasonably higher than $\sim 1\%$, very thin films are coherently strained to the substrate. By increasing the film thickness (crossing line C), film becomes metastable but no relaxation mechanism is activated till the film thickness reaches line A where cracks start to propagate. By

further increase in the film thickness, no plastic deformation happens since cracks do not allow dislocations to pass. For strains lower than $\sim 1\%$, the order of relaxation mechanisms is reversed. After a film crosses line C, films become metastable but still coherently attached to the substrate. By increasing the film thickness (crossing dashed line), plastic deformation mechanism is activated. Further increase in the film thickness activates cracking at the point where the film thickness crosses line A.

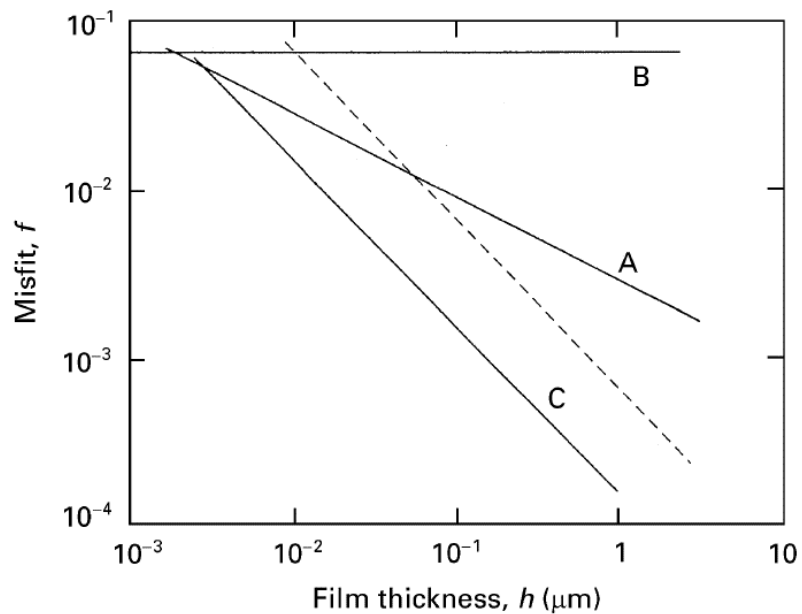


Fig. 2.8 Graphical summary of the predictions for films under tensile strain [19,20]. The graph shows misfit strain as a function of film thickness. Above line A, crack propagates. Above line B, film fractures spontaneously. Below line C, it is energetically favorable for the film to elastically relax. Dashed line shows relaxation critical thickness.

In this section, I focused on strain relaxation mechanisms that do not involve buckling and delamination. However in general, strain relaxation may involve such in plane and out of plane buckling and also delamination mechanisms such as peeling and bulging. Freund and Suresh [21] have provided more information about different relaxation mechanisms in more detail.

2.5 Film deposition techniques

Physical Vapor Deposition (PVD) and Chemical Vapor Deposition (CVD) are the most common approaches to grow thin films and heterostructures for depositing of material atom-by-atom from a vapor phase on a substrate. Vapor deposition is a mechanism through which the material is transferred from a vapor environment into a solid surface and hence the mass of the substrate increases. To be able to control the vapor composition, this deposition process is usually carried in a vacuum chamber. If the material deposited is produced by chemical reactions, the process is called CVD. If physical means are used to transfer vapor to a substrate as solid film, then the process is called PVD. There are a variety of methods developed both under PVD and CVD categories, each were trying to use some particular advantages for a specific system of material. In this section, I explain the growth mechanisms used both on PVD and CVD and also describe some of the specific techniques developed for each of them.

2.5.1 Physical vapor deposition

Physical vapor deposition is a technique in which atoms are physically deposited from a solid or a molten source onto a substrate. PVD uses physical processes such as evaporation, sublimation, and sputtering to produce thin films. A schematic view of evaporative deposition is shown in Fig. 2.9. In this mechanism, thermal energy is provided to the source to evaporate the atoms. There are different methods to heat the sample. Resistance, induction and electron beam heating are among the approaches that are used. Once the atoms are evaporated from the source, they travel in the low-pressure vacuum and condense on the substrate. The deposition rate of the film on substrate is a function of multiple parameters such as the distance between source and the substrate, impingement angle, temperature of the substrate and pressure of the chamber.

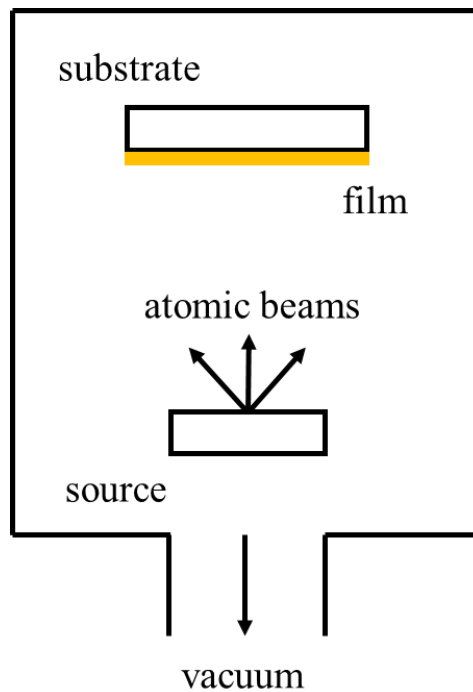


Fig. 2.9 Schematic view of evaporative PVD growth. The chamber is usually under high vacuum. A physical process is used to produce vapor from solid source of material. Material vapor is then deposited on substrate.

Molecular Beam Epitaxy (MBE) is one of the methods based on evaporation technique in ultra-high vacuum (10^{-10} torr). MBE can provide high quality films and hence is used in research; however, its low growth rate compared to other techniques has made its application to be limited in industry. After putting the substrate into the chamber, it is exposed to high temperature for a short period of time to remove the defects and contamination that may exist at the surface. This process is called flashing and the high temperature is provided to the sample by conduction. Subsequently the sample is cooled down to the range of 400-700°C, which is the temperature regime for growth. Once the substrate is in this temperature range, the source will be heated up to

the point where atoms evaporate and atomic beams are emitted. Atomic beams are received on the substrate surface and film grows through condensation process.

2.5.2 Chemical vapor deposition

The basic idea of chemical vapor deposition is to grow a non-volatile film on the substrate by chemical reactions between volatile reactants and suitable gas environment to facilitate this process as shown in Fig. 2.10. Similar to PVD, vapor supersaturation as well as substrate temperature affect the growth rate in CVD. Low gas supersaturation and high substrate temperature leads to epitaxial growth of thin film while high supersaturation of environment gas along with low growth temperature of the substrate result in growth of less coherent and possibly amorphous thin films.

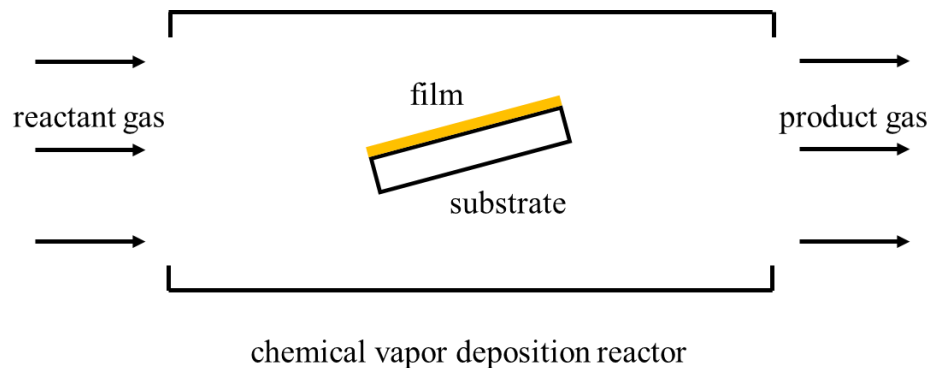


Fig. 2.10 Schematic view of CVD growth. The chamber is under vacuum. Reactant gases flow into the chamber and products leave the chamber after the reaction is done at the surface. The reaction at the surface produces the desired deposit.

There are different types of the CVD method. Here I explain each of these different types briefly. Atmospheric-Pressure CVD (APCVD) is the simplest and fastest CVD growth mode. However, the films grown by APCVD are usually non-uniform in thickness due to the limitation of mass transport. Low-Pressure CVD (LPCVD) provides high quality and uniform films but the

films are usually grown at high temperatures, which is not always favorable. Plasma Enhanced CVD (PECVD) is the most common growth technique for research. The advantage of this growth mode is that plasma helps the molecules to break up and hence the growth can be done at lower temperature and pressure. This approach is used for growth of electronics on plastics. However PECVD has a chemical contamination risk. Metal-organic CVD (MOCVD), also called organo-metallic vapor phase epitaxy (OMVPE) is the most common technique to grow epitaxial thin films. These epitaxial films have applications in solar cells, LEDs and quantum wells.

Similar to PVD, CVD enables the growths of crystalline and amorphous semiconductors, metal alloys and compounds with different stoichiometries. Each of these techniques has some advantages over the other approach. PVD films are usually grown at lower temperature and pressure as compared to CVD films and hence grown films with this technique have less contamination. Also, the PVD growth process usually does not involve toxic or corrosive gases and therefore is less dangerous than CVD process. On the other hand CVD has some advantages over PVD. Growth rate at CVD is usually higher than PVD and so this approach is preferred in industry. CVD allows growth of materials that are hard to evaporate and hence cannot be grown by PVD.

2.6 Simulation methods to study growth and annealing of semiconductor heterostructures

Ab-initio techniques has been used to study different aspects of semiconductors during growth and annealing such as surface recombination of heterostructures, strain engineering bandgap energy, and effect of defects on band structures. Here are some examples of studies that have used ab-initio approach. For instance, Kratzer *et al.* [22] used density-functional theory (DFT) to study stable surface reconstructions of GaAs. Specifically, the authors studied the adsorption, diffusion and desorption of Ga atoms. The authors found that Ga atoms are resistant to re-evaporation and hence their mobility determines the homogeneity of the growing layer. In another study, Kratzer *et al.* [23] used DFT in conjunction with kinetic Monte Carlo to

understand the mechanism for epitaxial growth of GaAs and InGaAs. It was reported that under As-rich condition, (2×3) reconstruction is more stable. In contrast, under less As-rich condition $\alpha 2(2 \times 4)$ reconstruction is the most stable one. Kusova *et al.* [24] studied the effect of tensile strain on silicon nanocrystals. They reported that the indirect bandgap of silicon changes to a direct bandgap due to the effect of tensile strain and quantum confinement. Luo *et al.* [25] studied quaternary alloy, $\text{GaAs}_{1-x-y}\text{P}_y\text{Bi}_x$ using DFT. The authors found that bandgap changes of $\text{GaAs}_{1-x-y}\text{P}_y\text{Bi}_x$ relative to GaAs are mainly by local changes in the structure around P and Bi atoms. Janotti *et al.* [26] used DFT to study the effect of defects on band structure of zinc oxide (ZnO). They found oxygen vacancies and zinc vacancies to have the lowest formation energy, while oxygen interstitials and oxygen antisites (on zirconium) have high energies.

Molecular Dynamics (MD) and Kinetic Monte Carlo (KMC) simulations have been used to model the growth of semiconductors. Researchers have used MD and KMC to study growth and formation of defects in heterostructures. Kwon *et al.* [27] studied the growth of amorphous and epitaxial silicon on Si(111) substrate. They reported that low surface diffusivity caused amorphous growth while high surface diffusivity lead to crystalline epitaxial growth. Chuang *et al.* [28] used MD simulations to study the growth of Ge on silicon dioxide. They reported critical size for island nucleation and the scaling of island density as a function of temperature. Srivastava *et al.* [29] studied growth of SiGe film on 2×1 surface reconstruction of Si substrate. Their results suggested a new mechanism for incorporation of adatoms in which diffusing atoms move perpendicular to the dimer rows of original surface. Schulze and Smereka [30] investigated the growth of strained heteroepitaxial structures using Monte Carlo method. They studied the effect of misfit strain and deposition rate on film morphology and formation of islands. Their results suggest a critical misfit strain for formation of islands. The authors also found that smaller values of deposition flux cause formation of larger and more separated islands. Remediakis *et al.* [31] provided a methodology to investigate dislocation energetics in segregated alloys based on KMC.

They extracted core energies for 60° dislocations that are very common in heteroepitaxial SiGe alloys.

Continuum approaches have extensively been used to model microstructural evolution of materials. These microstructural evolutions include morphological, compositional or structural changes in materials. These evolutions take place to reduce the total free energy of the system. Total free energy of a system can include contributions from bulk chemical free energy, interfacial and surface energies, elastic and plastic strain energies, magnetic energy, electrostatic energy, and external forces such as stress, electro-magnetic field, and temperature. Due to complicated nature of these evolution equations, they usually are solved via numerical approaches. In traditional methods to solve the evolution equations of microstructures, the interfaces between different structural or compositional domains are treated as mathematical sharp interfaces and hence the displacements and forces from different fields are calculated at each time step that means external tracking of all internal boundaries. A schematic view of the interfaces where explicit tracking of them is needed in every time step is shown in Fig. 2.11.

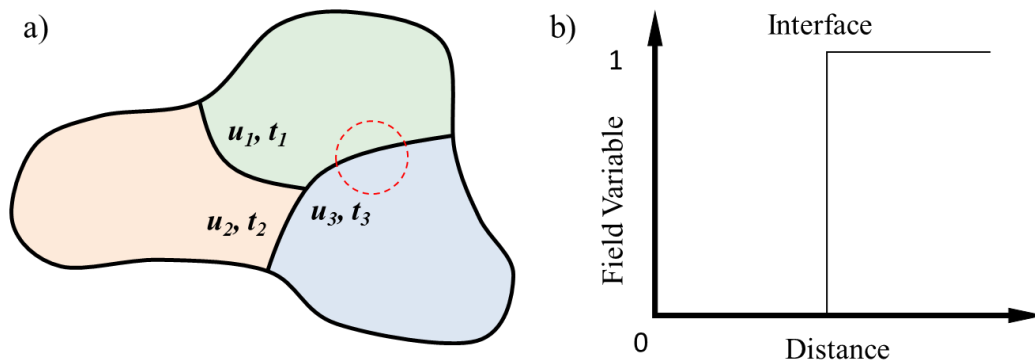


Fig. 2.11 a) Schematic view of different sub-domains inside the main domain. For evolution problems, in addition to solving governing equations in each sub-domain, boundary conditions between all sub-domains (such as displacement field, traction vector, etc.) are needed at each time

step to track the boundaries. b) Schematic view of sharp transition of a variable at an interface from 0 to 1.

Here are a few examples where sharp interface models have been used to study microstructural evolution of material. Tersoff *et al.* [32] studied the growth of multilayer arrays of coherently strained islands using a continuum based sharp interface model. The authors reported that arrangement of islands is not simply repeated from layer to another layer. Instead, the size and spacing between islands grow progressively more uniform by depositing more layers. Spencer *et al.* [33] investigated the effect of compositional stress on stability of strained thin films. It is found that compositional stress always makes alloys more unstable than a single-component film. Tu *et al.* [18] modeled the formation of self-assembled quantum dots using continuum mechanics modeling. The authors investigated the role of intermixing between deposited material and the substrate. It is found that surface morphology and intermixing are strongly coupled and they qualitatively reproduced trench formation and lateral island motion. Katsaros *et al.* [34] showed that nanoscale grooves can control the nucleation of the epitaxial Ge islands on Si substrate. Also, grooves can drive the islands laterally to sit directly on top of trenches. The reason for this lateral motion is that by positioning at the center of the groove minimizes the strain energy. Leontiou *et al.* [35] studied the competition between defect formation and intermixing in strained thin films using continuum modeling and Monte Carlo simulations. Authors reported that strain relaxation by defect formation can suppress the intermixing between film and the substrate.

This explicit tracking of boundaries can be successful in one-dimensional problems, however the simulations become computationally expensive for problems with higher dimensions. To address this problem, phase-field modeling has been developed substantially in past two decades. Phase field modeling is one of the strongest approaches that can be used to model microstructural

evolution of structures. I will discuss phase field modeling approach and its application with more details in chapter 3.

2.7 Reference

- [1] Y. N. Guo *et al.*, *Nano Lett.* **13**, 643 (2013).
- [2] D. J. SROLOVITZ, *Acta Metall.* **37**, 621 (1989).
- [3] R. Notzel, J. Temmyo, and T. Tamamura, *Nature* **369**, 131 (1994).
- [4] R. Notzel, T. Fukui, H. Hasegawa, J. Temmyo, and T. Tamamura, *Appl. Phys. Lett.* **65**, 2854 (1994).
- [5] Q. H. Xie, A. Madhukar, P. Chen, and N. P. Kobayashi, *Phys. Rev. Lett.* **75**, 2542 (1995).
- [6] M. Grundmann *et al.*, 1996 Eighth International Conference on Indium Phosphide and Related Materials, 738 (1996).
- [7] D. S. L. Mui, D. Leonard, L. A. Coldren, and P. M. Petroff, *Appl. Phys. Lett.* **66**, 1620 (1995).
- [8] S. M. Wise, J. S. Lowengrub, J. S. Kim, K. Thornton, P. W. Voorhees, and W. C. Johnson, *Appl. Phys. Lett.* **87**, 133102 (2005).
- [9] J. W. Matthews, A. E. Blakeslee, and S. Mader, *Thin Solid Films* **33**, 253 (1976).
- [10] S. C. Jain, M. Willander, and H. Maes, *Semicond. Sci. Technol.* **11**, 975 (1996).
- [11] C. S. Ozkan, W. D. Nix, and H. J. Gao, *Appl. Phys. Lett.* **70**, 2247 (1997).
- [12] E. A. Fitzgerald, S. B. Samavedam, Y. H. Xie, and L. M. Giovane, *J Vac Sci Technol A* **15**, 1048 (1997).
- [13] E. Luna, M. Wu, J. Puustinen, M. Guina, and A. Trampert, *J. Appl. Phys.* **117**, 185302 (2015).
- [14] K. C. Hsieh, K. Y. Hsieh, Y. L. Hwang, T. Zhang, and R. M. Kolbas, *Appl. Phys. Lett.* **68**, 1790 (1996).
- [15] M. Tang and A. Karma, *Phys. Rev. Lett.* **108**, 265701 (2012).
- [16] P. D. Markowitz, M. P. Zach, P. C. Gibbons, R. M. Penner, and W. E. Buhro, *JACS* **123**, 4502 (2001).

- [17] O. Ueda, S. Isozumi, and S. Komiya, *Jpn J Appl Phys* 2 **23**, 241 (1984).
- [18] Y. Tu and J. Tersoff, *Phys. Rev. Lett.* **98**, 096103 (2007).
- [19] J. W. Matthews and E. Klokholm, *Mater. Res. Bull.* **7**, 213 (1972).
- [20] D. J. Dunstan, *J Mater Sci-Mater El* **8**, 337 (1997).
- [21] L. B. Freund and S. Suresh, *Thin film materials : stress, defect formation, and surface evolution* (Cambridge University Press, Cambridge, England ; New York, 2003).
- [22] P. Kratzer, C. G. Morgan, and M. Scheffler, *Prog. Surf. Sci.* **59**, 135 (1998).
- [23] P. Kratzer, E. Penev, and M. Scheffler, *Appl. Surf. Sci.* **216**, 436 (2003).
- [24] K. Kusova, P. Hapala, J. Valenta, P. Jelinek, O. Cibulka, L. Ondic, and I. Pelant, *Adv Mater Interfaces* **1**, 1300042 (2014).
- [25] G. Luo, K. Forghani, T. F. Kuech, and D. Morgan, *Appl. Phys. Lett.* **109**, 112104 (2016).
- [26] A. Janotti and C. G. Van de Walle, *Phys Rev B* **76**, 165202 (2007).
- [27] I. Kwon, R. Biswas, G. S. Grest, and C. M. Soukoulis, *Phys Rev B* **41**, 3678 (1990).
- [28] C. Y. Chuang, L. A. Zepeda-Ruiz, S. M. Han, and T. Sinno, *Surf. Sci.* **641**, 112 (2015).
- [29] D. Srivastava, B. J. Garrison, and D. W. Brenner, *Langmuir* **7**, 683 (1991).
- [30] T. P. Schulze and P. Smereka, *Commun Comput Phys* **10**, 1089 (2011).
- [31] I. N. Remediakis, D. E. Jesson, and P. C. Kelires, *Phys. Rev. Lett.* **97**, 255205 (2006).
- [32] J. Tersoff, C. Teichert, and M. G. Lagally, *Phys. Rev. Lett.* **76**, 1675 (1996).
- [33] B. J. Spencer, P. W. Voorhees, and J. Tersoff, *Phys. Rev. Lett.* **84**, 2449 (2000).
- [34] G. Katsaros, J. Tersoff, M. Stoffel, A. Rastelli, P. Acosta-Diaz, G. S. Kar, G. Costantini, O. G. Schmidt, and K. Kern, *Phys. Rev. Lett.* **101**, 096103 (2008).
- [35] T. Leontiou, J. Tersoff, and P. C. Kelires, *Phys. Rev. Lett.* **105**, 236104 (2010).

Chapter 3 Method

3.1 Phase field method

Phase field is a diffuse-interface model that has been proposed by Van der Walls [1] more than a century ago and developed by Cahn and Hilliard more than 50 years ago [2]. In diffuse-interface models, the microstructure is represented by phase field variables that are continuous in time and spaces. In phase field model, interfaces are represented by variables that change continuously from one side of the interface to the other side unlike the abrupt transition across the boundaries in sharp-interface models. For instance, let's imagine a system with three different phases (orange, blue and green) as shown in Fig. 3.1a. Within each phase, phase field variables are constant values. These variables vary continuously across the boundaries. Variation of Φ_3 across the interface is shown in Fig. 3.1b. In diffuse-interface models, there is no need to track the boundaries explicitly and hence this method is computationally efficient for problems with complex microstructure that evolve in time. Also, this method can be used to model non-equilibrium processes by imposing no flux boundary conditions at the boundaries. Nowadays phase fields models have been applied to many different mesoscale level problems such as solidification [3-5], phase transformation [6-8], thin film growth [9,10], crack formation and propagation [11-13], dislocation dynamics [14-16] and even some biological applications [17,18].

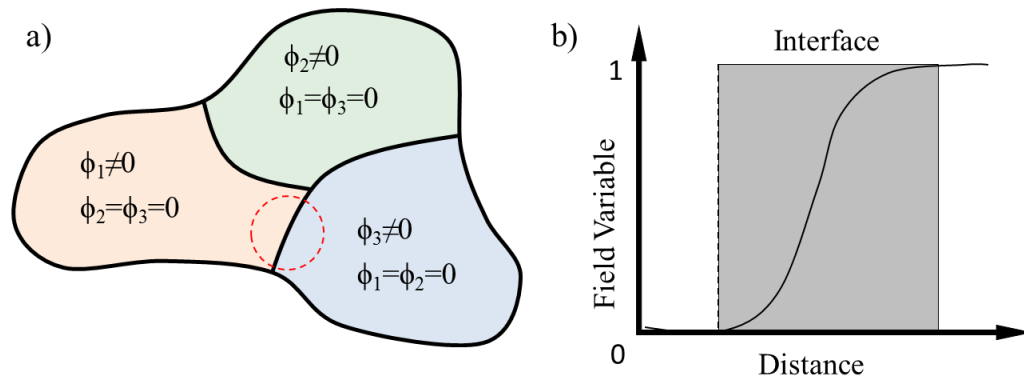


Fig. 3.1 a) Phase field variables: constant values inside a domain, continuous transition at the interfaces. b) Schematic view of transition of a phase field variable at an interface from 0 to 1.

Phase field method uses two types of variables to describe the microstructural evolution of a system. These are conserved variables and non-conserved variables. Conserved variables are usually related to the local composition and have to satisfy a local conservation constraint. Non-conserved variables usually contain information about the structure and orientation. There are three main variables in phase field model: composition variables (conserved), order parameters (non-conserved), and phase fields (non-conserved).

Composition variables such as concentration, density, and molar fraction are examples of conserved variables [19]. For instance, let's imagine a system with c components where n_i is the number of moles of each component and $i=1, 2 \dots c$. Molar fraction x_i and molar concentration c_i of each component are defined as

$$x_i = \frac{n_i}{n_{tot}} \quad 3-1$$

$$c_i = \frac{n_i}{V_{tot}} = \frac{x_i \cdot n_{tot}}{V_{tot}} = \frac{x_i}{V_m} \quad 3-2$$

where V_{tot} is the total volume, n_{tot} is the total number of moles in system and V_m is the molar volume. At each particular position in the system, one can write

$$\sum_{i=1}^c x_i = 1 \quad 3-3$$

$$\sum_{i=1}^c n_i = \frac{1}{V_m} \quad 3-4$$

In a closed system, the total number of moles of each component is conserved and hence the evolution of these variables are constrained by

$$\int_V c_i \, dr = \int_V \frac{x_i}{V_m} \, dr = \text{const.} \quad 3-5$$

Order parameters (η) are non-conserved variables that are used to distinguish crystal symmetry relations between coexisting phases with different structures. These order parameters can be used to study second-order phase transformations and anti-phase boundaries [19]. For instance, Fig. 3.2 shows a phase transformation from cubic structure to tetragonal structure that represents a symmetry reduction in the structure. Three order parameters are needed to describe phase transformation since tetragonal structure has three orientations that are energetically equivalent [19]. Order parameters can also be used to describe the grain growth evolution and coarsening in microstructure [20-22].

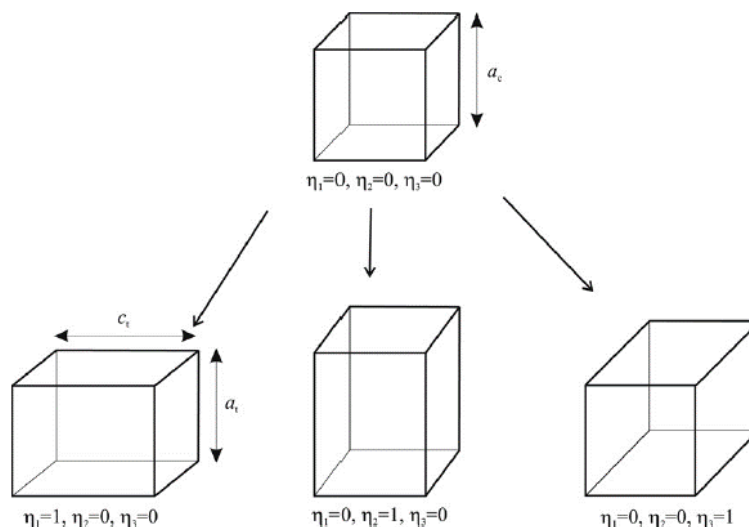


Fig. 3.2 Phase transformation from cubic to tetragonal structure. Since tetragonal structure has three different orientations that are energetically equivalent, three order parameters (η_1, η_2 and η_3)

are needed to model the transformation. a_c , a_t and c_t are lattice parameters of cubic and tetragonal structure [19].

Phase fields (φ) are used to distinguish between two different phases of a material. For instance in a solid-gas system phase field variable φ is 0 in gas phase, 1 in solid phase, and it continuously varies between 0 and 1 in the interface region. The phase field concept can also be applied to solid state phase transformation such as phase transformation in steel between austenite and ferrite phases [19].

Temporal evolution of phase field variables is described by a set of partial differential equations and these equations are usually solved numerically. Total free energy of a microstructure is comprised of such terms such as bulk energy, interfacial energy, and strain energy. Total free energy is a function of conserved and non-conserved variables and can be written as follows

$$F = F_{bulk} + F_{int} + F_{elastic} + F_{plastic} \quad 3-6$$

$$F = \int_{\Omega} \left(f_0(c_1, c_2, \dots, c_n, \eta_1, \eta_2, \dots, \eta_n, \varphi_1, \varphi_2, \dots, \varphi_n) + \sum_{i=1}^n \frac{\varepsilon^2}{2} |\nabla c_i|^2 + \sum_{i=1}^n \frac{\alpha^2}{2} |\nabla \eta_i|^2 + \sum_{i=1}^n \frac{\beta^2}{2} |\nabla \varphi_i|^2 \right) d\Omega + \int_R W_i(c_1, c_2, \dots, c_n, \eta_1, \eta_2, \dots, \eta_n, \varphi_1, \varphi_2, \dots, \varphi_n) dR. \quad 3-7$$

The above total free energy of the system consists of two integrals, and each of them is discussed below in detail. The first integral on the right hand side (rhs) of Eq. (3-7) represents short-range chemical interactions including bulk energy and interfacial energy [23]. The second integral represents long-range interactions (W_i) such as elastoplastic, electrostatic, magnetic interactions. Ω and R represent the volume of system. f is the local free energy density that is a function of conserved variables (c) and non-conserved variables (η and φ). ε^2 , α^2 and β^2 are the

gradient energy coefficients. Driving force for the microstructural evolution is to reduce the total free energy of a system.

Bulk free energy density is the first term in total free energy functional represented in Eq. (3.7) which determines the composition and volume fractions of equilibrium phases. This free energy has units of J/m^3 and can be in general written as $f_0 = f_0(c, \eta, \varphi)$. Free energy density can be determined based on the common tangent to f_0 as shown in Fig. 3.3. Bulk free energy density has minima at equilibrium states of the system. Common tangent is usually used for conserved variables such as concentration (see Fig. 3.3a). For non-conserved variables such as order parameters and phase fields, the minima in free energy density represent equivalent variants of the ordered structure and hence the free energy density is assumed to be zero at these minima. The difference between common tangent line and the double wellled free energy density (shown as Δf_0 in Fig. 3.3) corresponds to interfacial energy and hence needs to be reduced from bulk energy F_{bulk} and added to interfacial energy F_{int} .

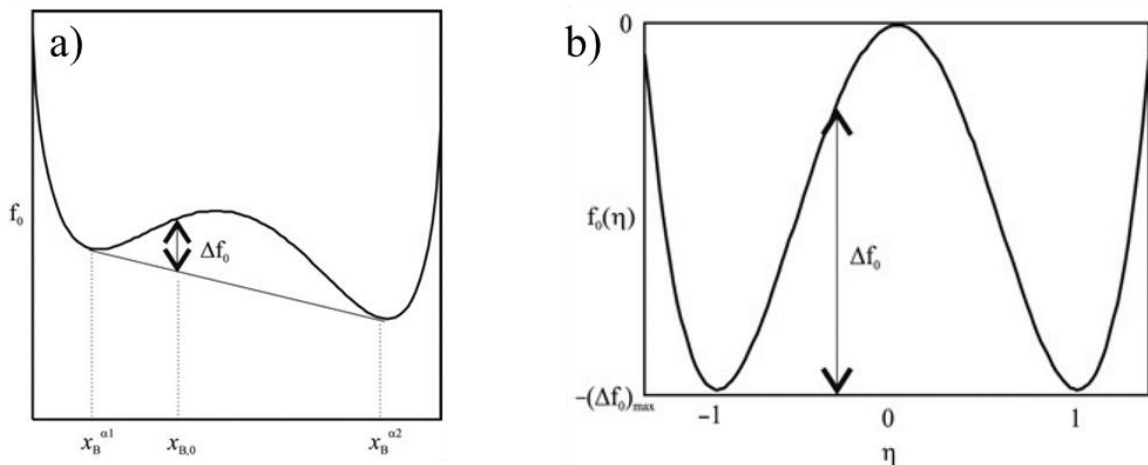


Fig. 3.3 a) Bulk free energy density as a function of molar fraction (x). There are two minima at $x_B^{\alpha 1}$ and $x_B^{\alpha 2}$ where a common tangent between those minima represents the energy of stable phases in between these two minima. b) Bulk free energy density as a function of order parameter (η) with minima at $\eta = \pm 1$ [19].

As previously mentioned, bulk free energy F_{bulk} can be a function of different phase field variables (conserved and non-conserved). However, for simplicity, I will use only one order parameter (phase field) in bulk free energy density formulation from now on. If multiple concentrations and order parameters and phase fields are introduced in the system, the bulk free energy density will have some cross product terms. It has been reported that bulk free energy of systems with only one variable could be represented by a polynomial [19,23]. Landau was one of the first researchers to propose a polynomial to represent bulk free energy density [24]. When only two stable phases are allowed, a fourth-order polynomial is used.

$$F_{bulk} = \int_V f_0(\varphi) dV = \int_V (A_0 + B_0\varphi + C_0\varphi^2 + D_0\varphi^3 - \Delta f_0(\varphi)) dV. \quad 3-8$$

Assuming minima at $\varphi = 0$ and $\varphi = 1$, symmetric free energy around $\varphi = 0.5$ and $f_0(\varphi = 0) = 0$, a double well free energy density is found as follows

$$F_{bulk} = \int_V \left(\frac{1}{4} w_0 \varphi^2 (1 - \varphi)^2 - \Delta f_0(\varphi) \right) dV. \quad 3-9$$

In Eq. (3-9) free energy density is zero at $\varphi = 0$ and $\varphi = 1$ and has maximum of $w_0/64$ at $\varphi = 0.5$. A double-welled bulk free energy is plotted in Fig. 3.4. Sixth-order polynomials are used where three stable phases are allowed.

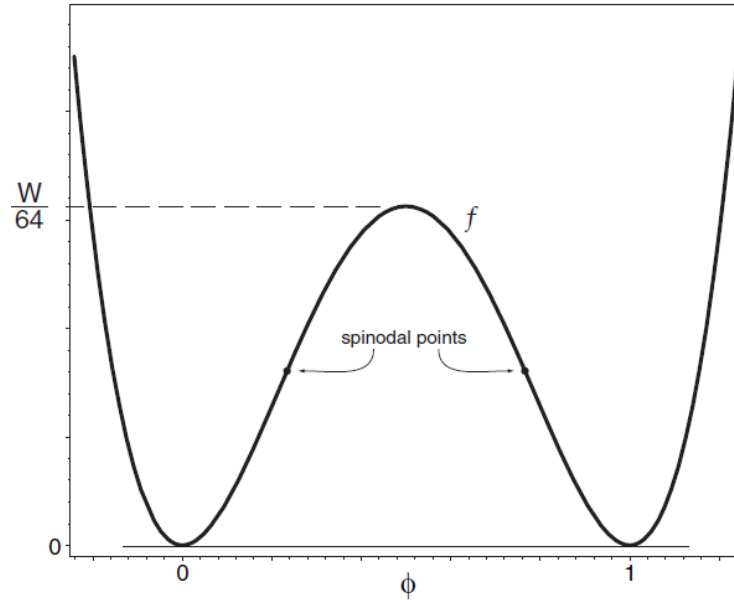


Fig. 3.4 Double-welled free energy density function [9]. This free energy density function describes a case where there are two thermodynamically stable phases at $\varphi=0$ and $\varphi=1$. The barrier height of free energy functional $W/64$ is calculated from interfacial thickness and interfacial energy as shown in Eqs. (3-12) and (3-13).

The interfacial energy F_{int} of a system with bulk free energy as shown in Eq. (3-9) can be written as

$$F_{int} = \int_V (\Delta f_0(\varphi) + \frac{\beta^2}{2} |\nabla \varphi_i|^2) dV \quad 3-10$$

Δf_0 is the same term as used in Eq. (3-9). Hence the sum of bulk and interfacial energy for a system with one order parameter can be written as

$$F_{bulk} + F_{int} = \int_V (\frac{1}{4} w_0 \varphi^2 (1 - \varphi)^2 + \frac{\beta^2}{2} |\nabla \varphi_i|^2) dV. \quad 3-11$$

For this free energy density, one can find the relationship between interfacial energy γ_{int} (J/m²) and phase field parameters w_0 and β [9].

$$\gamma_{int} = \frac{\beta}{6} \sqrt{\frac{w_0}{2}} \quad 3-12$$

$$\delta = \beta \sqrt{\frac{2}{w_0}}. \quad 3-13$$

Second integral on the rhs of Eq. (3-7) includes long-range interactions, such as electrostatic, magnetic and elastic strain. In this study, I consider the long-range contributions from elastic energy density. Assuming that both elastic and plastic free energies are only a function of concentration (c), they can be defined as

$$F_{elastic} + F_{plastic} = \int_R W_i(c) dR = \int_R (W^{el}(c) + W^{pl}(c)) dR \quad 3-14$$

where $W_i(c)$ is the total work, $W^{pl}(c)$ is the plastic work

$$W^{pl}(c) = \int_0^{e^{pl}} \sigma_{ij} de_{ij}^{pl} \quad 3-15$$

e_{ij}^{pl} is plastic strain tensor and σ_{ij} is the Cauchy stress tensor. $W^{el}(c)$ is the elastic work that can be written as

$$W^{el}(c) = \int_0^{e^{el}} \sigma_{ij} de_{ij}^{el} = \frac{1}{2} \sigma_{ij} e_{ij}^{el} \quad 3-16$$

here e_{ij}^{el} is an elastic strain tensor, which can be given as

$$e_{ij}^{el} = e_{ij}^{tot} - e_{ij}^* - e_{ij}^{pl} \quad 3-17$$

e_{ij}^{tot} is the total strain, and e_{ij}^* is the eigenstrain associated with the difference between lattice parameters of the film and the substrate. Assuming a linear strain displacement relationship, the total strain can be written as

$$e_{ij}^{tot} = \frac{1}{2}(u_{i,j} + u_{j,i}) \quad 3-18$$

$u_{i,j}$ is the derivative in the j direction of the displacement in i direction. Assuming that mechanical equilibrium is reached much faster than chemical equilibrium, the total strain is calculated by solving the mechanical equilibrium (Cauchy-Navier) equation

$$\frac{\partial \sigma_{ij}}{\partial x_j} = 0. \quad 3-19$$

Stress is related to the elastic strain as follows:

$$\sigma_{ij} = C_{ijkl} e_{kl}^{el} = C_{ijkl} (e_{ij}^{tot} - e_{ij}^* - e_{ij}^{pl}) \quad 3-20$$

where C_{ijkl} is the elastic modulus and in general is a function of the order parameter φ since coexisting phases usually have different elastic properties. Eigenstrain in our model is defined as

$$e_{ij}^* = \hat{e}_f \delta_{ij} \quad 3-21$$

here δ_{ij} is Kronecker delta and \hat{e}_f is the lattice mismatch which is given by

$$\hat{e}_f = \frac{a_{film} - a_{substrate}}{a_{substrate}}. \quad 3-22$$

To find the plastic strain tensor I need to define a yield function, a flow rule, and a hardening rule. Here, I use $J2$ plasticity (Von-Mises criterion) with the yield function

$$F(\sigma_{ij}, \sigma_Y) = \sigma_{mises} - \sigma_Y \leq 0 \quad 3-23$$

F is the yield function, σ_Y is the current yield stress, and σ_{mises} is the Von-Mises stress. For isotropic hardening, flow rule is given by

$$\dot{e}_{ij}^{pl} = \lambda \frac{\partial F(\sigma_{ij}, \sigma_Y)}{\partial \sigma_{ij}} \quad 3-24$$

where \dot{e}_{ij}^{pl} is the plastic strain rate and λ is plastic multiplier, which is a positive number. For the film and the substrate materials I assume a linear work hardening, which can be written as

$$\sigma_Y = \sigma_{Y0} + \sigma_h \quad 3-25$$

here σ_{Y0} is the initial yield stress and σ_h is the work hardening function

$$\sigma_h = E_t \cdot e^{pl} \quad 3-26$$

E_t is the slope of stress-strain curve after linear elastic regime, which is also called tangential Young's modulus.

In the phase field model, temporal evolution of variables that represents the morphological evolution of the system is determined by solving a system of coupled partial differential equations. There is one such equation for each variable. These equations are chosen in a way that the free energy of the system decreases monotonically. Solving these equations provides the temporal evolution of the variables. There are two main types of evolution equations: Allen-Cahn (Ginzburg-Landau) [25] equation that is used to track the evolution of non-conserved variables, and Cahn-Hilliard [2] equation that models the evolution of conserved variables.

Allen-Cahn equation governs non-conserved variables such as phase fields (φ_k) and order parameters (η_k) as follows

$$\frac{\partial \varphi_k}{\partial t} = -L_k(\varphi_k) \frac{\delta F}{\delta \varphi_k} = -L_k(\varphi_k) \left(\frac{\delta f_0}{\delta \varphi_k} - \nabla \cdot (\beta_k^2 \nabla \varphi_k) + \frac{\partial W_i}{\partial \varphi_k} \right) \quad 3-27$$

$$\frac{\partial \eta_k}{\partial t} = -L_k(\eta_k) \frac{\delta F}{\delta \eta_k} = -L_k(\eta_k) \left(\frac{\delta f_0}{\delta \eta_k} - \nabla \cdot (\alpha_k^2 \nabla \eta_k) + \frac{\partial W_i}{\partial \eta_k} \right) \quad 3-28$$

where $k = 1, 2, \dots, p$ represents different order parameters and f_0 is the bulk free energy density which in general is a function of all conserved and non-conserved variables. β_k is the gradient energy coefficient and L_k is the mobility. Both these coefficients may depend on conserved or non-conserved variables to represent anisotropy. In case that only one non-conserved variable φ exists, evolution equation can be written as

$$\frac{\partial \varphi}{\partial t} = -L \frac{\delta F}{\delta \varphi} = -L(\varphi) \left(\frac{\delta f_0}{\delta \varphi} - \nabla \cdot (\beta^2 \nabla \varphi) \right). \quad 3-29$$

To model anisotropy, one needs to define the gradient energy coefficient as a function of orientation. This topic will be discussed later in this chapter.

Cahn-Hilliard equation governs evolution of conserved variables such as density, molar fraction, and concentration. For instance, let us consider a case where concentration (c) is the only conserved field variable. Concentration evolves according to the mass conservation equation

$$\frac{\partial c}{\partial t} = -\nabla \cdot J \quad 3-30$$

J is the density flux, which can be related to the gradient of variational derivative of the free energy density functional as

$$\begin{aligned} J &= -M(c) \nabla \frac{\delta F}{\delta c} = -M(c) \nabla \left(\frac{\partial f}{\partial c} - \nabla \cdot (\varepsilon^2 \nabla c) + \frac{\partial W_i}{\partial c} \right) = \\ &-M(c) \nabla \left(\frac{\partial f}{\partial c} - \nabla \cdot (\varepsilon^2 \nabla c) + \frac{\partial W^{el}}{\partial c} + \frac{\partial W^{pl}}{\partial c} \right) \end{aligned} \quad 3-31$$

where $\frac{\delta}{\delta c}$ is a variational derivative. The plasticity driving force on concentration field is $\frac{\partial W^{pl}}{\partial c}$.

Since the majority of the plastic work in crystalline systems is released as heat, I assume that the effect of plastic work as driving force for evolution of the concentration field is negligible. I previously discussed that anisotropy in interfacial energies can be incorporated in the gradient energy coefficients. Following the formulation developed by Egglestone *et al.* [9], anisotropic interfacial energy can be defined as

$$\varepsilon(\theta) = \varepsilon_0 (1 + \varepsilon_4 \cos(4\theta)) \quad 3-32$$

where ε_0 is the gradient energy constant, θ is the angle between the normal to the contour of constant concentration and the x -axis and ε_4 is a constant between 0 to 1, which determines the degree of anisotropy. The variation of ε_4 with distance from the substrate has been adopted from Egglestone *et al.* [9]. Using anisotropic interfacial energy, the flux can be written as

$$J = -M(c) \nabla \left(\frac{\partial f}{\partial c} - \nabla \cdot (\varepsilon^2 \nabla c) + \frac{\partial W^{el}}{\partial c} + \frac{\partial}{\partial x} \left(\varepsilon \frac{d\varepsilon}{d\theta} \frac{\partial c}{\partial y} \right) - \frac{\partial}{\partial y} \left(\varepsilon \frac{d\varepsilon}{d\theta} \frac{\partial c}{\partial x} \right) \right) \quad 3-33$$

where ε_4 is a positive constant smaller than 1/15.

There are two main kinetic terms that have been included in the phase field model in this thesis in order to model growth and annealing of semiconductor heterostructures. One term represents the effect of diffusivity (both surface and bulk diffusivities), which is incorporated in the model through $M(c)$. $M(c)$ is called mobility and depends on the concentration in the following way

$$M(c) = M_s c^2 (1 - c)^2 \quad 3-34$$

where M_s is the surface mobility and for ideal solution is equal to

$$M_s = \frac{D_0 V_m}{RT} \quad 3-35$$

here D_0 is surface diffusivity, R is the gas constant, T is temperature in Kelvin. The second kinetic effect is related to the deposition flux during film growth

$$\frac{\partial c}{\partial t} = -\nabla \cdot J + J_d n_y \quad 3-36$$

where J_d is the deposition flux and n_y is the vertical component of the surface normal. J_d is defined as [9]

$$J_d = V_d A_0 R_0 c^2 (1 - c)^2 \quad 3-37$$

where V_d is the surface velocity (growth rate) due to deposition, R_0 is a random number between 0.95 to 1.05, and $A_0 = \frac{6}{\delta}$, where δ is the interfacial thickness.

Combining Eqs. (3-33) and (3-36), one can derive the following Cahn-Hilliard equation [26]

$$\frac{\partial c}{\partial t} = \nabla \cdot \left[M(c) \nabla \left(\frac{\partial f}{\partial c} + \frac{\partial W^{el}}{\partial c} - \nabla \cdot (\varepsilon^2 \nabla c) + \frac{\partial}{\partial x} \left(\varepsilon \frac{d\varepsilon}{d\theta} \frac{\partial c}{\partial y} \right) - \frac{\partial}{\partial y} \left(\varepsilon \frac{d\varepsilon}{d\theta} \frac{\partial c}{\partial x} \right) \right) \right] + J_d n_y. \quad 3-38$$

Note that in this work, the coupling between plasticity and microstructural evolution is only through the elastic driving force, which is an approach often taken in the literature [27]. To make Eq. (3-38) non-dimensional, I use l^* as the characteristic length, e^* as the characteristic energy density, and t^* as the characteristic time. Using these dimensionless parameters, I define other

dimensionless quantities, which are free energy density ($f^* = \frac{f}{e^*}$), elastic moduli ($C_{ij}^* = \frac{C_{ij}}{e^*}$), strain energy density ($W^* = \frac{W}{e^*}$), gradient energy coefficient ($\varepsilon^{*2} = \frac{\varepsilon^2}{l^{*2}e^*}$), mobility ($M^* = \frac{M_s t^* e^*}{l^{*2}}$), and deposition flux rate ($J_d^* = t^* J_d$). I can also write a dimensionless form of the Cahn-Hilliard equation

$$\frac{\partial c}{\partial \hat{t}} = \nabla \cdot \left[M^*(c) \nabla \left(\frac{\partial f^*}{\partial c} + \frac{\partial W^{el^*}}{\partial c} - \nabla \cdot (\varepsilon^{*2} \nabla c) + \frac{\partial}{\partial \hat{x}} \left(\varepsilon^* \frac{d\varepsilon^*}{d\theta} \frac{\partial c}{\partial \hat{y}} \right) - \frac{\partial}{\partial \hat{y}} \left(\varepsilon^* \frac{d\varepsilon^*}{d\theta} \frac{\partial c}{\partial \hat{x}} \right) \right) \right] + J_d^* n_y \quad 3-39$$

where the ∇ symbol represents a gradient with respect to non-dimensional variables \hat{x} and \hat{y} .

Eq. (3-39) is a fourth order partial differential equation (PDE) and hence needs to be solved numerically. In this section, I discuss two possible approaches that have been used to solve these types of equations: finite difference method and finite element method.

3.2 Numerical methods to solve governing equations

3.2.1 Finite difference method

Finite difference method (FDM) is one of the techniques to find solution for non-linear PDEs. In this method, the simulation domain is divided into small areas using a mesh (e.g., see the 2D domain shown in Fig. 3.5). Points at the intersection of the mesh lines are called grid points. Positions of these points in 2D domain is represented by two variables i and j . The value of function U at the point (i,j) is represented by $U(i,j)$. The value of U at any grid point with a small distance away from point (i,j) can be calculated in terms of the function U and its derivatives at (i,j) using Taylor expansion. I assume the mesh size in $x(h_i)$ and $y(h_j)$ directions to be the same and equal to h for simplicity. $U(i \pm mh_i, j \pm nh_j)$ is found as follows

$$U(i \pm mh, j \pm nh) = U(i, j) \pm mh \frac{\partial U(i, j)}{\partial x} \pm nh \frac{\partial U(i, j)}{\partial y} \pm \frac{(mh)^2}{2!} \frac{\partial^2 U(i, j)}{\partial x^2} \pm \frac{(nh)^2}{2!} \frac{\partial^2 U(i, j)}{\partial y^2} \pm \frac{(mh)^3}{3!} \frac{\partial^3 U(i, j)}{\partial x^3} \pm \frac{(nh)^3}{3!} \frac{\partial^3 U(i, j)}{\partial y^3} \pm h(O^4). \quad 3-40$$

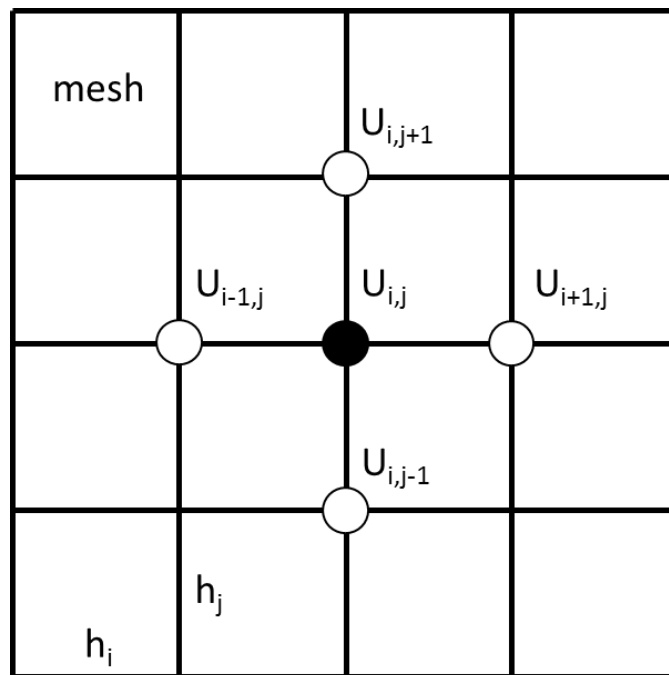


Fig. 3.5 Meshing is a process of dividing a domain in small elements where there are grid points at the corners of each element. h_i and h_j show the length of each element in x and y directions. $U(i,j)$ represents the value of function U at grid point (i,j) .

Assuming $h=1$ for simplicity, one can find $U(i-1,j)$ and $U(i+1,j)$ from Eq. (3-40). By subtracting $U(i-1,j)$ from $U(i+1,j)$, one can find the value of derivative of U at point (i,j) as follows

$$\frac{\partial U(i,j)}{\partial x} = \frac{U(i+1,j) - U(i-1,j)}{2h} + \left[\frac{h^2}{6} \frac{\partial^3 U(i,j)}{\partial x^3} + O(h^4) \right]. \quad 3-41$$

By neglecting the higher order terms in the square brackets of the above equation, one can find an estimate for the first derivative of function U in x direction.

$$\frac{\partial U(i,j)}{\partial x} \approx \frac{U(i+1,j) - U(i-1,j)}{2h} \quad 3-42$$

which has an error of $O(h^2)$. This derivative is called the Centered Finite Difference derivative. A similar method can be used to find other derivatives in the problem, such as the time derivative at $t_p = t_0 + p \cdot \Delta t$ where t_0 is initial time, Δt is time step and p is an integer. This time derivative takes the form

$$\frac{\partial U^p(i,j)}{\partial t} = \frac{U^{p+1}(i,j) - U^p(i,j)}{\Delta t} + O(\Delta t). \quad 3-43$$

The above method is called forward Euler differencing. The advantage of the Forward Euler approach is that the value of function at time step $p+1$ is only determined based on values from step p and hence this method is an example of an explicit approach. The drawback of this method is that it is first order approximation in time step and therefore it is less accurate than the Centered Finite Difference derivative, which is based on a second order approximation. Looking at Eq. (3-39), one can find $\nabla \cdot \nabla = \nabla^2$ is a higher order operator called Laplacian. The Laplacian of function V at point (i,j) can be calculated as the finite difference

$$\nabla^2(V^p) = \frac{V^p(i+1,j) + V^p(i-1,j) + V^p(i,j+1) + V^p(i,j-1) - 4V^p(i,j)}{h^2}. \quad 3-44$$

By combining Forward Euler for time differentiation, Centered Finite Difference for spatial differentiation, and finite difference form for Laplacian one can write Eq. (3-39) as

$$\begin{aligned} \frac{c^{p+1}(i,j) - c^p(i,j)}{\Delta t} &= M^*(c) \nabla^2 \left(\frac{W_0}{2} \left(2(c^p(i,j))^3 - 3(c^p(i,j))^2 + c^p(i,j) \right) + \frac{\partial W^{el^*}}{\partial c} - \right. \\ &\varepsilon^* \frac{c^p(i+1,j) + c^p(i-1,j) + c^p(i,j+1) + c^p(i,j-1) - 4c^p(i,j)}{h^2} + \frac{\partial}{\partial \hat{x}} \left(\varepsilon^* \frac{d\varepsilon^*}{d\theta} \frac{c(i,j+1) - c(i,j-1)}{2h} \right) - \\ &\left. \frac{\partial}{\partial \hat{y}} \left(\varepsilon^* \frac{d\varepsilon^*}{d\theta} \frac{c(i+1,j) - c(i-1,j)}{2h} \right) \right) + J^*_d n_y. \end{aligned} \quad 3-45$$

Assuming $G(i,j) = \varepsilon^* \frac{d\varepsilon^*}{d\theta} \frac{c(i,j+1) - c(i,j-1)}{2h}$ and $H(i,j) = \varepsilon^* \frac{d\varepsilon^*}{d\theta} \frac{c(i+1,j) - c(i-1,j)}{2h}$, one can plug

Eq. (3-42) into Eq. (3.45) to get

$$\frac{c^{p+1}(i,j)-c^p(i,j)}{\Delta t} = M^*(c)\nabla^2 \left(\frac{W_0}{2} \left(2(c^p(i,j))^3 - 3(c^p(i,j))^2 + c^p(i,j) \right) + \frac{\partial W^{el*}}{\partial c} - \right. \\ \left. \varepsilon^* 2 \frac{c^p(i+1,j)+c^p(i-1,j)+c^p(i,j+1)+c^p(i,j-1)-4c^p(i,j)}{h^2} + \frac{G(i+1,j)-G(i-1,j)}{2h} - \frac{H(i,j+1)-H(i,j-1)}{2h} \right) + J^*_d n_y .$$

3-46

3.2.2 Finite element method

Another method to numerically solve governing equations is the finite element method (FEM). FEM is widely used in the fields of fluid mechanics, solid mechanics, structural dynamics, heat transfer and many other fields of engineering and mathematics.

A schematic view of a simulation domain with prescribed boundary conditions is shown in Fig. 3.6a. For simplicity, I assume that a single field variable $\varphi(x,y)$ is the only unknown in the domain of interest. To solve for $\varphi(x,y)$, one needs to divide the domain into elements with finite size, which is similar to FDM. The differences between FEM and FDM will be discussed later. As an example, a single element with three nodes is shown in Fig. 3.6a. In the FEM, the value of field variable is calculated at each of the nodes. Then the value of the field variable is calculated everywhere inside the element using the approximation

$$\varphi(x,y) = N_1(x,y)\varphi_1 + N_2(x,y)\varphi_2 + N_3(x,y)\varphi_3 \quad 3-47$$

where $\varphi_1, \varphi_2, \varphi_3$ are values of the field variables at the nodes and N_1, N_2, N_3 are interpolation functions. The nodal values are unknown constants to be determined and interpolation functions are usually polynomials with independent variables such as material properties. Smaller elements are usually used near the boundaries and at the points with force concentration to increase the accuracy of the approximation. Fig. 3.6b schematically shows how smaller and larger elements can be used incorporated in one simulation domain.

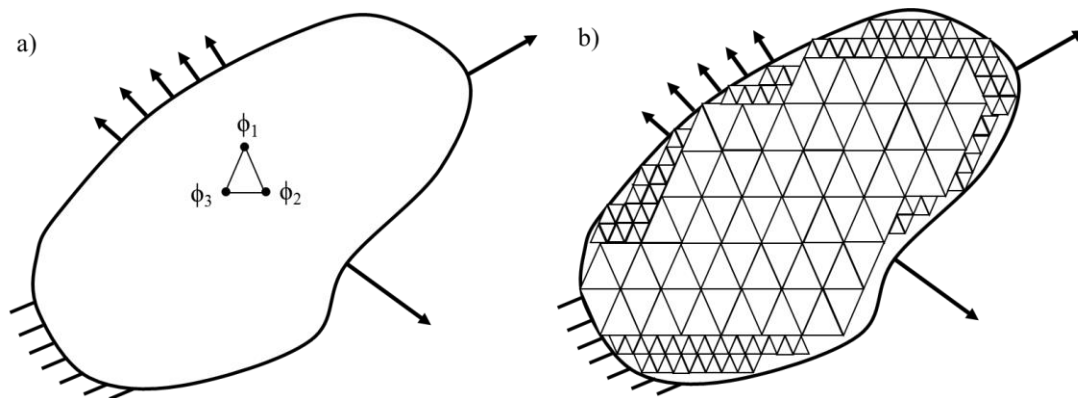


Fig. 3.6 a) 2D domain of variable $\varphi(x,y)$ with a 3-node mesh. ϕ_1 , ϕ_2 and ϕ_3 are nodal values of the variable φ . b) Elements with different sizes can be used in the same domain. To solve the problem, one needs to fully populate the domain with elements.

For structural applications (e.g. truss bridges, elastic bars), simple elements such as spring and bar are often used. The governing equations for these systems are usually algebraic equations, which explicitly include the relationship between force and displacement. However, for non-structural applications the governing equations are usually in the form of differential equations. Due to the complexities from geometry and loading in non-structural problems, rarely there are exact solutions for the governing equations and so approximate solutions are indispensable. FEM uses approximate techniques to solve for these differential equations. One of these methods is called Weighted Residuals Method (WRM). WRM is an approximate technique to solve for boundary value problems using trial functions that satisfy the boundary conditions. The nodal values of unknowns are found by satisfying constraints that minimize the average error in the entire simulation domain. For instance, given a general form of one dimensional homogenous differential equation

$$D[y(x), x] = 0, \quad a < x < b \quad 3-48$$

$$y(a) = y(b) = 0. \quad 3-49$$

WRM seeks an approximate solution in the form of

$$y^*(x) = c_i n_i(x) \quad 3-50$$

where $y^*(x)$ is an approximate solution for $y(x)$, c_i are constant unknown parameters, and $n_i(x)$ is an admissible trial function. Admissible trial function is continuous in the domain and satisfies the boundary conditions. Index i shows number of terms included in the trial solution and it follows Einstein notation convention. Given that the requirements for choosing these functions are not very restrictive, it is unlikely that these equations provide the exact solution. Hence, plugging in these functions into the differential equation results in a residual error $R(x)$

$$R(x) = D[y^*(x), x] = D[c_i n_i(x), x] \quad 3-51$$

In WRM, unknowns (c_i) are found by solving following equations (i equations)

$$\int_a^b w_i(x) R(x) dx = \int_a^b w_i(x) D[c_i n_i(x), x] dx = 0 \quad 3-52$$

where $w_i(x)$ is the weight function. In the so-called Galerkin's global weighted residual method, which is one of the most commonly used techniques in the FEM, the weight functions are chosen to be identical to the trial functions. To find the unknown constants c_i , one needs to solve the following algebraic equations

$$\int_a^b N_i(x) R(x) dx = 0. \quad 3-53$$

The above Galerkin method is often referred to as the classical approach. Since this approach requires trial functions that are valid in the entire domain, it will be difficult to find such functions in two and three-dimensional problems. Consequently, Galerkin's global approach has been adapted (for simplicity I will call it local Galerkin from now on) to be able to solve a system of partial differential equations in higher dimensions. In local Galerkin method, I divide the simulation domain into M elements and $M+1$ nodes (in this 1D example). The approximate solution of governing equation is

$$y^*(x) = \sum_{i=1}^M y_i N_i(x) \quad 3-54$$

where y_i is the value of solution function at $x=x_i$ and $N_i(x)$ is the corresponding trial function. There are two main differences between local Galerkin method and a general WRM. First, the trial functions in local Galerkin approach are only non-zero on a small part of the entire domain. Second, the unknown coefficients (c_i) in the general WRM approach become unknown values of solution function y evaluated at nodes. Substitution of Eq. (3-54) into Eq. (3-53) yields $M+1$ algebraic equations where these equations can be written in the matrix form as

$$[K]\{u\} = \{f\} \quad 3-55$$

where $[K]$ is stiffness matrix, u is global vector of nodal displacements and f is global vector of nodal forces.

Interpolation functions are usually chosen to be polynomials. These functions determine the accuracy of the FEM in an element. Higher order polynomials provide better estimates for the governing equations, but are computationally more expensive than lower order polynomials. Interpolation functions determine the number of nodes needed on each element as well. For example, I have shown triangular elements with different interpolation functions in Fig. 3.7.

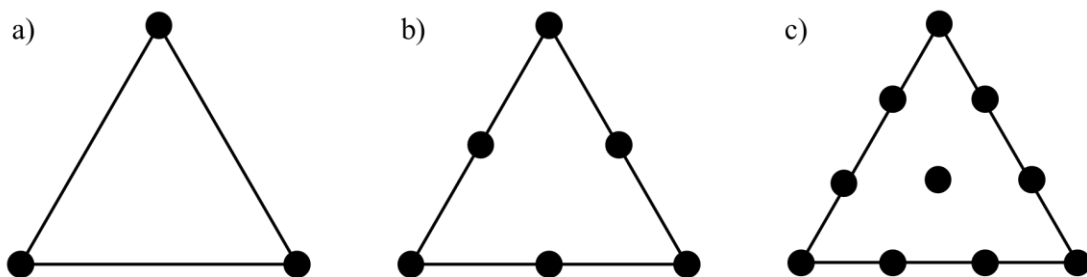


Fig. 3.7 Triangular elements: a) 3-node element with a linear interpolation function. b) 6-node element with a quadratic interpolation function. c) 10-node element with a cubic interpolation function. Interpolation functions with higher orders provide higher accuracy to numerical approximations.

Interpolation functions for each of the above elements can be found in terms of the area coordinates. These coordinates are defined as the ratio of subdomain areas (A_1 , A_2 and A_3) to the total area (A) of the element as shown in Fig. 3.8a.

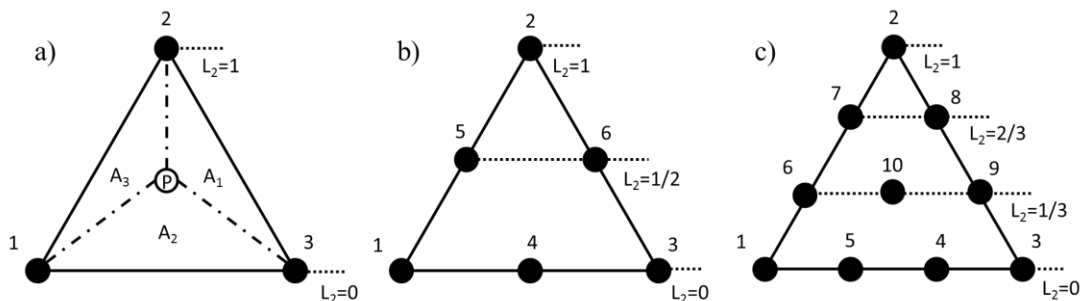


Fig. 3.8 a) An arbitrary point P is chosen inside the element. By connecting point P to the corners of the element, three subdomains are formed. A_1 , A_2 and A_3 are the areas of these triangular subdomains. L_2 is the ratio between A_2 and A (total area of element). L_2 is zero when point P is chosen on the line that connects corners 1 and 3. L_2 is one when point P is chosen at corner 2. b) L_2 has three values in this element. $L_2=0$, $L_2=0.5$, and $L_2=1$. c) L_2 has four values in this element. $L_2=0$, $L_2=0.5$, and $L_2=1$.

In Fig. 3.8, point P is an arbitrary point inside the element. By connecting point P to corners of the element, three triangles are formed. A_1 , A_2 and A_3 are the areas of these triangles. Based on the location of the arbitrary point P, one can define area coordinates as follows

$$L_1 = \frac{A_1}{A}, L_2 = \frac{A_2}{A}, L_3 = \frac{A_3}{A} \quad 3-56$$

If point P coincides with point 2, $A_2=A$ and $L_2=1$ while $L_1=L_3=0$. To find interpolation functions (N_i) for each node for 3-node and 6-node elements shown in Fig. 3.8a-b, one can write

$$\phi(x, y) = a_0 + a_1x + a_2y = L_1\phi_1 + L_2\phi_2 + L_3\phi_3 = N_1\phi_1 + N_2\phi_2 + N_3\phi_3 \quad 3-57$$

$$\begin{aligned}\phi(x,y) &= b_0 + b_1x + b_2y + b_3x^2 + b_4xy + b_5y^2 = L_1(2L_1 - 1)\phi_1 + L_2(2L_2 - 1)\phi_2 + \\ &L_3(2L_3 - 1)\phi_3 + 4L_1L_3 + 4L_1L_2 + 4L_2L_3 = N_1\phi_1 + N_2\phi_2 + N_3\phi_3 + N_4\phi_4 + N_5\phi_5 + N_6\phi_6\end{aligned}$$

3-58

where $\phi(x,y)$ is a scalar function, a_j are unknown constants where $j=1,2$ and 3 , b_i are unknown constants and ϕ_i are nodal values of $\phi(x,y)$ where $i=1,2, \dots 6$.

The main difference between FEM and FDM is that in FEM, interpolation functions are used to find the value of unknown variables everywhere inside an element where in FDM the unknown variables are only calculated at the grid points. So to increase the accuracy of the problem in FEM, one can either increase the order of interpolation functions or increase the number of elements where in FDM, the only method to increase the accuracy of the solution is by increasing the number of elements.

I will now introduce governing equations of elasticity in FEM for general three-dimensional elements. First, strain tensor $\boldsymbol{\varepsilon}$ is related to displacement vector (u,v,w) as follows

$$\{\boldsymbol{\varepsilon}\} = \begin{Bmatrix} \varepsilon_x \\ \varepsilon_y \\ \varepsilon_z \\ 2\varepsilon_{xy} \\ 2\varepsilon_{xz} \\ 2\varepsilon_{yz} \end{Bmatrix} = \begin{Bmatrix} \frac{\partial u}{\partial x} \\ \frac{\partial v}{\partial y} \\ \frac{\partial w}{\partial z} \\ \frac{\partial u}{\partial y} + \frac{\partial v}{\partial x} \\ \frac{\partial u}{\partial z} + \frac{\partial w}{\partial x} \\ \frac{\partial v}{\partial z} + \frac{\partial w}{\partial y} \end{Bmatrix} = \begin{bmatrix} \frac{\partial}{\partial x} & 0 & 0 \\ 0 & \frac{\partial}{\partial y} & 0 \\ 0 & 0 & \frac{\partial}{\partial z} \\ \frac{\partial}{\partial y} & \frac{\partial}{\partial x} & 0 \\ \frac{\partial}{\partial z} & 0 & \frac{\partial}{\partial x} \\ 0 & \frac{\partial}{\partial z} & \frac{\partial}{\partial y} \end{bmatrix} \begin{Bmatrix} u \\ v \\ w \end{Bmatrix} = [L] \begin{Bmatrix} u \\ v \\ w \end{Bmatrix}$$

3-59

where u,v,w are displacements in x , y , and z directions. Stress and strain are related to each other using constitutive equations. For homogenous, isotropic, linear elastic material this equation can be written as

$$\{\sigma\} = \begin{Bmatrix} \sigma_x \\ \sigma_y \\ \sigma_z \\ \sigma_{xy} \\ \sigma_{xz} \\ \sigma_{yz} \end{Bmatrix} = \frac{E}{(1+\nu)(1-2\nu)} \begin{bmatrix} 1-\nu & \nu & \nu & 0 & 0 & 0 \\ \nu & 1-\nu & \nu & 0 & 0 & 0 \\ \nu & \nu & 1-\nu & 0 & 0 & 0 \\ 0 & 0 & 0 & \frac{1-2\nu}{2} & 0 & 0 \\ 0 & 0 & 0 & 0 & \frac{1-2\nu}{2} & 0 \\ 0 & 0 & 0 & 0 & 0 & \frac{1-2\nu}{2} \end{bmatrix} \{\varepsilon\} = [D]\{\varepsilon\}. \quad 3-60$$

Following the general method explained at the beginning of this section for two dimensional elements, displacements for a three dimensional element can be written as

$$u(x, y, z) = N_i(x, y, z)u_i \quad 3-61$$

$$v(x, y, z) = N_i(x, y, z)v_i \quad 3-62$$

$$w(x, y, z) = N_i(x, y, z)w_i \quad 3-63$$

here u_i , v_i and w_i are nodal displacements, $N_i(x,y,z)$ is the interpolation function associated with the number of nodes and $i = 1,2,\dots, M$ indicates the node number. Nodal displacements are represented by

$$\{\delta\} = [u_1 \ u_2 \ \dots \ u_M \ v_1 \ v_2 \ \dots \ v_M \ w_1 \ w_2 \ \dots \ w_M]^T. \quad 3-64$$

Displacement field in the elements are related to nodal values of displacement

$$\begin{Bmatrix} u \\ v \\ w \end{Bmatrix} = \begin{bmatrix} [N] & [0] & [0] \\ [0] & [N] & [0] \\ [0] & [0] & [N] \end{bmatrix} \{\delta\} = [N_3]\{\delta\} \quad 3-65$$

where $[N]$ represents the interpolation function

$$[N] = [N_1 \ N_2 \ N_3 \ \dots \ N_M]^T. \quad 3-66$$

Total potential energy of an element is

$$\Pi = U - W = \frac{1}{2} \iiint_V \{\varepsilon\}^T \{\sigma\} dV - \{\delta\}^T \{f\} = \frac{1}{2} \iiint_V \{\varepsilon\}^T [D] \{\varepsilon\} dV - \{\delta\}^T \{f\} \quad 3-67$$

where f is the vector of nodal forces

$$\{f\} = [f_{1x} \ f_{2x} \ \dots \ f_{Mx} \ f_{1y} \ f_{2y} \ \dots \ f_{My} \ f_{1z} \ f_{2z} \ \dots \ f_{Mz}]^T. \quad 3-68$$

By substituting Eqs. (3.59) and (3.65) in Eq. (3.67), the total potential energy is

$$\Pi = U - W = \frac{1}{2} \{\delta\}^T \iiint_V [B]^T [D] [B] dV \{\delta\} - \{\delta\}^T \{f\} \quad 3-69$$

where $[B]$ is defined as

$$[B] = [L][N_3]. \quad 3-70$$

Using Castigliano's first theorem as follows,

$$\frac{\partial \Pi}{\partial \delta_i} = 0. \quad 3-71$$

One can find the nodal equilibrium equation for three dimensional elasticity governing equations

$$\iiint_V [B]^T [D] [B] dV \{\delta\} = \{f\}. \quad 3-72$$

By comparing Eq. (3.72) with Eq. (3.55), one can find stiffness matrix as

$$[K] = \iiint_V [B]^T [D] [B] dV. \quad 3-73$$

These equations will be modified to include plasticity in chapters 4 and 5 of this thesis. This is because these modifications depend on the yield criteria, flow rule and hardening rule that are specific to a given problem.

In this study, I use FEM to solve the phase field governing equations. Rectangular elements with quadratic interpolation functions are chosen for both elastoplastic and evolution equations. For this study, I have used commercial software package called COMSOL Multiphysics.

3.3 Reference

- [1] J. S. Rowlinson, *J Stat Phys* **20**, 197 (1979).
- [2] J. W. Cahn and J. E. Hilliard, *J. Chem. Phys.* **28**, 258 (1958).
- [3] A. Karma and W. J. Rappel, *Phys Rev E* **53**, 3017 (1996).
- [4] C. Beckermann, H. J. Diepers, I. Steinbach, A. Karma, and X. Tong, *J Comput Phys* **154**, 468 (1999).
- [5] A. Karma, *Phys. Rev. Lett.* **87**, 115701 (2001).
- [6] A. Artemev, Y. Jin, and A. G. Khachaturyan, *Acta Mater.* **49**, 1165 (2001).
- [7] A. Artemev, Y. Wang, and A. G. Khachaturyan, *Acta Mater.* **48**, 2503 (2000).
- [8] T. Miyazaki, T. Koyama, and T. Kozakai, *Mat Sci Eng a-Struct* **312**, 38 (2001).
- [9] J. J. Eggleston, PhD Thesis, NORTHWESTERN UNIVERSITY, 2001.
- [10] S. M. Wise, J. S. Lowengrub, J. S. Kim, K. Thornton, P. W. Voorhees, and W. C. Johnson, *Appl. Phys. Lett.* **87**, 133102 (2005).
- [11] A. Karma, D. A. Kessler, and H. Levine, *Phys. Rev. Lett.* **87**, 045501 (2001).
- [12] Y. U. Wang, Y. M. M. Jin, and A. G. Khachaturyan, *J. Appl. Phys.* **91**, 6435 (2002).
- [13] M. J. Borden, C. V. Verhoosel, M. A. Scott, T. J. R. Hughes, and C. M. Landis, *Comput Method Appl M* **217**, 77 (2012).
- [14] M. Koslowski, A. M. Cuitino, and M. Ortiz, *J Mech Phys Solids* **50**, 2597 (2002).
- [15] Y. U. Wang, Y. M. M. Jin, and A. G. Khachaturyan, *Acta Mater.* **51**, 4209 (2003).
- [16] P. Y. Chan, G. Tsekenis, J. Dantzig, K. A. Dahmen, and N. Goldenfeld, *Phys. Rev. Lett.* **105**, 015502 (2010).
- [17] C. M. Elliott and B. Stinner, *Siam J Appl Math* **70**, 2904 (2010).
- [18] J. S. Lowengrub, A. Ratz, and A. Voigt, *Phys Rev E* **79**, 031926 (2009).
- [19] N. Moelans, B. Blanpain, and P. Wollants, *Computer Coupling of Phase Diagrams and Thermochemistry* **32**, 268 (2008).

- [20] D. Fan, S. P. Chen, and L. Q. Chen, *J. Mater. Res.* **14**, 1113 (1999).
- [21] D. N. Fan and L. Q. Chen, *Acta Mater.* **45**, 3297 (1997).
- [22] D. Fan, L. Q. Chen, and S. P. P. Chen, *J. Am. Ceram. Soc.* **81**, 526 (1998).
- [23] L. Q. Chen, *Annu Rev Mater Res* **32**, 113 (2002).
- [24] J.-C. Tolédano and P. Tolédano, (World Scientific Publishing Co. Pte. Ltd, 1987).
- [25] S. M. Allen and J. W. Cahn, *Acta Metall.* **27**, 1085 (1979).
- [26] J. W. CAHN, *Acta Metall.* **9**, 795 (1961).
- [27] A. Gaubert, Y. Le Bouar, and A. Finel, *Philosophical Magazine* **90**, 375 (2010).

Chapter 4 **Effects of confinements on morphology of $\text{In}_x\text{Ga}_{1-x}\text{As}$ thin film grown on sub-micron patterned GaAs substrate: elastoplastic phase field model**

Published in Journal of Applied Physics, Volume 116: 114313 (2014)

4.1 **Abstract**

An elastoplastic phase field model is developed to investigate the role of lateral confinement on morphology of thin films grown heteroepitaxially on patterned substrates. Parameters of the model are chosen to represent $\text{In}_x\text{Ga}_{1-x}\text{As}$ thin films growing on GaAs patterned with SiO_2 . I determined the effect of misfit strain on morphology of thin films grown in $0.5\mu\text{m}$ patterns with non-uniform deposition flux. Growth of islands inside patterns can be controlled by non-uniformity of deposition flux, misfit strain between film and the substrate, and also strain energy relaxation due to plastic deformation. Our results show that the evolution of island morphology depends non-monotonically on indium content and associated misfit strain due to coupling between the plastic relaxation and the confinements effects. Low indium concentration (0-40%) causes formation of instabilities with relatively long wavelengths across the width of the pattern. Low surface diffusion (due to low indium concentration) and fewer islands across the pattern (due to small misfit strain) lead to formation and growth of islands near the walls driven by overflow flux. Further increase in indium concentration (40-75%) increases the lattice mismatch and surface diffusivity of the film, and also activates plastic deformation mechanism, which leads to coalescence of islands usually away from the edges. By further increasing the indium concentration (up to 100%), plastic deformation relaxes most of the strain energy density of the film, which prevents formation of instabilities in the film. Hence, in this case islands are only formed near the walls.

4.2 Introduction

Growth of semiconductors on patterned substrates provides an effective approach to fabricate ordered surface structures such as quantum-dots [1], nano-rods [2] and nano-rings [3]. These nano-structures are used for a number of different applications, including solar cells, sensors, electronic and photonic devices [4]. Advancements in patterning techniques, e.g., self-assembly processes [5], lithographic methods [6-8], scanning probe techniques [9] and block copolymer methods [10], make it now possible to prepare large-scale arrays with a precisely tailored shape, size, and crystallographic orientation [4].

Of particular interest to this study is the use of patterned substrates to grow III-V semiconductor thin films. Multiple experimental studies have been reported in this area. For instance, Jha *et al.* [11] used block copolymer lithography (BCL) to pattern GaAs and to grow GaSb. Brammertz *et al.* [12] selectively grew GaAs films on Ge using SiO₂ mask layers. Martin-Sanchez *et al.* [13] combined atomic force microscopy and local oxidation nanolithography to grow InAs quantum dots on GaAs substrate. Elarde *et al.* [14] studied preferential sites for quantum dots growth of InGaAs/GaAs system using the selective area epitaxy method. Hoshii *et al.* [15] demonstrated that micro selective area growth is an effective way to increase the quality of crystal InGaAs on Si substrates using SiO₂ patterns. They showed that one could control the nucleation process and potentially reduce the number of InGaAs nuclei on Si substrate by using very small area regions of Si. Ganesan *et al.* [16] used SiO₂ patterns made by lateral epitaxial growth to study growth of InAs film on GaAs substrates using metalorganic chemical vapor deposition method. One of the key observations from these studies is that patterns can be utilized to control nucleation and growth of islands, as well as their crystallographic orientations. For example, in the study of Ganesan *et al.* [16], who used strip-shaped patterns (trenches), it was found that trenches of different sizes can provide an effective way to control the morphology of the islands. Specifically, for patterns that are approximately 0.6 μm wide, scattered islands were

able to find and coalesce with each other [16], which can lead to reduction in the number of nuclei and an improvement in crystal quality [15]. The growth of islands near walls in patterned morphologies has been attributed to the effects of overflow growth, which means that an additional material is deposited near the walls because it does not stick to the patterned mask and flows down along the pattern walls into the trenches [17]. However, it is not clear how this contribution from overflow flux interacts with the effects of surface diffusion of the film, lattice mismatch between the film and the substrate, and plastic relaxation to produce the final morphology of the film.

Contributions to energy during heteroepitaxial growth of thin films on patterned substrates come from strain energy due to the lattice mismatch between the film and the substrate, surface energy of the film, and interfacial energy between the film and the walls of the patterns. Morphology evolution (formation of islands) and plastic deformation due to formation of dislocations are two mechanisms that can relax the energy during such growth. Two main mechanisms have been proposed to lead to formation of islands: surface instability due to strain energy [18] and dewetting [18,19]. These mechanisms may be active simultaneously during heteroepitaxial growth [20]. Surface instability, which is caused by non-hydrostatic stress, is referred to as the Asaro-Tiller-Grinfeld-Srolovitz (ATGS) instability [21-23]. In this case, surface morphology is determined by the competition between strain energy due to lattice mismatch and surface energy, which competition may lead to formation of islands. These islands can subsequently coalesce and grow. On the other hand, the dewetting mechanism is driven by competition among surface energies of the film and the substrate and their interfacial energy. In this paper, I assume there is always a wetting layer between the film and the substrate and therefore our focus will be on the effects of the competition between strain and surface energy of the film. This assumption is consistent with the Stranski-Krastanov growth mode, which has been observed for InGaAs experimentally [24]. The wetting layer in these experiments was reported to

vary from a couple of monolayers to several nanometers. In my model I choose an intermediate value of 3 nm. An alternative strain relief method is formation of misfit dislocations, which usually happens when the film thickness is above a critical limit. Dislocations are mostly formed at film-substrate interface and can cause deterioration of electronic properties of the film. Several theoretical and experimental studies [25-29] have suggested that both morphological evolutions and plastic deformation take place in films above the critical thickness.

Simulations provide a powerful approach that is complementary to experiments and that allows a systematic investigation of the various factors that impact morphological evolution of heteroepitaxially grown films. A range of computational tools has been previously employed to address different aspects of such growth. These tools include *ab-initio* methods [30], molecular dynamics based on classical force fields [31], kinetic Monte-Carlo [32] and continuum models, where the latter ones can be divided into sharp interface [33,34] and diffuse interface models [35,36]. In conventional continuum modeling approaches to microstructural evolution, the interfaces between different phases (e.g., the film/vapor and film/substrate interfaces) are considered to be sharp and consequently it is necessary to define a multi-domain structure to model these systems. For each domain one set of differential equations is being solved while the constitutive equations and flux boundary conditions have to be satisfied at the interfaces. Hence one needs to track explicitly each moving interface, which can be numerically challenging for morphologically complex interfaces and for multiphase systems (which contain many interfaces) [36,37].

Each of the aforementioned modeling approaches has its own advantages. Of particular interest to the current study are continuum models since they enable simulations of growth on the experimental time and length scales [38-40]. One example of using continuum approaches to study growth is the study of Tu and Tersoff [40], who modeled the effect of intermixing of the deposited material and the substrate on the planar growth of thin films. The critical thickness

predicted by their model has a similar dependence on misfit strain as seen experimentally. The same authors have also used sharp interface models to investigate island formation and evolution of heteroepitaxial systems [39]. They observed morphological changes and alloy intermixing as active methods to reduce the free energy of the system. It was also found that there is a strong coupling between morphological and compositional evolutions due to surface diffusivity, which is the main mass diffusion mechanism implemented in the model in Refs. [39,40].

Among diffuse interface approaches, phase field modeling has emerged in recent years as an effective numerical tool for studies of film growth. In a phase field model one can capture both the thermodynamic effects (e.g., the elastic strain energy and the thermodynamic stability of a given phase) and the kinetic effects (e.g., the deposition flux and diffusion) on growth [36,41]. Phase field models have already been successfully used to study problems related to the ATGS instability [33,42-46]. For instance, Eggleston *et al.* [35] developed a phase field model to investigate the growth of thin films on non-patterned and patterned substrates. The patterned systems consisted of long and narrow mesas deposited on the substrate. Simulations showed formation of wavelike islands due to surface instability of films during the growth. They also showed that the presence of mesas causes formation of highly ordered arrays of nanocrystalline islands. Interestingly, including anisotropy of the surface energy of the film led to a faster occurrence of instability on the film surface. This phenomenon reduced the distance over which instability wave travels, causing a reduction in the island ordering. In a different study Wise *et al.* [47] investigated the effects of an inclusion buried in the substrate on the morphology of the film during growth. The authors reported the same waviness on the surface as observed by Eggleston *et al.* [35]. It was found that the embedded particle localized the growing islands, leading to the idea that strain patterning could be used to increase the ordering of islands. In addition, Wise *et al.* [38] considered the effects of strain energy due to compositional strain and surface energy on the morphology of binary alloys. Simulations showed that there is a competition between the

surface energy and compositional strain energy, which leads to alignment of segregated phases with respect to the film surface. This alignment can be either parallel or perpendicular to the surface, depending on the simulation conditions. For large enough compositional strain, phase separation is controlled by strain energy and alignment of phases perpendicular to the free surface is more favorable. For smaller compositional strain, surface energy dominates the morphological evolution, leading to a parallel alignment of the separated phases with respect to the surface. The ATGS surface instability has been also studied by Boyne *et al.* [20], who used phase field to simulate heteroepitaxial morphological evolution of Gadolinia-doped ceria films deposited on Ytria-stabilized zirconia. The authors considered the effects of confinement (patches) present on the substrate. They assumed a constant misfit strain due to lattice mismatch throughout the film. Similarly to the previously discussed results, Boyne *et al.* [20] reported development of wavelike ordering in the stress driven instability on the surface of the thin film surface. Instabilities were initiated next to the surface patches and it was found that when a misfit stress exists in the substrate and in the patches, instability starts more quickly than in the case of stress-free patches. However, Boyne *et al.* [20] did not study the kinetic effect associated with the deposition flux and how this deposition flux couples to diffusion. Also the effect of relaxation associated with plastic deformation was not investigated in their model.

In crystalline materials, plastic deformation is mainly due to formation of dislocations. Hence, several studies have been reported that couple dislocation plasticity to the phase field formation. Dislocations can be introduced into the model either explicitly or through constitutive elasto-plastic equations. Explicit models treat dislocations as continuous fields on each slip system and couple these fields to phase field variables. The most important advantage of this method is that it inherently includes interactions between dislocations. An example of this approach was reported in 2001 by Wang *et al.* [48,49], who studied multi-dislocation system in elastically anisotropic crystals. Later on, Hataaja *et al.* [50] introduced phase field formulation

coupled with dislocations as a model for non-equilibrium multiphase systems to simulate the dynamics of lattice-mismatched heteroepitaxial films. The authors investigated how dislocations can compete with surface instability to relieve strain during the film growth. Hataaja *et al.* [51] later developed their model to include the effects of nucleation, interactions and dynamics of dislocation. Wang *et al.* [52] added an extension to the phase field microelasticity to study the dislocation dynamics near a free surface in heteroepitaxial thin films. However, there are a couple of drawbacks associated with the approach of studying dislocations explicitly. Firstly, one needs sub nanometer grid size to model the dislocation cores, which limits the total size of the simulation domain. Consequently, while explicit modeling of dislocations has been implemented before studying growth of heteroepitaxial thin films, this has been done only for non-patterned surfaces. Secondly, different mechanisms for dislocations (other than glide) have not been accounted for yet within phase field models, and this is still an active area of research [53]. Another approach is to model dislocations implicitly by coupling elasto-plastic constitutive equations to the phase field model through plastic strain field. This approach does not require very fine grid points and therefore is amenable to simulating larger simulation domains with nanopatterns. Flow rule and hardening law in the form of ordinary differential equations need to be solved in addition to equilibrium, constitutive and compatibility equations, and one needs to add a yield condition to the model. This approach was used by Guo *et al.* [54] who coupled plasticity to a phase field model to study the stress distribution around defects, such as cracks and holes. Gaubert *et al.* [55] developed an elasto-visco-plastic model to study microstructural evolution during a creep loading in superalloys. Cottura *et al.* [53] developed a size dependent viscoplastic phase field model to study the rafting of the microstructures. However, this kind of approach has not previously been applied to study heteroepitaxial growth on patterned substrates. Since I am not interested in lower length scale information about dislocation structures and also because of numerical efficiency of this type of method, I choose it for this investigation.

Specifically, here I developed a phase field model coupled with elastoplasticity governing equations to determine how surface patterning, misfit strain, and plastic relaxation affect morphology of thin films. In order to be consistent with typical experimental conditions, I include in the model a biased deposition, with statistical non-uniformity of the deposition flux expected for patterned substrates [17], and high interfacial energy between the film and the walls of the patterns (non-wetting conditions). One of the key questions that I answer with these simulations is under what conditions islands can nucleate and grown near the edges of the patterns. Such a growth pattern is attractive since it leads to a more uniform island size distribution and a more uniform crystallographic orientation of the islands [16]. Another important question I answer is under what circumstances small islands coalesce to form a single island across the pattern. Again, such single island structures are preferred as they can decrease the density of defects [15,56]. The parameters in our study are chosen so that the film has the effective properties of $\text{In}_x\text{Ga}_{1-x}\text{As}$, the substrate the properties of GaAs, and the pattern walls the properties of SiO_2 .

4.3 Elastoplastic phase field model

In this section I report governing equations, boundary conditions, and the simulation parameters used to model heteroepitaxial growth of thin films under the conditions of lateral confinements due to surface patterning. I will investigate the effects of misfit strain and plastic deformations on morphology of the thin film grown in $0.5\ \mu\text{m}$ -wide pattern under effects of non-uniform overflow flux and at a constant temperature. Schematic cross-sectional view of the patterned substrate with overflow deposition flux is shown in Fig. 4.1a. As shown in Fig. 4.1b, the model consists of the substrate (orange), walls of the confining pattern (dark blue), the gas phase (light blue) and the film (red). I treat each of these sections as a one-component system (one phase), with effective properties of GaAs (for the substrate), SiO_2 (for the walls) and $\text{In}_x\text{Ga}_{1-x}\text{As}$ (for the film). The concentration of the growing film varies between $c = 0$ (representing the vapor phase and shown in light blue) to $c = 1$ (representing the solid phase and shown in red).

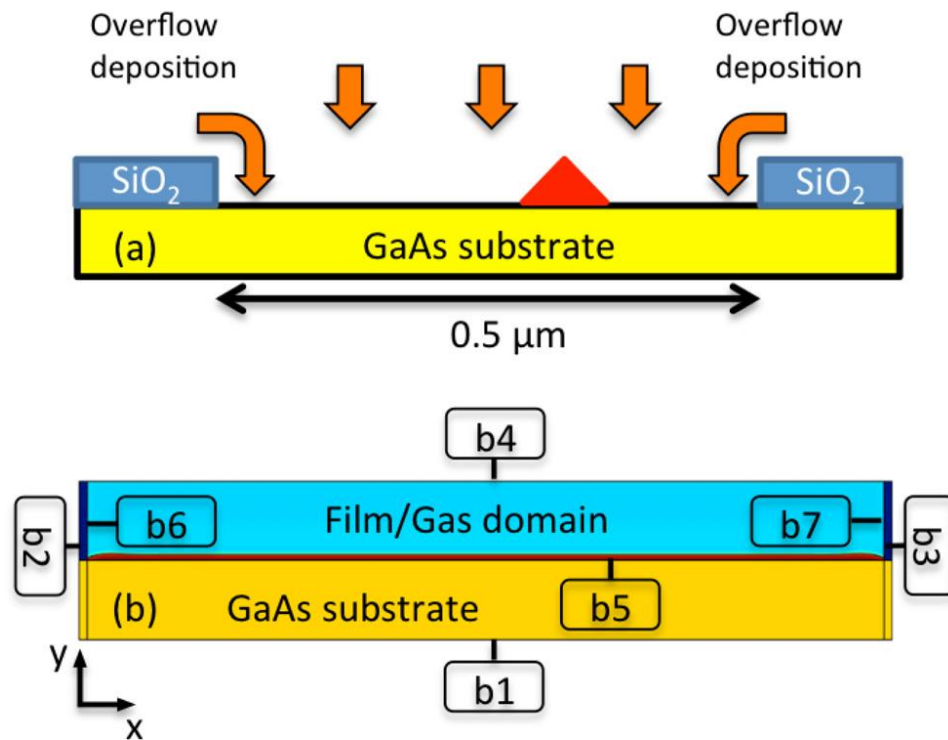


Fig. 4.1 a) Schematic cross-sectional view of the patterned substrate showing deposition flux non-uniformity. The distance between two walls is $0.5 \mu\text{m}$. Width of SiO_2 pattern is also $0.5 \mu\text{m}$ but is not plotted to scale b) Boundaries in the simulation domain: b1 (the lower boundary of the substrate), b2 and b3 (outer boundaries of the wall and the substrate), b4 (outer/top boundary of the gas phase region), b5 (substrate/film interface), b6 and b7 (interface between wall and film/gas). The coordinate system originates at the interface between film and the substrate.

In our simulations, I treat the film as one phase and do not allow for phase separation. This assumption is consistent with experimental observation of no phase separation in InGaAs grown on GaAs [16]. The wall and the substrate are considered to be in the solid phase with concentrations equal to 1. Here, I assume that there is always a wetting layer (called a boundary-layer [35]) on the substrate. Therefore, the substrate is never exposed to the gas phase and the interface between the film and the substrate does not evolve with time. In addition, I assume that

the main mass transport mechanism in the film is via surface diffusion, which occurs around the film-vapor interface. This is a common assumption for heteroepitaxial growth of thin films [35]. Bulk diffusion is ignored in the film, the substrate, and the walls and there is no mass transport between these three regions.

In many experiments, patterns have the form of long strips [15,16]. In our two-dimensional simulations I represent such experiments by assuming plain strain conditions. Specifically, the pattern wall has an infinite length along the z direction (into the plane of Fig. 4.1). Deposition flux has a random perturbation of $\pm 5\%$ in the flux magnitude introduced at each grid point across the width of pattern under both uniform and biased deposition conditions to represent the noise in deposition process [35]. Random numbers are drawn from a uniform distribution. This randomness also provides the perturbation needed to initiate surface instability [35].

I model the film growth using the phase field method combined with elastoplasticity equations. Following Cahn and Hilliard [57] and Allen and Cahn [58] equations, the total free energy F of the system can be written in the following functional form

$$F = \int_{\Omega} \left(f(c) + W(c) + \frac{\varepsilon^2}{2} |\nabla c|^2 \right) d\Omega + \oint_{B_1} f_s(c) dl \quad 4-1$$

The above total free energy of the system consists of two integrals, and each of them is discussed below in detail. In the first integral on the right hand side (rhs) of Eq. (4-1), Ω represents the cross-sectional area of the entire system, c is the concentration (density). ε^2 is the gradient energy coefficient. Following the formulation developed by Egglestone *et al.* [35], anisotropic interfacial energy between film and gas is defined as

$$\varepsilon(\theta) = \varepsilon_0(1 + \varepsilon_4 \cos(4\theta)) \quad 4-2$$

where ε_0 is the gradient energy constant, θ is the angle between the normal to the contour of constant concentration and the x axis and ε_4 is a constant between 0 to 1, which determines the

degree of anisotropy. The variation of ε_4 with distance from the substrate has been adopted from Egglestone *et al.* [35].

In the first integral on the rhs of Eq. (4-1), f is the free energy density and it is a function of concentration. I use a double-well potential, f_1 , for the free energy density function in the film. In the substrate and the walls, I use a single-well potential, f_2 , to restrict their evolution [20]. Specifically,

$$f_1(c) = \frac{1}{4}w_0c^2(1-c)^2 \quad 4-3$$

$$f_2(c) = \frac{1}{4}w_0(1-c)^2 \quad 4-4$$

where w_0 represents the barrier height of the single and double-well functions representing the local free energy density. Symbol W in Eq. (4-1) has contributions from elastic and plastic energy densities, which are defined as

$$W(c) = W^{el}(c) + W^{pl}(c) \quad 4-5$$

where $W(c)$ is the total work, $W^{pl}(c)$ is the plastic work

$$W^{pl}(c) = \int_0^{e^{pl}} \sigma_{ij} de_{ij}^{pl} \quad 4-6$$

e_{ij}^{pl} is plastic strain tensor and σ_{ij} is the Cauchy stress tensor. $W^{el}(c)$ is the elastic work given as

$$W^{el}(c) = \frac{1}{2}\sigma_{ij} e_{ij}^{el} \quad 4-7$$

where e_{ij}^{el} is an elastic strain tensor, which can be given as

$$e_{ij}^{el} = e_{ij}^{tot} - e_{ij}^* - e_{ij}^{pl} \quad 4-8$$

where e_{ij}^{tot} is the total strain and e_{ij}^* is the eigenstrain associated with the difference between lattice parameters of the film and the substrate. Assuming a linear strain displacement relationship, the total strain can be written as

$$e_{ij}^{tot} = \frac{1}{2}(u_{i,j} + u_{j,i}) \quad 4-9$$

where $u_{i,j}$ is the derivative in the j direction of the displacement in i direction. Total strain is calculated by solving the mechanical equilibrium (Cauchy-Navier) equation

$$\frac{\partial \sigma_{ij}}{\partial x_j} = 0 \quad 4-10$$

Following Egglestone *et al.*[35] eigenstrain in our model is defined as

$$e_{ij}^* = \frac{1}{2} \hat{\epsilon}_f (1 + f_{BL}(y)) \delta_{ij} \quad 4-11$$

where δ_{ij} is kreneckar delta and f_{BL} is the boundary layer function of the same form as in Ref. [35] $\hat{\epsilon}_f$ is the lattice mismatch which is given by

$$\hat{\epsilon}_f = \frac{a_{film} - a_{substrate}}{a_{substrate}} \quad 4-12$$

To find the plastic strain tensor I need to define a yield function, a flow rule and a hardening rule. Here, I use $J2$ plasticity (Von-Mises criteria) with the yield function

$$F(\sigma_{ij}, \sigma_Y) = \sigma_{mises} - \sigma_Y \leq 0 \quad 4-13$$

where F is the yield function, σ_Y is the current yield stress, and σ_{mises} is the Von-Misses stress.

For isotropic hardening, flow rule is given by

$$\dot{e}_{ij}^{pl} = \lambda \frac{\partial F(\sigma_{ij}, \sigma_Y)}{\partial \sigma_{ij}} \quad 4-14$$

where $\dot{\epsilon}_{ij}^{pl}$ is plastic strain rate and λ is plastic multiplier, which is a positive number. For the film and the substrate materials I assume a linear work hardening, which can be written mathematically as

$$\sigma_Y = \sigma_{Y0} + \sigma_h \quad 4-15$$

where σ_{Y0} is the initial yield stress and σ_h is the work hardening function

$$\sigma_h = E_t \cdot e^{pl} \quad 4-16$$

where E_t is tangential Young's modulus. This value was measured for InGaAs layers to be approximately 20% of the Young's modulus [59] of InGaAs. Since E_t was not measured for the entire range of compositions, I assume this value to be a reasonable approximation for all compositions I study.

The second integral on the rhs of Eq. (4-1) corresponds to surface and interfacial energies on B_1 , where B_1 represents the interface between the film and the walls (b6 and b7 in Fig. 4.1b). f_s stands for the difference between interfacial energy densities for the film/wall and vapor/wall interfaces. There is a convenient way to include the term f_s into the model, which was first introduced by Cahn [60] and later used by Wise *et al.* [38,61]. Specifically,

$$f_s(c) = s_1 c \quad 4-17$$

where s_1 is a positive constant. Eq. (4-17) assumes that f_s is linearly dependent on concentration of the nearby phase. Higher values of s_1 correspond to more non-wetting conditions at the interface. The approximation given in Eq. (4-17) has been shown to be in agreement with the nearest-neighbor bond counting approximation [38,61], in which the surface/interfacial energy is calculated based on energy contributions from broken bonds at that surface/interface. To my knowledge, the interfacial energy between $\text{In}_x\text{Ga}_{1-x}\text{As}$ film and the SiO_2 wall has not been measured experimentally. However, experimental observations [16] imply non-wetting conditions

at such interface. Therefore in our simulations I will use $s_1 = 0.03$, which corresponds to an interfacial energy that is high enough to produce non-wetting conditions in our simulations. The interfacial energy between $\text{In}_x\text{Ga}_{1-x}\text{As}$ film and the GaAs substrate is assumed to be negligible. The interfacial energy between $\text{In}_x\text{Ga}_{1-x}\text{As}$ film and the vapor will be defined later.

The different boundaries present in these simulations are defined in Fig. 4.1b. I use the displacement and/or traction vectors to define boundary conditions. I assume that the displacements vanish at the lower boundary of the substrate (b1). The outer boundaries, b2 and b3, are also kept fixed (zero displacements) while the top boundary of the gas phase region (b4) is assumed to be traction free. Since the growing film is very thin, I assume that the traction vector at b5 is also zero. The displacement and the traction vectors are continuous across the boundary b5. The traction, which the elastic walls exert on the film, is proportional to the displacement along the x direction of the boundaries b6 and b7. In addition, the traction vector is continuous across the wall/film boundaries, b6 and b7. The x component of displacement vector u_x is continuous across the boundaries b6 and b7, while the y component u_y of displacement field is not in order to enable the film to climb up the wall in case it is favorable.

In this model concentration (c) is a conserved field variable. Concentration evolves according to the mass conservation equation

$$\frac{\partial c}{\partial t} = -\nabla \cdot J + J_a n_y \quad 4-18$$

where J is the density flux, which can be related to the gradient of variational derivative of the free energy density functional as

$$J = -M(c)\nabla \frac{\delta F}{\delta c} = -M(c)\nabla \left(\frac{\partial f}{\partial c} + \frac{\partial W^{el}}{\partial c} + \frac{\partial W^{pl}}{\partial c} - \nabla \cdot (\varepsilon^2 \nabla c) + \frac{\partial}{\partial x} \left(\varepsilon \frac{d\varepsilon}{d\theta} \frac{\partial c}{\partial y} \right) - \frac{\partial}{\partial y} \left(\varepsilon \frac{d\varepsilon}{d\theta} \frac{\partial c}{\partial x} \right) \right) \quad 4-19$$

where $\frac{\delta}{\delta c}$ is variational derivative. The plasticity driving force on concentration field is $\frac{\partial W^{pl}}{\partial c}$.

Since the majority of the plastic work in crystalline systems is released as heat, I assume that the

effect of plastic work as driving force for evolution of the concentration field is negligible. $M(c)$ is the mobility, which depends on the concentration in the following way

$$M(c) = M_s c^2 (1 - c)^2 \quad 4-20$$

where M_s is the surface mobility. In Eq. (4-18), J_d is the deposition flux and n_y is the vertical component of the surface normal. J_d is defined as [35]

$$J_d = V_d A_0 R_0 c^2 (1 - c)^2 K(x) \quad 4-21$$

where V_d is the surface velocity (growth rate) due to deposition, R_0 is a random number between 0.95 to 1.05, and $A_0 = \frac{6}{\delta}$, where δ is the interfacial thickness. The function $K(x) = (126 - 125 \cdot H(x - 2) + 125 \cdot H(x - 498))$ describes the overflow flux, where $H(x)$ is the Heaviside function. The parameters of the $K(x)$ function correspond to the mesh of 500 elements, each element being 1 nm wide. The overflow flux is added to 2 mesh elements on each side of the pattern. The width of the masked substrate between two trenches is also 500 nm. I assume that the entire material deposited on the mask flows into the two adjacent trenches (half of the deposited material flows into each trench). The additional flux of 250 nm is added within the 2 nm distance near each wall. I evaluated that the additional flux effectively leads to an increase of the flux by 125 times as compared to the deposition flux inside the trench.

Combining Eqs. (4-18) and (4-19), one can derive the following Cahn-Hilliard equation [62]

$$\frac{\partial c}{\partial t} = \nabla \cdot \left[M(c) \nabla \left(\frac{\partial f}{\partial c} + \frac{\partial W^{el}}{\partial c} - \nabla \cdot (\varepsilon^2 \nabla c) + \frac{\partial}{\partial x} \left(\varepsilon \frac{d\varepsilon}{d\theta} \frac{\partial c}{\partial y} \right) - \frac{\partial}{\partial y} \left(\varepsilon \frac{d\varepsilon}{d\theta} \frac{\partial c}{\partial x} \right) \right) \right] + J_d n_y \quad 4-22$$

Note that in this work, the coupling between plasticity and microstructure evolution is only through the elastic driving force, which is an approach often taken in the literature [55].

As shown in Eq. (4-1) and Eq. (4-19), the phase field model is coupled to the elastic energy of the system. This coupling is implemented by solving Cauchy-Navier equations (Eq. (4.10)) in two dimensions simultaneously with the Cahn-Hilliard equation (Eq. (4.22)) to find the

displacement and concentration fields at each time step of the simulation. Since I have a 2-D model, all energies in the model are defined per unit of length along the z direction. I wrote the phase field code using the commercial software, COMSOL, which solves systems of partial differential equations using finite element method. The total dimensions of the model are 500×180 grid points, with more grid points along the x direction. I use a non-uniform mesh along the y direction with a more refined mesh size ($\sim 1 \text{ \AA}$) near the substrate and coarser mesh size ($\sim 1 \text{ nm}$) in the gas phase away from the substrate.

In the model I assume homogenous and cubic elastic constants for the film and the substrate while isotropic elastic constants has been used for the walls. The elastic constants, yield strength, surface energy, diffusion coefficient and growth conditions for different indium concentrations are listed in Table 4.1.

Table 4.1 Elastic constants, yield strength, surface energy, diffusion coefficient and growth conditions for different indium concentrations.

Input parameters	Substrate (GaAs)	Film ($\text{In}_x\text{Ga}_{1-x}\text{As}$)				
		0	0.1	0.25	0.5	0.75
Concentration x	0	0.1	0.25	0.5	0.75	1
C_{11} (GPa)	118.8 [63]	115.2	109.9	101.1	92.2	83.4 [63]
C_{12} (GPa)	53.4 [63]	52.6	51.4	49.4	42.5	45.4 [63]
C_{44} (GPa)	59.6 [63]	57.6	54.6	49.5	44.5	39.5 [63]
Yield strength σ_{Y0} (GPa)	5 [59]	5.5 [59]	5.5 [59]	4.5 [59]	3 [59]	2.5 [59]
Surface energy γ (J m^{-2})	0.714 [63]	0.712	0.710	0.706	0.703	0.699 [63]

Gradient energy coefficient ε_0^2 (nJ m ⁻¹)	-	2.137	2.131	2.119	2.108	2.097
Lattice mismatch (%)	0	0.71	1.79	3.58	5.37	7.17
Diffusion coefficient D_0 (cm ² s ⁻¹)	1×10^{-7} [64]	1.9×10^{-7}	3.25×10^{-7}	5.5×10^{-7}	7.75×10^{-7}	1×10^{-6} [65]

Elastic constants, surface energy and diffusion coefficients for pure GaAs and InAs are found from Refs. [63-65], as indicated in Table 4.1. I use a linear interpolation between compositions $x = 0$ and $x = 1$ to find the properties for $\text{In}_x\text{Ga}_{1-x}\text{As}$ for different indium concentrations. The yield stress of InGaAs, which is an input parameter to our model, is extracted from Korte *et al.* [59]. The interfacial energy γ and interfacial thickness δ are related to gradient energy coefficient ε_0^2 and the barrier height of the double-well function w_0 through $\gamma = \frac{\varepsilon_0}{6} \sqrt{\frac{w_0}{2}}$ and $\delta = \varepsilon_0 \sqrt{\frac{2}{w_0}}$ (see for instance Ref. [35]). The interfacial thickness is assumed to be about 5 Å and the grid size near the substrate is about 1 Å. From the expression for the interfacial thickness and interfacial energy, I calculate w_0 to be 1.75×10^9 J m⁻³. To describe anisotropic interfacial energy, I accepted the formulation developed by Egglestone *et al.* [35], where gradient energy coefficient ε_0^2 is calculated and shown in Table 4.1 for different indium concentrations. The anisotropic gradient energy coefficient is assumed to vary with thickness as derived in Egglestone *et al.* [35]. The surface mobility M_s depends on surface diffusion coefficient D_0 through $D_0 = M_s RT$, where T is temperature and R is gas constant. M_s is assumed to be 4.36×10^{-18} m⁵ J⁻¹ s⁻¹ for InAs and 3.54×10^{-20} m⁵ J⁻¹ s⁻¹ for GaAs, which corresponds to surface diffusivity of 1×10^{-6} cm² s⁻¹ and 1×10^{-7} cm² s⁻¹, respectively [63,65]. Growth temperature T is set to 650 °C. Growth rate is assumed to be 1 nm/s. The simulation parameters are normalized in the following way. I use l^* as the characteristic length (taken to be 1 nm), e^* as the characteristic energy density (taken to be 10^{10} J

m^{-3}) and t^* as the characteristic time (chosen to be 10^{-8} s). Using these dimensionless parameters, I define other dimensionless quantities, which are free energy density ($f^* = \frac{f}{e^*}$), elastic moduli ($C_{ij}^* = \frac{C_{ij}}{e^*}$), strain energy density ($W^* = \frac{W}{e^*}$), gradient energy coefficient ($\varepsilon^{*2} = \frac{\varepsilon^2}{l^{*2} \cdot e^*}$), mobility ($M^* = \frac{M_s t^* \cdot e^*}{l^{*2}}$) and deposition flux rate ($J_d^* = t^* \cdot J_d$). I can also write a dimensionless form of the Cahn-Hilliard equation

$$\frac{\partial c}{\partial \hat{t}} = \nabla \cdot \left[M^*(c) \nabla \left(\frac{\partial f^*}{\partial c} + \frac{\partial W^{el^*}}{\partial c} - \nabla \cdot (\varepsilon^{*2} \nabla c) + \frac{\partial}{\partial \hat{x}} \left(\varepsilon^* \frac{d\varepsilon^*}{d\theta} \frac{\partial c}{\partial \hat{y}} \right) - \frac{\partial}{\partial \hat{y}} \left(\varepsilon^* \frac{d\varepsilon^*}{d\theta} \frac{\partial c}{\partial \hat{x}} \right) \right) \right] + J_d^* n_y \quad 4-23$$

where the ∇ symbol here represents a gradient with respect to non-dimensional variables \hat{x} and \hat{y} . Simulations are performed for the total time of 5×10^7 , 1×10^8 and 5×10^8 simulation steps Δt , where $\Delta t = 10^{-8}$ s. I report time in seconds, but one can convert seconds to time steps by dividing the simulation time by Δt . The total time of the simulations was chosen so that the total energy variation between last two time steps is less than 1×10^{-6} percent of the total energy, indicating very small change in the morphology.

4.4 Results

I report results of phase field simulations of heteroepitaxial growth of thin films on patterned substrates coupled with elastoplastic governing equations, with parameters corresponding to the $\text{In}_x\text{Ga}_{1-x}\text{As}/\text{GaAs}$ systems with SiO_2 patterns. Our goal is to determine how patterns control the morphology of islands during growth. More specifically, I identify conditions leading to the island growth near the walls of the SiO_2 patterns and conditions under which a single island grows away from the walls. I investigate how the morphology of the growing film is affected by the lattice mismatch between the film and the substrate and also I study the role of plastic relaxation in the film on morphology. The model includes a biased deposition flux and high interfacial energy between the film and confining walls of the pattern, to emulate experimental conditions. Although plastic relaxation is allowed in this model for all In concentrations in the

$\text{In}_x\text{Ga}_{1-x}\text{As}/\text{GaAs}$ alloy, I found that it occurs only for In concentrations higher than 0.4. Therefore I break up the discussion of our results into the low- (< 0.4) and high- (> 0.4) In concentration regimes.

4.4.1 Low indium concentration $\text{In}_x\text{Ga}_{1-x}\text{As}/\text{GaAs}$ ($x < 0.4$)

Here I investigate the effect of misfit strain on the morphology of the islands across the pattern. It is of particular interest to know under what condition islands coalesce to make a single nucleus and when they form multiple nuclei. For instance, as discussed in the introduction, experimental observations have shown the existence of the overflow flux near the walls [17] and the question arises whether this overflow flux will always lead to formation of islands near the edges of the patterns or whether it competes with other equally strong effects on film morphology.

First I study growth of $\text{In}_{0.1}\text{Ga}_{0.9}\text{As}$ film on GaAs substrate with SiO_2 confining walls. This model includes the effect of the overflow flux, which means that effectively there is a higher local deposition of material near the walls. Under experimental conditions, deposition flux is actually uniform throughout the entire patterned sample. However, since the deposited material does not form strong bonds with the SiO_2 mask, it does not grow on top of the mask. This behavior was demonstrated experimentally for example during InAs growth on patterned GaAs substrate, where the deposited material was growing in the trenches only [16,17]. As a result, the material initially deposited on SiO_2 flows down the walls toward the substrate and the film growing on top of it. This idea is schematically shown in Fig. 4.2a. To estimate the flux near the walls, I assume the trenches are equally spaced and separated by $0.5 \mu\text{m}$ -wide SiO_2 mask. Under these conditions, the overflow material deposited near each wall is equal to half of the material deposited on top of the SiO_2 mask. I assume that this additional flux is spread over a distance of two finite element mesh grids in our simulations, which corresponds to a physical distance of 2 nm. The results of phase field simulations at different times during for growth with $x = 0.1$ In concentration are

shown in Fig. 4.2. This low indium concentration (with a corresponding lattice mismatch of 0.71 %) does not cause any instability in the initial flat film, except for near the edges due to unfavorable interfacial energy between the film and the walls as shown in Figs. 2a-b. During further deposition of material, I observe only two relatively symmetric islands that are wide enough to spread between the edge and the center of the pattern. The wide spreading of the islands is possible due to the relatively low cost in the strain energy. The ratio of strain energy to total energy (which consists of surface and strain energies) after 10^{-5} s is 1.7% while this ratio increases to 7.8% after 5 seconds. Strain energy is increased due to deposition of additional strained material (where strain is caused by lattice mismatch between deposited film and the substrate) while the surface energy is slightly decreased. No plastic relaxation was observed during these simulations. One should note, however, that plastic deformation might occur at later stages of growth when the islands continue to grow and coalesce into a continuous film within the trench.

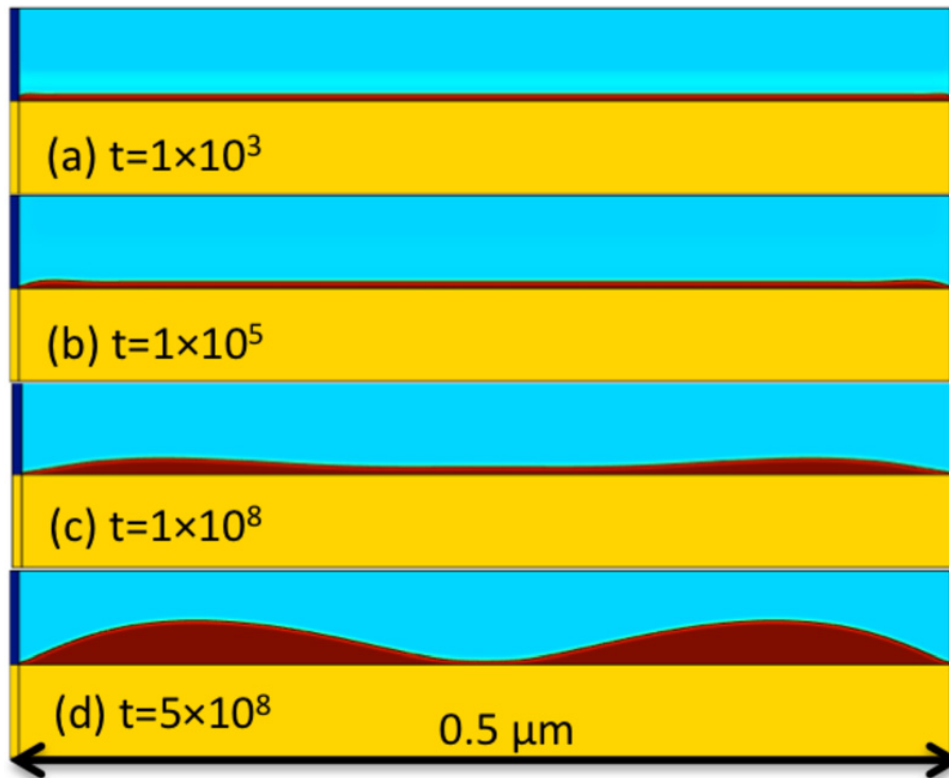


Fig. 4.2 Growth of $\text{In}_{0.1}\text{Ga}_{0.9}\text{As}/\text{GaAs}$ inside a SiO_2 pattern is shown in plots (a)-(d). Overflow deposition flux causes formation of two wide islands across the pattern.

The results of simulation for $\text{In}_{0.25}\text{Ga}_{0.75}\text{As}/\text{GaAs}$ are presented in Fig. 4.3. Except for the parameters that depend on In concentration (see Table 4.1), such as elastic properties, yield strength and surface diffusion coefficient, all other parameters are kept the same as the results for $\text{In}_{0.1}\text{Ga}_{0.75}\text{As}/\text{GaAs}$ reported in Fig. 4.2. Starting from a flat thin film, I find that perturbations in the growing film first form near the walls as shown in Fig. 4.3a-b. The same phenomenon was reported by Boyne *et al.* [20] who studied heteroepitaxial growth of Gadolinia-doped ceria on Ytria-stabilized zirconia with patches (confinement) present on the substrate. After 0.1 s, perturbations due to ATGS instabilities are extended throughout the entire trench (see Fig. 4.3c). The critical wavelength expected based on the linear elasticity theory for infinite films [21] is 84 nm, while the wavelength measured in our simulation is 91 nm. This difference can be attributed

to the effect of surface patterning, since the width of the pattern needs to accommodate an integer number of wave peaks and valleys. Since there is a wetting layer on the substrate, dewetting does not play any role in our simulations. In Fig. 4.3d, one can see that small islands are formed due to the coalescence of surface instabilities. Biased deposition flux causes faster growth rate of islands near the walls and once these islands are large enough, they absorb other small islands as shown in Fig. 4.3e. These two islands keep growing as long as I deposit the material as demonstrated in Fig. 4.3f. During the growth, strain energy of the system increases from 4.41×10^{-8} J/m after 10^{-5} s to 12.86×10^{-8} J/m after 5 s due to the deposition of additional strained material. Relatively slow surface diffusion (as compared to the deposition flux) combined with the effects of biased (overflow) flux are the most important reasons preventing coalescence of the two islands into a single island. It is easy to see that the islands in Fig. 4.3f for 0.25 In concentration have a similar size (length: ~ 130 nm, height: ~ 38 nm) and that the length of each island is much smaller than length of islands formed in the case of concentration $x = 0.1$ In concentration shown in Fig. 4.2d (length: ~ 250 nm, height: ~ 25 nm). Comparing the size of islands in these two cases shows that alloys with higher In concentration reduce their elastic energy by reducing the contact area with the substrate and by growing taller islands at the expense of increased surface energy.

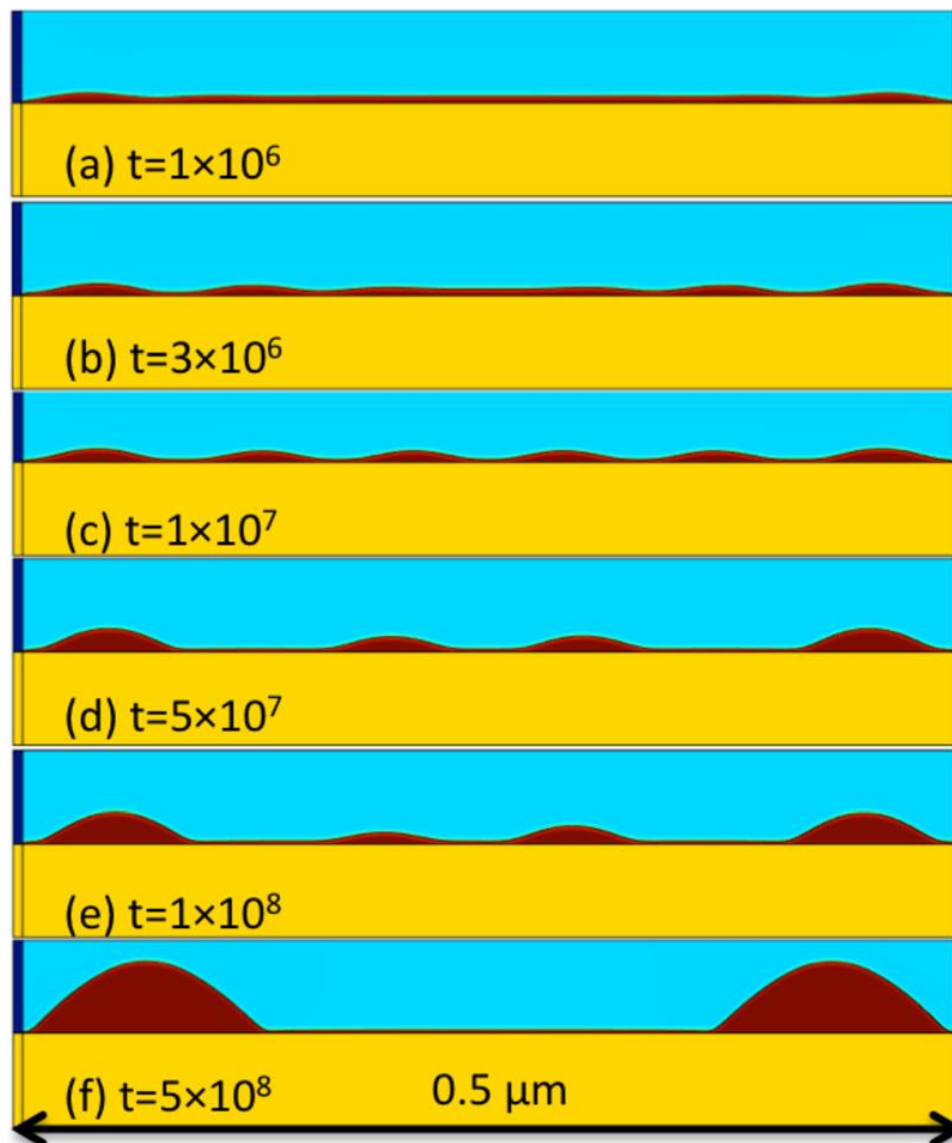


Fig. 4.3 Growth of $\text{In}_{0.25}\text{Ga}_{0.75}\text{As}/\text{GaAs}$ inside a SiO_2 pattern is plotted in a-f. ATGS instability occurs across the pattern. Small islands coalesce to form two islands near the walls driven by the effects of overflow flux.

In Fig. 4.4a I plot Von-Mises (effective) stress in the $\text{In}_{0.25}\text{Ga}_{0.75}\text{As}/\text{GaAs}$ system after 5 s of growth. I find that due to formation of the ATGS instabilities, stress in the film that was high at the early stages of growth, is now relaxed. The stress is more relaxed near the top of the islands

whereas it is still concentrated at the corners of each island (see Fig. 4.4a). Since the yield strength of the material is higher than the effective stress in the simulations, yielding does not take place. It is instructive to consider the different components of stress along the AB line. As shown in Fig. 4.4b, all the components of the stress tensor are zero in the gas phase due to zero elastic constants while there are nonzero components of stress present both in the film and the substrate. The shear stress σ_{xy} is zero both in the substrate and the film along the AB line, but I found it to be finite at the corners of the islands. σ_{yy} is tensile everywhere and its magnitude decreases monotonically from 0.3 GPa at the interface between film and the substrate to around zero near the top of the island. The most important component of the stress, σ_{xx} , is tensile in the substrate but it suddenly becomes compressive in the film. By moving away from the film-substrate interface, σ_{xx} becomes less compressive until it becomes slightly tensile at the top of the island. The presence of tensile stress at the top of the island has been reported in the literature [66-68]. Von Mises stress has its largest magnitude (about 1.8 GPa) at the film-substrate interface while it decreases to 1.6 GPa at the top of the islands and suddenly drops to zero in the gas phase. The variation of strain components along AB line is plotted in Fig. 4.4c. The eigenstrain is zero in the substrate and also in the gas phase, while it has a constant value across the film. Elastic strain ϵ_{xx} on the other hand, changes from compressive at the film-substrate interface to tensile at the top of the island. As expected, the total strain is always a sum of elastic strain and eigenstrain.

Analysis of the above results for two different low In concentrations shows that biased deposition plays an important role in formation of islands near the walls. For both concentrations, only elastic relaxation was present during growth. The effects of plastic relaxation on film morphology (present in films with higher In concentrations) are discussed in the next section.

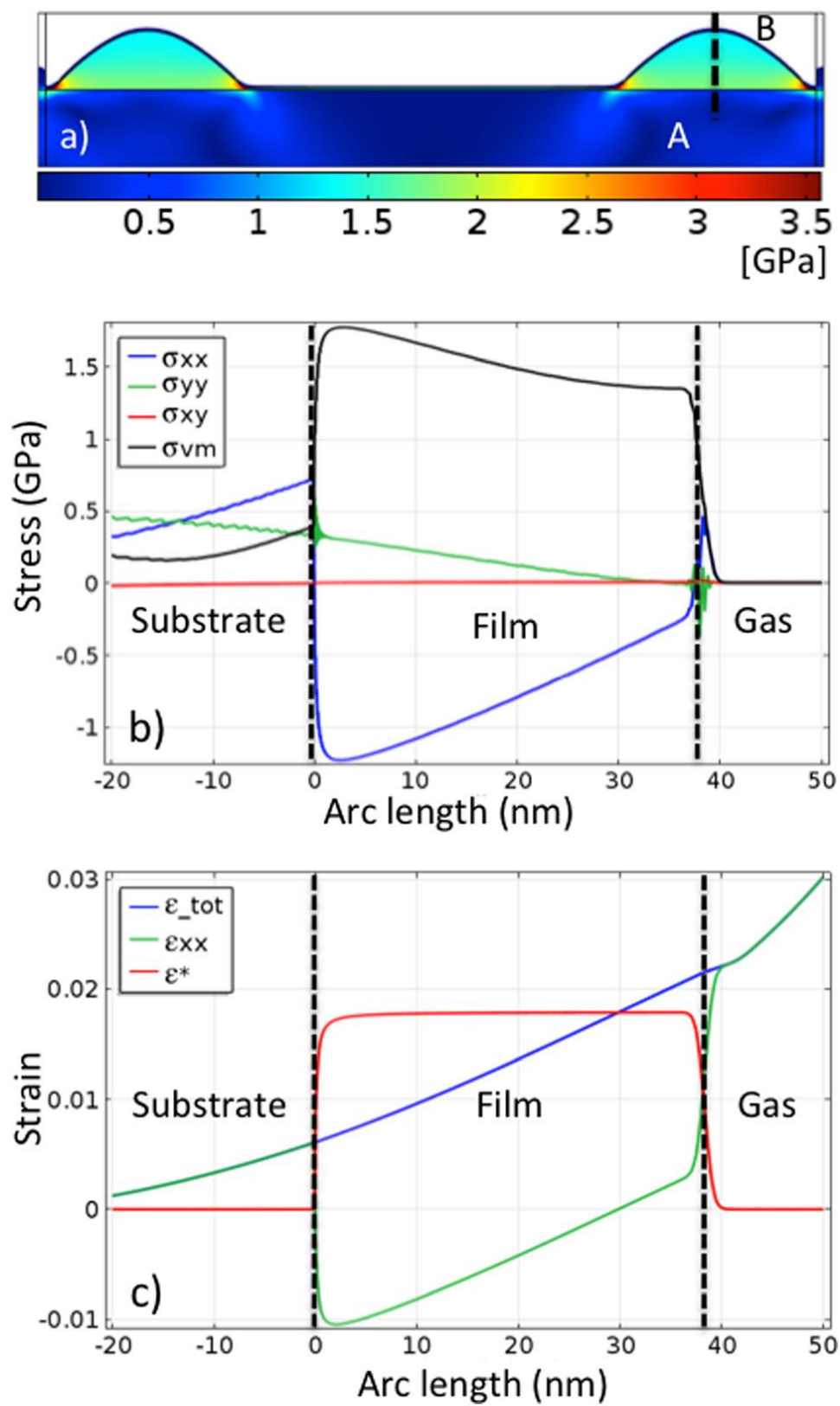


Fig. 4.4 a) Von Mises stress contour after 5×10^8 simulation steps. Maximum Von Mises stress is 3.56 GPa. Yield strength equals to 5.5 GPa. Current flow strength is 5.5 GPa. Stresses below 0.05 GPa are shown in white. b) Von Mises stress (σ_{VM} - black) and components of stress tensor (σ_{xx} - blue, σ_{yy} - green, σ_{xy} - red). c) Strain components: ϵ_{tot} (blue) is the total strain in x direction, ϵ_{xx} (green) is elastic strain in x direction and ϵ^* (red) is the eigenstrain of $In_{0.25}Ga_{0.75}As/GaAs$ inside a SiO_2 pattern along AB line. Dashed lines in plots b and c separate substrate, gas and the film.

4.4.2 High indium concentration $In_xGa_{1-x}As$ ($x > 0.4$)

I now investigate the effect of further increase of In concentration on the morphology of a heteroepitaxially grown films. For concentrations of In higher than 0.4 I observe plastic relaxation in our simulations and I investigate the effect of plastic relaxation on the film morphology.

I first study growth of $In_{0.5}Ga_{0.5}As$ on GaAs substrates. Again, all the other parameters that do not depend on In concentration were kept constant in the model. By increasing the indium concentration (x), the lattice mismatch between the film and GaAs substrate increases (see Table 4.1) and so does the accumulated stress. When the effective stress rises above the yield strength of the film, plastic deformation takes place, which partially relaxes the elastic strain and subsequently reduces strain energy of the film. As discussed in Sec. 4.4.1, for the case of $In_{0.25}Ga_{0.75}As$ ($x = 0.25$) on GaAs I found that the deposited material formed two islands at the walls (see Fig. 4.3). For comparison, in Fig. 4.5, I show the results of growth simulations for $In_{0.5}Ga_{0.5}As/GaAs$ ($x = 0.5$) inside the SiO_2 patterns. Similarly as in the case of $x = 0.25$, here I find that perturbations initiate at the edges of the trenches near the wall (see Figs. 5a-b). The ratio of elastic energy to the total energy is 28.8% after 10^{-4} s. This ratio drops to 24.5% after 10^{-3} s due to the formation of instabilities on the surface (Fig. 4.5c), which partially relaxes the strain energy

density. These instabilities grow into isolated islands and they are able to coalesce as shown in Figs. 5d-e. This coalescence causes further reduction in the ratio of elastic to total energy to 22% after 10^6 and 21.8% after 0.1 s. In this case, the maximum value of the effective plastic strain is 0.1% while the eigenstrain is about 3.5%. Interestingly, during further deposition, all the islands coalesce and form one big island away from the walls as shown in Fig. 4.5f. The plastically deformed region has grown in size at the corners of the large island and the magnitude of the maximum value of plastic strain is 3% (see Fig. 4.5g). Partial relaxation due to plastic deformation leads to a slight decrease in the ratio of elastic to total energy, which is now 21.5% after 0.18 s. Further deposition of strained material increases this ratio again to 26.1% after 1 s (due to deposition of strained material). There are two qualitative differences in the final morphologies of $\text{In}_{0.5}\text{Ga}_{0.5}\text{As}$ as (Fig. 4.5f) and of $\text{In}_{0.25}\text{Ga}_{0.75}\text{As}$ (Fig. 4.3f): (i) There is only one island formed for the case of $x = 0.5$ whereas there are two islands for $x = 0.25$; (ii) For $x = 0.5$ the island forms in the middle of the pattern whereas for $x = 0.25$ the islands form near the edges. Formation of one island instead of two reduces the area of the interface between the strained film and the substrate. For the case of $x = 0.5$ the driving force for strain relaxation is higher (because of the higher misfit strain). In addition, for $x=0.5$ surface diffusivity of $\text{In}_{0.5}\text{Ga}_{0.5}\text{As}$ is about 70% higher than surface diffusivity of $\text{In}_{0.25}\text{Ga}_{0.75}\text{As}$. Hence, small islands are able to coalesce before the deposition flux can grow islands near the walls. The effects of high surface diffusivity can also explain the second difference in morphology. Islands across the pattern find each other and coalesce due to high surface diffusivity. Once the islands grow in size, they cannot easily move since they can only move through surface diffusion of the material. I have performed 9 separate simulations for the case of $x = 0.5$, where I changed the random seed for the deposition flux. Although the exact position of the final island varies among these simulations, the qualitative conclusion that the island grows away from the walls is valid for all these simulations.

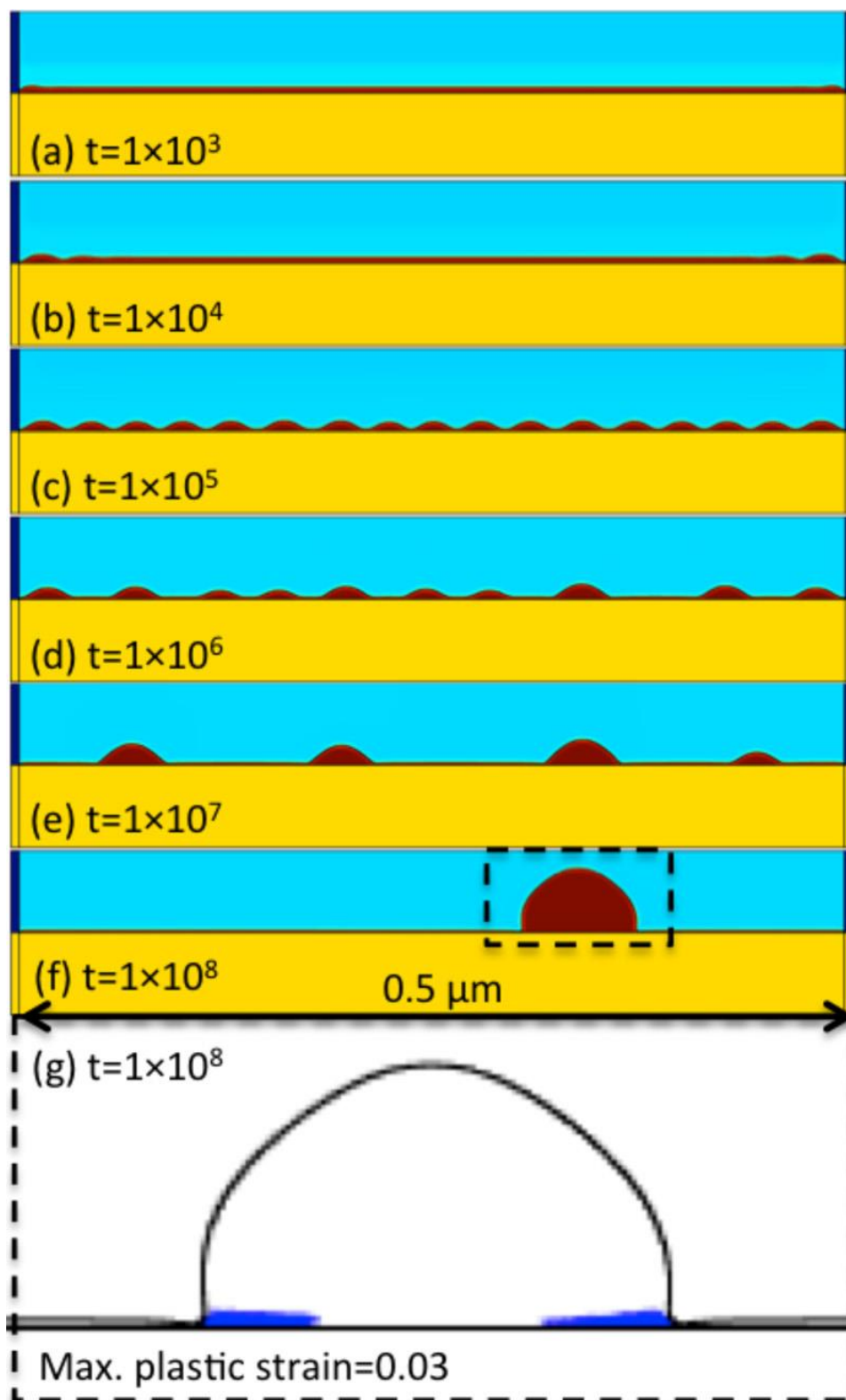


Fig. 4.5 Growth of $\text{In}_{0.5}\text{Ga}_{0.5}\text{As}/\text{GaAs}$ inside a SiO_2 pattern is depicted in plots a-f. ATGS instability happens across the pattern. Small islands coalesce and form one big island, away from the walls. Plastically deformed regions for plot f is shown in plot g.

This result demonstrates that overflow flux alone is not enough to grow islands near the edges. It competes with the effect of elastic energy and also plastic strain relaxation.

In Table 4.2, I compare the energetics associated with the growth of $\text{In}_{0.25}\text{Ga}_{0.75}\text{As}$ ($x = 0.25$), studied Sec. 4.4.1 (and plotted in Fig. 4.3) to the growth of $\text{In}_{0.5}\text{Ga}_{0.5}\text{As}$ ($x = 0.5$) on GaAs shown in Fig. 4.5. The first two columns in the table show the energetics for $\text{In}_{0.25}\text{Ga}_{0.75}\text{As}$ at the initial step and after 1 s of simulations. The last two columns of the table show the corresponding energetics for $\text{In}_{0.5}\text{Ga}_{0.5}\text{As}$. Initially, the total energy of $\text{In}_{0.25}\text{Ga}_{0.75}\text{As}/\text{GaAs}$ system is 73.74×10^{-8} J/m and the total energy of the $\text{In}_{0.5}\text{Ga}_{0.5}\text{As}/\text{GaAs}$ system is 79.88×10^{-8} J/m. After 1 s, the total energy of these systems is 44.72×10^{-8} J/m and 55.74×10^{-8} J/m, respectively. Hence one can see that for the higher indium concentration the reduction of the total energy (30.22%) is slightly smaller than the reduction of 39.35% for lower indium concentration. For both systems, the largest contribution of the total energy comes from surface and interfacial energies. This contribution is 86% for $\text{In}_{0.25}\text{Ga}_{0.75}\text{As}/\text{GaAs}$ ($x = 0.25$) and 73% for $\text{In}_{0.5}\text{Ga}_{0.5}\text{As}/\text{GaAs}$ ($x = 0.5$). Surface and interfacial energies for both cases ($x = 0.25$ and $x = 0.5$ In concentration) are very close at the initial and the final simulation time (the difference is smaller than 6%) while relatively large differences are observed in strain energies. Specifically, in $\text{In}_{0.25}\text{Ga}_{0.75}\text{As}$ the strain energy increases from 2.49×10^{-8} J/m at the beginning of simulation to 6.17×10^{-8} J/m after 1 s. The same qualitative trend is also found for $\text{In}_{0.5}\text{Ga}_{0.5}\text{As}$, but with a smaller relative increase. Plastic energy is zero at the beginning for both $\text{In}_{0.25}\text{Ga}_{0.75}\text{As}/\text{GaAs}$ and $\text{In}_{0.5}\text{Ga}_{0.5}\text{As}/\text{GaAs}$ systems. After 1 s, this energy remains zero for $x = 0.25$ system while it is 0.31×10^{-8} J/m for $x = 0.5$, as shown in Table 4.2.

Table 4.2 Energy comparison between $\text{In}_{0.25}\text{Ga}_{0.75}\text{As}$ and $\text{In}_{0.5}\text{Ga}_{0.5}\text{As}$ thin films grown on GaAs. Surface energy refers to the energy of the film surface in contact with the gas phase. Interface energy refers to the energy between film and the walls.

Composition	$\text{In}_{0.25}\text{Ga}_{0.75}\text{As}$		$\text{In}_{0.5}\text{Ga}_{0.5}\text{As}$	
	0	1	0	1
Time (s)	0	1	0	1
Surface and interface energy (10^{-8} J/m)	71.25	38.54	70.87	41.19
Strain energy (10^{-8} J/m)	2.49	6.17	9.01	14.55
Plastic energy (10^{-8} J/m)	0	0	0	0.31
Total (elastic + plastic + interfacial) energy (10^{-8} J/m)	73.74	44.72	79.88	56.05

To bring further insights into the effect of lattice mismatch and plastic relaxation on film morphology I have simulated growth of alloys with higher In concentrations. For $x=0.75$, I see trends in morphology that are qualitatively similar to those for $x = 0.5$ shown in Fig. 4.5, specifically, instabilities start near the walls, spread throughout the pattern, islands form and coalesce into a single island in the middle of the pattern. Higher In concentration reduces the wavelength of ATGS instabilities, which is 20 nm for $x = 0.75$ and 29 nm for $x = 0.5$ (Fig. 4.5c). Another difference is that for $x=0.75$, plastic deformation begins in the film early on (at $t = 1 \times 10^3$) and generally plastic strain is larger. Hence it is instructive to analyze the stress and strain the film. Von Mises stress for $\text{In}_{0.75}\text{Ga}_{0.25}\text{As}/\text{GaAs}$ after 0.16 s is shown in Fig. 4.6a. The stress in the thin film introduced by lattice mismatch is relaxed both by formation of instabilities and by plastic deformation. In this case, the flow strength in the film increases from the initial value of

3.5 GPa to value of 4.91 GPa at 0.16 s. It is worth pointing out that the GaAs substrate is also allowed to deform plastically. However, the effective stress never reaches that yields strength of 5 GPa and therefore such relaxation does not take place in the substrate. Different components of stress along AB line are plotted in Fig. 4.6b. Since the AB line cuts through the middle of an island, shear stress σ_{xy} is zero both in the film and the substrate. σ_{yy} is tensile in substrate but reduces gradually and remains slightly compressive at the top of the island. σ_{xx} is tensile in the substrate with the highest magnitude near the film substrate interface, and it abruptly switches to compressive in the film. In addition, the magnitude of σ_{xx} shows a small drop in the film near the substrate. The same behavior is observed for Von Mises stress. This drop in stress is the result of plastic relaxation and it has not been observed in Fig. 4.4b for a lower In concentration of $x = 0.25$. Strain components corresponding to the growth stage in Fig. 4.6a are plotted in Fig. 4.6c. Similarly to Fig. 4.4c, eigenstrain is constant across the film while it remains zero both in the substrate and gas. Plastic strain causes partial relaxation of elastic strain near the film-substrate interface while no plastic deformation occurs by moving away from the interface. Plastic strain remains zero both in the substrate and the gas phase. Elastic strain ϵ_{xx} , which is partially relaxed near the film-substrate interface, keeps increasing along AB line and it becomes tensile at the top of the island.

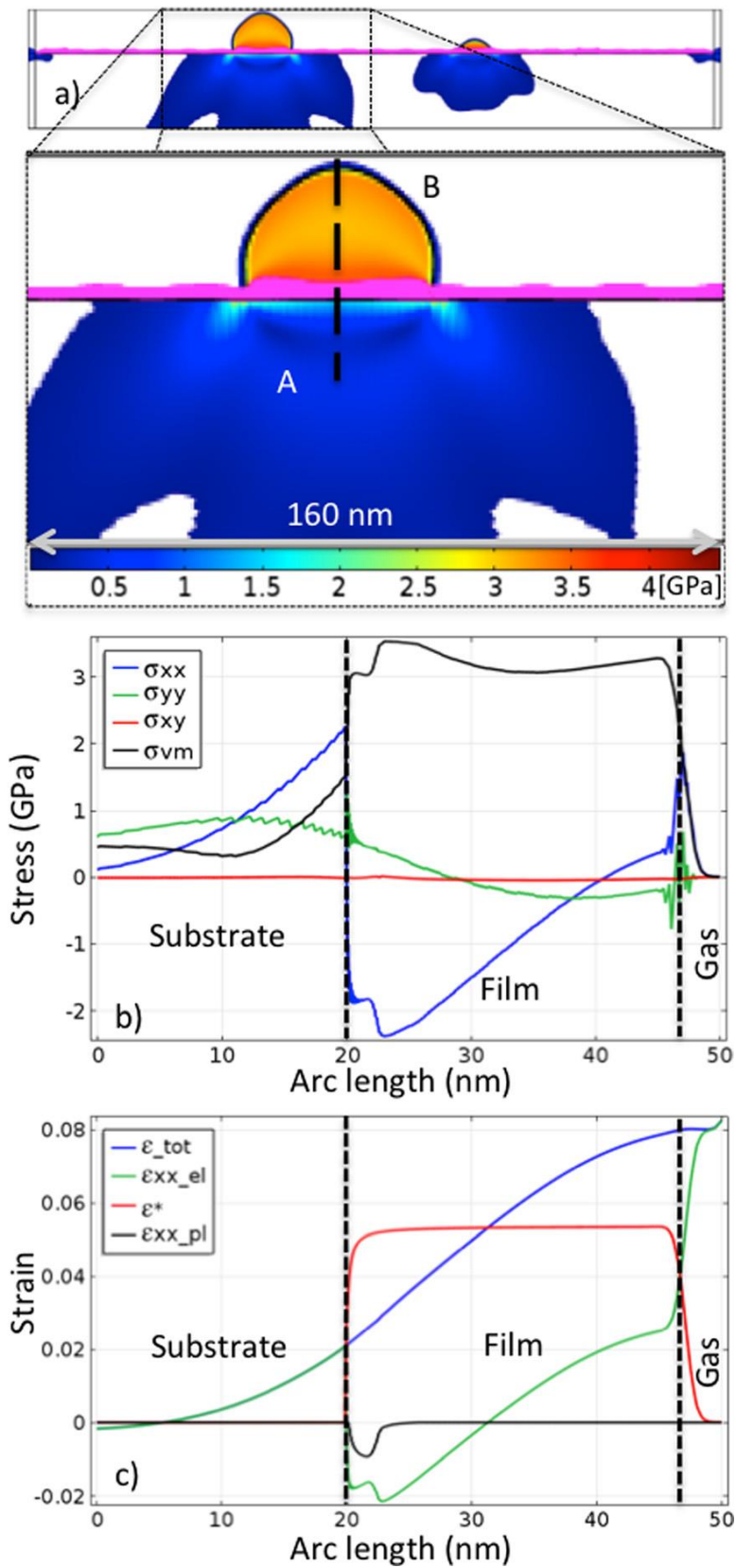


Fig. 4.6 a) Von Mises stress contour after 1.6×10^7 steps. Maximum Von Mises stress is 4.45 GPa. Initial yield strength equals to 3.5 GPa. Current flow strength is 4.45 GPa. Stresses below 0.1 GPa are shown in white, plastically deformed region is plotted in magenta. A small section of the pattern showing the stress in the island is magnified b) Von Mises stress (σ_{VM} – black) components of stress tensor (σ_{xx} – blue, σ_{yy} – green, σ_{xy} – red). c) ϵ_{tot} (blue) is the total strain in x direction, ϵ_{xx_el} (green) is elastic strain in x direction, ϵ_{xx_pl} (green) is plastic strain in x direction, and ϵ^* (red) is the eigenstrain of $\text{In}_{0.75}\text{Ga}_{0.25}\text{As}/\text{GaAs}$ inside a SiO_2 pattern along AB line. Dashed lines in plots b and c separate substrate, gas and the film.

Finally, in Fig. 4.7 I show simulation results for growth of InAs/GaAs substrate on SiO_2 patterned surface. The film has a very large lattice mismatch with the substrate ($\sim 7\%$), which causes a large compressive stress σ_{xx} in the film. The initial yield strength of InAs is assumed to be 2.5 GPa [59], which leads to an instantaneous yielding in the film. Relatively large plastic strain ($\sim 3\%$) throughout the entire flat film reduces the elastic strain ϵ_{xx} and subsequently stress σ_{xx} . Hence the ATGS instability is suppressed in the film as shown in Fig. 4.7a-b. However, high interfacial energy between the film and the walls generates instabilities near the walls shown in Fig. 4.7b. These instabilities start to grow and form islands due to the effects of the overflow deposition flux (Fig. 4.7c-d). Due to the high misfit strain, I find that the plastic deformation extends throughout the entire flat film and throughout the entire islands. Maximum plastic strain measured at a given time increases from 3% after 1×10^2 to 7% after 0.1 s. Experimental growth of InAs on GaAs substrates in $0.6 \mu\text{m}$ wide trenches with deposition flux of 1 nm/s revealed formation of random islands across the pattern while these islands coalesce and form a single nucleus[16] during growth in addition to small islands which exist near the walls in some cases. Our results for high In concentration alloys which are done under growth conditions similar to the experiments (e.g. growth temperature, flux rate, width of the pattern) are in a qualitative

agreement with experimental studies by Ganesan *et al.* [16] on InAs/GaAs systems where the randomly nucleated islands across the pattern coalesce to form a single nucleus inside the pattern.

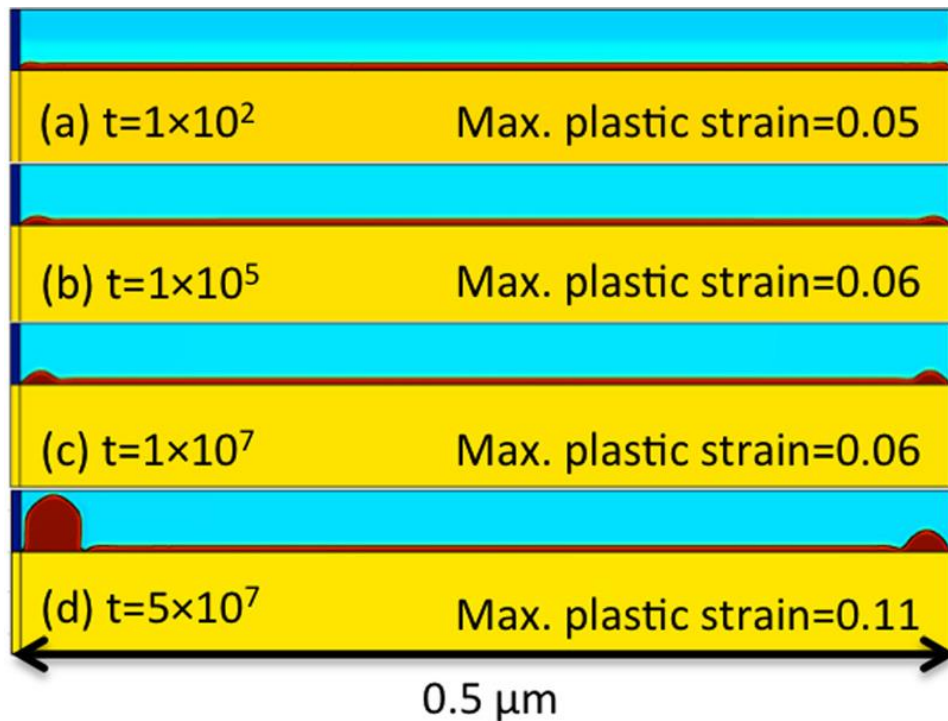


Fig. 4.7 Growth of InAs/GaAs inside a SiO₂ pattern are shown in a-d. No ATGS instability happens across the pattern. Islands are only formed at the walls.

In Table 4.3, I compare energetics for In_xGa_{1-x}As/GaAs systems for $x = 0.5, 0.75$ and 1 after 0.1 s. The morphologies for $x=0.5$ and $x=1$ can be found in Fig. 4.5 and Fig. 4.7, respectively. As shown in the last row of Table 4.3, the total energy increases due to the increase in In concentration. This energy includes contributions from elastic, plastic, and interfacial energies. Higher In concentration causes a higher lattice mismatch and subsequently a higher stress in the film. Since the yield strength decreases when In concentration increases [59], higher plastic energy is expected for higher In concentration alloys. The plastic energy per unit length at a specific time for In_{0.5}Ga_{0.5}As is 0.01×10^{-8} J/m while it is substantially higher (16.18×10^{-8} J/m) for InAs at the same time. It may be intuitive to expect an increasing trend for elastic energy per unit

length with increasing In concentration. However, my results show that the elastic strain energy for InAs is 16.35×10^{-8} J/m is actually slightly smaller than the value found for $\text{In}_{0.75}\text{Ga}_{0.25}\text{As}$ (16.61×10^{-8} J/m). The decrease in elastic energy for larger In concentration can be attributed to large plastic deformation that occurred in the entire film and relaxes the accumulated elastic energy. For InAs film grown on GaAs this energy relaxation is large enough so that the film does not form ATGS instabilities. Comparing the surface and interfacial energies in Table 4.3, one can see a 4% increase between $\text{In}_{0.75}\text{Ga}_{0.25}\text{As}$ and InAs. The interface energy is zero since there is no contact between film and the walls. Hence this difference can be explained by the surface energy (the energy between the film and the gas phases) that has two contributions, one from free energy density function $f(c)$, and the other one from the gradient energy term $\frac{\varepsilon^2}{2} |\nabla c|^2$. Although the gradient energy coefficient (ε^2) decreases by increasing In concentration as shown in Table 4.1 and hence the gradient energy contribution to the surface energy is reduced, the surface energy increases due to increase in free energy density. The same increasing trend in surface and interfacial energy is observed between $\text{In}_{0.5}\text{Ga}_{0.5}\text{As}$ and $\text{In}_{0.75}\text{Ga}_{0.25}\text{As}$.

Table 4.3 Energy comparison for $\text{In}_x\text{Ga}_{1-x}\text{As}$ thin films ($x = 0.5, 0.75$ and 1) grown on GaAs. Surface energy refers to the energy of the film surface in contact with the gas phase, which has two contributions, one from free energy density and the other one from gradient energy. Interface energy refers to the energy between film and the walls.

Composition	$\text{In}_{0.5}\text{Ga}_{0.5}\text{As}$	$\text{In}_{0.75}\text{Ga}_{0.25}\text{As}$	InAs
Surface and interface energy (10^{-8} J/m)	39.74	41.81	43.6
Strain energy (10^{-8} J/m)	11.08	16.61	16.35
Plastic energy (10^{-8} J/m)	0.01	5.24	16.18

Total (elastic + plastic + interfacial) energy (10^{-8} J/m)	50.83	63.66	76.13
--	-------	-------	-------

4.5 Conclusions

I developed a phase field model coupled with elastoplasticity to study the effects of sub-micron sized patterns on morphology of heteroepitaxial films grown on patterned substrates. This model considers the effects of anisotropy in elastic properties, non-uniform deposition flux and anisotropy in surface energy (between film and gas). To investigate the effect of lattice mismatch between the film and substrate on morphology I performed all the simulations under effects of biased deposition flux, which is observed in experiments. Diffusion coefficients, growth conditions, elastic constants, yield strengths, surface energies and lattice mismatch were chosen to correspond to the typical growth conditions of $\text{In}_x\text{Ga}_{1-x}\text{As}$ thin films on GaAs substrates patterned with SiO_2 .

My results showed that there is a competition between overflow flux, surface diffusivity, strain energy and plastic relaxation on formation of islands in SiO_2 patterned GaAs substrates. For $\text{In}_x\text{Ga}_{1-x}\text{As}$ alloys with low indium concentration (x smaller than 0.4) islands are formed at the walls mainly due to effects of overflow flux while strain energy and surface diffusivity are relatively low because of low In concentration. There is no plastic deformation happening in this regime of concentrations. On the other hand, for $\text{In}_x\text{Ga}_{1-x}\text{As}$ alloys with higher indium concentration (x larger than 0.4), surface diffusivity competes with the effect of the overflow flux to make a single island usually away from the walls. Elastic strain energy, which now has a higher value due to a higher lattice mismatch, is minimized by formation of a single island due to smaller area of strained interface. Plastic deformation partially relaxes strain energy of the island, which further reduces the motivation of the island to move. For In concentrations between 0.4 and 0.6 ($0.4 < x < 0.6$), plastic deformation only happens at the corners of the islands while for

higher In concentration ($0.6 < x < 1$) the yielded region expands to the entire thin film and the islands. Also, the ATGS surface instability is suppressed for case of $x = 1$.

4.6 Reference

- [1] S. Kohmoto, T. Ishikawa, and K. Asakawa, Japanese Journal Of Applied Physics **38**, 769 (1999).
- [2] J. Hu, L.-s. Li, W. Yang, L. Manna, L.-w. Wang, and A. P. Alivisatos, Science **292**, 2060 (2001).
- [3] A. Lorke, R. J. Luyken, A. O. Govorov, and J. P. Kotthaus, Phys. Rev. Lett. **84**, 2223 (2000).
- [4] Y. Lei, W. Cai, and G. Wilde, Prog. Mater Sci. **52**, 465 (2007).
- [5] G. M. Whitesides and B. Grzybowski, Science **295**, 2418 (2002).
- [6] S. B. Clendenning *et al.*, Adv. Mater. **16**, 215 (2004).
- [7] S. Matsui and Y. Ochiai, Nanotechnology **7**, 247 (1996).
- [8] W. Chu, H. I. Smith, and M. L. Schattenburg, Appl. Phys. Lett. **59**, 1641 (1991).
- [9] S. Kramer, R. R. Fuieler, and C. B. Gorman, Chem. Rev. **103**, 4367 (2003).
- [10] D. Y. Ryu, K. Shin, E. Drockenmuller, C. J. Hawker, and T. P. Russell, Science **308**, 236 (2005).
- [11] S. Jha, C. C. Liu, T. S. Kuan, S. E. Babcock, P. F. Nealey, J. H. Park, L. J. Mawst, and T. F. Kuech, Appl. Phys. Lett. **95**, 062104 (2009).
- [12] G. Brammertza, M. R. Caymax, Y. Mols, S. Degroote, M. Leys, J. V. Steenbergen, G. Winderickx, G. Borghs, and M. M. Meurisd, ECS Transactions **3**, 585 (2006).
- [13] J. Martin-Sanchez, P. Alonso-Gonzalez, J. Herranz, Y. Gonzalez, and L. Gonzalez, Nanotechnology **20**, 125302 (2009).
- [14] V. C. Elarde, T. S. Yeoh, R. Rangarajan, and J. J. Coleman, J. Cryst. Growth **272**, 148 (2004).
- [15] T. Hoshii, M. Deura, M. Sugiyama, R. Nakane, S. Sugahara, M. Takenaka, Y. Nakano, and S. Takagi, Physical Status Solidus C **5**, 2733 (2008).

- [16] S. Ganesan, PhD thesis, University of Wisconsin – Madison, 2006.
- [17] Z. R. Zytewicz, J. Domagala, D. Dobosz, and J. Bak-Misiuk, *J. Appl. Phys.* **86**, 1965 (1999).
- [18] K. Brunner, *Rep. Prog. Phys.* **65**, 27 (2002).
- [19] E. Jiran and C. Thompson, *Thin Solid Films* **208**, 23 (1992).
- [20] A. Boyne, M. D. Rauscher, S. A. Dregia, and Y. Wang, *Scripta Mater.* **64**, 705 (2011).
- [21] R. J. Asaro and W. A. Tiller, *Metallurgical Transactions* **3**, 1789 (1972).
- [22] M. A. Grinfeld, *Doklady Akademii Nauk SSSR* **290**, 1358 (1986).
- [23] D. J. SROLOVITZ, *Acta Metall.* **37**, 621 (1989).
- [24] G. S. Solomon, J. A. Trezza, and J. S. Harris, *Appl. Phys. Lett.* **66**, 991 (1995).
- [25] H. J. Gao and W. D. Nix, *Annu. Rev. Mater. Sci.* **29**, 173 (1999).
- [26] C. S. Ozkan, W. D. Nix, and H. J. Gao, *Appl. Phys. Lett.* **70**, 2247 (1997).
- [27] A. G. Cullis, A. J. Pidduck, and M. T. Emeny, *Phys. Rev. Lett.* **75**, 2368 (1995).
- [28] J. Tersoff and F. K. Legoues, *Phys. Rev. Lett.* **72**, 3570 (1994).
- [29] D. E. Jesson, S. J. Pennycook, J. M. Baribeau, and D. C. Houghton, *Phys. Rev. Lett.* **71**, 1744 (1993).
- [30] P. Kratzer, E. Penev, and M. Scheffler, *Appl. Surf. Sci.* **216**, 436 (2003).
- [31] X. Su, R. K. Kalia, A. Nakano, P. Vashishta, and A. Madhukar, *Appl. Phys. Lett.* **79**, 4577 (2001).
- [32] T. P. Schulze and P. Smereka, *Commun Comput Phys* **10**, 1089 (2011).
- [33] B. J. Spencer, P. W. Voorhees, and J. Tersoff, *Phys. Rev. Lett.* **84**, 2449 (2000).
- [34] J. Tersoff, *Phys. Rev. Lett.* **87**, 156101 (2001).
- [35] J. J. Eggleston, PhD Thesis, NORTHWESTERN UNIVERSITY, 2001.
- [36] N. Moelans, B. Blanpain, and P. Wollants, *Computer Coupling of Phase Diagrams and Thermochemistry* **32**, 268 (2008).

- [37] K. Thornton, J. Agren, and P. W. Voorhees, *Acta Materialia* **51**, 5675 (2003).
- [38] S. M. Wise and W. C. Johnson, *J. Appl. Phys.* **94**, 889 (2003).
- [39] Y. Tu and J. Tersoff, *Phys. Rev. Lett.* **98**, 096103 (2007).
- [40] Y. Tu and J. Tersoff, *Phys. Rev. Lett.* **93**, 216101 (2004).
- [41] L.-Q. Chen, *Annu Rev Mater Res* **32**, 113 (2002).
- [42] K. Kassner and C. Misbah, *Europhys. Lett.* **46**, 217 (1999).
- [43] J. Drucker, *Phys Rev B* **48**, 18203 (1993).
- [44] D. J. Seol, S. Y. Hu, Z. K. Liu, L. Q. Chen, S. G. Kim, and K. H. Oh, *J. Appl. Phys.* **98**, 044910 (2005).
- [45] D.-H. Yeon, P.-R. Cha, and M. Grant, *Acta Materialia* **54**, 1623 (2006).
- [46] B. J. Spencer, P. W. Voorhees, and J. Tersoff, *Phys Rev B* **64**, 235318 (2001).
- [47] S. M. Wise, J. S. Lowengrub, J. S. Kim, and W. C. Johnson, *Superlattices Microstruct.* **36**, 293 (2004).
- [48] Y. U. Wang, Y. M. Jin, A. M. Cuitino, and A. G. Khachaturyan, *Acta Mater.* **49**, 1847 (2001).
- [49] Y. U. Wang, Y. M. Jin, A. M. Cuitino, and A. G. Khachaturyan, *Appl. Phys. Lett.* **78**, 2324 (2001).
- [50] M. Haataja, J. Muller, A. D. Rutenberg, and M. Grant, *Phys Rev B* **65**, 035401 (2002).
- [51] M. Haataja, J. Muller, A. D. Rutenberg, and M. Grant, *Phys Rev B* **65**, 165414 (2002).
- [52] Y. U. Wang, Y. M. M. Jin, and A. G. Khachaturyan, *Acta Mater.* **51**, 4209 (2003).
- [53] M. Cottura, Y. Le Bouar, A. Finel, B. Appolaire, K. Ammar, and S. Forest, *J Mech Phys Solids* **60**, 1243 (2012).
- [54] X. H. Guo, S. Q. Shi, and X. Q. Ma, *Appl. Phys. Lett.* **87**, 221910 (2005).
- [55] A. Gaubert, Y. Le Bouar, and A. Finel, *Philosophical Magazine* **90**, 375 (2010).
- [56] T. Nishinaga, *J. Cryst. Growth* **237**, 1410 (2002).

- [57] J. W. Cahn and J. E. Hilliard, *J. Chem. Phys.* **28**, 258 (1958).
- [58] S. M. ALLEN and J. W. CAHN, *Acta Metall.* **27**, 1085 (1979).
- [59] S. Korte, I. Farrer, and W. J. Clegg, *J Phys D Appl Phys* **41**, 205406 (2008).
- [60] J. W. Cahn, *J. Chem. Phys.* **66**, 3667 (1977).
- [61] S. M. Wise, J. S. Kim, and W. C. Johnson, *Thin Film Solids* **473**, 151 (2005).
- [62] J. W. CAHN, *Acta Metall.* **9**, 795 (1961).
- [63] E. Placidi *et al.*, in *Self-Assembly of Nanostructures: The INFN Lectures*, edited by Springer(2012).
- [64] M. Kasu and N. Kobayashi, *J. Cryst. Growth* **145**, 120 (1994).
- [65] M. Rosini, M. C. Righi, P. Kratzer, and R. Magri, *Phys Rev B* **79**, 075302 (2009).
- [66] H. Ye, Z. Y. Yu, P. F. Lu, Y. M. Liu, and L. H. Han, *J. Appl. Phys.* **114**, 093504 (2013).
- [67] R. Gatti, A. Marzegalli, V. A. Zinovyev, F. Montalenti, and L. Miglio, *Phys Rev B* **78**, 184104 (2008).
- [68] X. D. Liang, Y. Ni, and L. H. He, *Computational Materials Science* **48**, 871 (2010).

Chapter 5 **Control of surface induced phase separation in immiscible semiconductor alloy core-shell nanowires**

Published in Computational Materials Science, Volume 130 (2017) 50-55

5.1 **Abstract**

Semiconductor nanowires have been shown to exhibit novel optoelectronic properties with respect to bulk specimens made of the same material. However, if a semiconductor alloy has a miscibility gap in its phase diagram, at equilibrium it will phase separate, leading to deterioration of the aforementioned properties. One way to prevent this separation is to grow the material at low temperatures and therefore to suppress kinetics. Such growth often needs to be followed by high-temperature annealing in order to rid the system of undesirable growth-induced defects. In this study, I propose a method to control phase separation in core-shell nanowires during high temperature annealing by tailoring geometry and strain. Using a phase field model I determined that phase separation in nanowires begins at the free surface and propagates into the bulk. I discovered that including a thin shell around the core delays the phase separation whereas a thick shell suppresses the separation almost entirely.

5.2 **Introduction**

High surface to volume ratio and the possibility of a lateral strain relaxation make nanowires promising candidates for growth of semiconductor structures. Semiconductor nanowires have shown outstanding electronic and optical properties, and therefore are being considered for use as lasers [1], light emitting diodes [1,2], transistors [3] and sensors [4]. In particular, many studies have focused on nanowires made of III-V semiconductors because the band gap energy in these materials can be controlled by alloy composition [5,6]. One challenge in growing multi-component heterostructures, such as InGaAs, AlGaAs, and GaAsSb, is that these alloys have a miscibility gap in their phase diagrams and therefore at equilibrium these alloys phase separate

[7]. During growth process, phase separation can be kinetically inhibited for most III-V semiconductors because of the relatively low growth temperatures. However, these materials often need to be subsequently annealed in order to remove defects introduced during growth and the high temperature annealing can lead to undesirable phase separation. For instance, Luna *et al.* [8] found spontaneous formation of a lateral composition modulation (LCM) in GaAsBi epilayers grown by Molecular Beam Epitaxy (MBE). Hsieh *et al.* [9] observed LCM in AlGaAs film upon annealing and found that the phase separation was more pronounced near the free surface. The authors proposed a stress-driven vacancy-assisted mechanism to be responsible for this phenomenon. Tang *et al.* [10] used linear stability theory to study the role of free surfaces in spontaneous phase separation of alloys in thin films and found that stress relaxation begins at the surface. However, Tang *et al.* did not study the effects of geometry and strain on formation of surface induced compositional modulations. Also they did not investigate potential pathways for controlling this phase separation.

As shown experimentally, the existence of a miscibility gap in phase diagrams of III-V semiconductors leads to compositional modulation during growth and annealing [8,9]. Here, I propose a method to control such phase separation under conditions where phase separation is thermodynamically favorable and kinetically allowed. This method takes advantage of the strain induced by a core-shell geometry of a nanowire. The effects of different factors, such as the miscibility gap, surface and bulk diffusion, and elastic strains, on the compositional modulation in the nanowire structure are investigated using the phase field model.

5.3 Model

I model the annealing process of the nanowires made of a generic immiscible alloy using phase field method combined with elasticity governing equations. I developed this continuum-based model earlier to study the growth of thin films on patterned substrates [11] and continuum approaches have been found to be applicable for strain and stress field calculations in core-shell

nanowires [12]. In my model I do not account for possible faceting of the nanowires because my goal is to demonstrate the general effect of a shell on phase separation. For a given material pair, faceting may or may not play a role in phase separation and this effect should be further investigated. In this study, I do not include the effect of plastic deformations since they do not happen at the length scale of interest based on both theoretical predictions [13] and experimental observations [14-16].

The model assumes a rotational symmetry along the axis of the nanowire. The circumferential component (u_θ) of the displacement field is zero while the radial (u_r) and the axial (u_z) components of the displacement field are treated as variables. Displacement and traction vector continuity is assumed at all internal boundaries. The substrate is fixed (no displacements along r and z directions) at the bottom while all the external boundaries are traction-free. Semiconductor nanowires have been grown experimentally with diameters as small as 3 nm [17]. However, the range of diameters of interest is usually between 15-100 nm [15,18,19] due to difficulties associated with the growth of very small nanowires (<10 nm in diameter) and no practical advantage of larger nanowires (>100 nm in diameter) [17]. Throughout this study, the height of the nanowire and the diameter of the core are kept constant and equal to 200 nm and 20 nm, respectively, while the shell material and thickness (t_s) vary. GaAsSb is chosen as an example of immiscible alloy for the core nanowire. GaAsSb is thermodynamically unstable at 650 °C and under equilibrium condition, it phase separates to GaAs-rich and GaSb-rich phases. Given that this phase separation process is effectively determined by interdiffusion of As and Sb on the same sublattice, diffusion of Ga does not play an important role and hence I have not included the diffusivity of Ga in this model. Hence I use a single concentration variable in the model. I use the effective diffusion coefficient with the value of $1 \times 10^{-18} \text{ cm}^2 \text{ s}^{-1}$ [20], which was determined in experimental studies of Sb diffusion in GaAs. I define free energy density functional as

$$F = \int_{\Omega} \left(f(c) + W(c) + \frac{\varepsilon^2}{2} |\nabla c|^2 \right) d\Omega \quad 5-1$$

where Ω represents the system volume, W is the strain energy density, ε^2 is the gradient energy coefficient, f is the free energy density, and c is the concentration of Sb. For GaAsSb at 650 °C, the excess Gibbs free energy is taken from CALPHAD calculations [21] and it is given by

$$f_{core} = \frac{(G_{ideal} + L_{GaAsSb}^0 c(1-c) + L_{GaAsSb}^1 c(1-c)(1-2c))}{V_m^{GaAs}} \quad 5-2$$

where V_m^{GaAs} is the molar volume of GaAs and G_{ideal} the ideal Gibbs free energy. The interaction parameters L_{GaAsSb}^0 and L_{GaAsSb}^1 are defined as follows

$$G_{ideal} = RT(c \ln(c) + (1-c) \ln(1-c)) \quad 5-3$$

$$L_{GaAsSb}^0 = 24824 - 7.74301 \times T \quad 5-4$$

$$L_{GaAsSb}^1 = 4774 \quad 5-5$$

where R is the gas constant, and T is the temperature in Kelvin. For numerical reasons, I fitted the Gibbs free energy with a ninth order polynomial (shown in Fig. 5.1) and I used this polynomial function in my model. The polynomial function is given by

$$\begin{aligned} G_{ideal} = & -3.14808 \times 10^6 - 4.81905 \times 10^8 c + 5.02091 \times 10^9 c^2 - 2.64836 \times 10^{10} c^3 + \\ & 8.04754 \times 10^{10} c^4 - 1.4885 \times 10^{11} c^5 + 1.63584 \times 10^{11} c^6 - 9.76861 \times 10^{10} c^7 + 2.44215 \times \\ & 10^{10} c^8 + 2.01987 c^9 \end{aligned} \quad 5-6$$

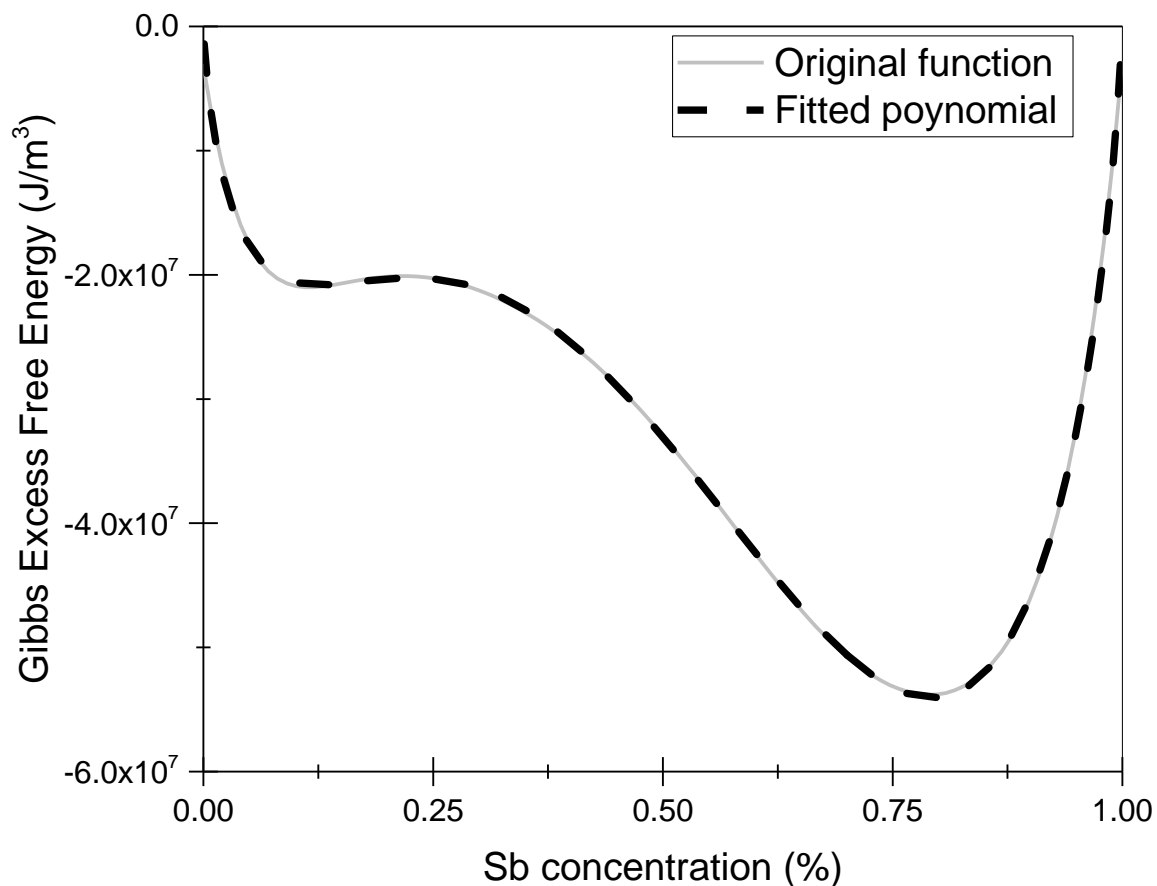


Fig. 5.1 Excess Gibbs free energy of GaAsSb at 650 °C (solid line). Ninth order polynomial has been used to fit the function (dashed line).

For the shell, I have chosen a material (GaAs) that is thermodynamically stable material at the temperature of interest (650 °C) and hence in my formulation it is sufficient to use a single-welled free energy density [22] as follows

$$f_{shell/substrate} = \alpha_0 c^2 \quad 5-7$$

where α_0 is a positive coefficient representing the sharpness of the single-welled function.

The second term in free energy functional shown in Eq. (5-1) is strain energy density W that is defined as

$$W(c) = \frac{1}{2} \sigma_{ij} e_{ij}^{el} \quad 5-8$$

σ_{ij} is the Cauchy stress tensor, and e_{ij}^{el} is the elastic strain tensor. Elastic strain tensor satisfies the following relationship

$$e_{ij}^{el} = e_{ij}^{tot} - e_{ij}^* \quad 5-9$$

where e_{ij}^{tot} is the total strain and e_{ij}^* is the eigenstrain, which arises due to the lattice mismatch between core/shell and the substrate. e_{ij}^* is given by

$$e_{ij}^* = \frac{a_{core/shell} - a_{substrate}}{a_{substrate}} \delta_{ij} \quad 5-10$$

where a is the lattice parameter of different parts of the nanowire specified in the subscript and δ_{ij} is the Kronecker delta. I use a linear interpolation to calculate the lattice mismatch between the core/the shell and the substrate as a function of alloy concentration. Assuming a linear strain-displacement relationship (which is valid for an infinitesimal strain), I solve equilibrium equations to find the total strain. Both the strain-displacement and the equilibrium equations can be found in Ref. [11].

The third term in free energy functional shown in Eq. (5-1) is interfacial energy that is a function of ε^2 and c . In my model, c is a conserved field variable that evolves according to the mass conservation equation

$$\frac{\partial c}{\partial t} = -\nabla \cdot J \quad 5-11$$

where J is the density flux and it is related to the gradient of variational derivative of the free energy density functional as

$$J = -M \nabla \frac{\delta F}{\delta c} = -M \nabla \left(\frac{\partial f}{\partial c} + \frac{\partial W^{el}}{\partial c} - \nabla \cdot (\varepsilon^2 \nabla c) \right) \quad 5-12$$

here M is the effective mobility of alloy. Mobility and diffusivity are related to each other through $MRT = DV_m$ [23], where D is diffusivity and V_m is the molar volume. There are two separate mass

transport mechanisms included in my model, which are the surface and the bulk diffusion. In this model, the diffusion coefficient changes from $1 \times 10^{-8} \text{ cm}^2 \text{ s}^{-1}$ at the surface (in the region corresponding to the thickness of 3 monolayers) to $1 \times 10^{-18} \text{ cm}^2 \text{ s}^{-1}$ in the bulk. The thickness of the surface region is in agreement with the thickness of 2-4 monolayers reported in the literature based on experimental observations [24]. Combining Eqs. (5-11) and (5-12), the evolution equation, known as the Cahn-Hilliard equation, can be found

$$\frac{\partial c}{\partial t} = \nabla \cdot \left[M \nabla \left(\frac{\partial f}{\partial c} + \frac{\partial W^{el}}{\partial c} - \nabla \cdot (\varepsilon^2 \nabla c) \right) \right] \quad 5-13$$

Eqs. (5-1) and (5-13) show that the strain energy is coupled to the phase field model. This coupling means that in order to find the unknown variables in the model, I need to simultaneously solve for the Cauchy-Navier (equilibrium) equations in both the radial and the axial directions and the Cahn-Hilliard equation. Here the unknowns are the two displacement fields (u_r and u_z) and the concentration field (c). All energy values in the model are defined per unit of length. The aforementioned system of partial differential equations is solved using the finite element method as implemented in the COMSOL software. In the finite element mesh, I used 10 grid points per unit of length (1 nm), which means that each grid has dimensions of 1 Å by 1 Å.

A schematic view of the nanowire structure is shown in Fig. 5.2a. The model consists of a substrate, a cap and a core. The shell will be shown in subsequent figures. The substrate is made of GaAs and the shell is made either of material GaAs or a composition of alloy GaAsSb to produce compressive or tensile strain in the core, respectively. The cap is made of a single element material and is chosen to be lattice matched with the core-nanowire. The results presented in this paper are not unique to a single semiconductor alloy and can be applied to alloys that have a miscibility gap at high temperatures ($< 700 \text{ }^\circ\text{C}$) and that have a relatively high bulk diffusivity in the temperature range of interest. There are multiple phenomena that affect the phase separation in the core-shell nanowire. I isolated these phenomena to study the effect of each

on the phase separation. In order to study the effects of misfit strain between core and shell and also shell thickness on phase separation in the core, I first assumed that there is no mass transport (i.e., atomic mixing) between different sections of the nanowire (substrate, cap, core, and shell). I then include the possibility of intermixing to elucidate the effect of mass transport between core and shell on phase separation in the core.

The material in the core is $\text{GaAs}_{0.6}\text{Sb}_{0.4}$, which separates into two phases under equilibrium conditions at 650 °C. GaAs-rich alloy ($\text{GaAs}_{0.92}\text{GaSb}_{0.08}$) and GaSb-rich alloy ($\text{GaAs}_{0.27}\text{GaSb}_{0.73}$). This composition of GaAsSb is chosen because it is in the middle of a tie line of the phase diagram at the temperature of interest. Material properties of $\text{GaAs}_{1-x}\text{Sb}_x$ are calculated using a linear interpolation between properties of GaAs ($x=0$) and GaSb ($x=1$). For GaAs I take the following values for material properties [11]: elastic constants $C_{11}=118.8$ GPa, $C_{12}=53.4$ GPa, and $C_{44}=59.6$ GPa, surface diffusion coefficient equal to 1×10^{-8} $\text{cm}^2 \text{s}^{-1}$. GaSb is assumed to have the following properties [25]: elastic constants $C_{11}=83.3$ GPa, $C_{12}=40.2$ GPa, and $C_{44}=43.2$ GPa, misfit strain with respect to GaAs equal to 7.83%. Bulk diffusion coefficient for GaAsSb is taken to be 1×10^{-18} $\text{cm}^2 \text{s}^{-1}$ [20]. Surface diffusivity of GaSb is assumed to be equal to the surface diffusivity of GaAs. Annealing temperature is 650 °C. The interfacial energy γ between GaAs and GaSb is 0.08 J/m². This value is calculated from the Young's equation knowing the surface energies of GaAs to be equal to 0.71 J/m² [26] and GaSb which is 0.63 J/m² [27], knowing that GaAsSb starts to grow in a layer-by-layer mode on GaAs [28] and hence the contact angle is zero. Following Cahn and Hilliard [29], gradient energy coefficient ε_0^2 is calculated from $\gamma = \int_{0.077}^{0.73} \sqrt{2\varepsilon_0^2 f(c)}$ to be 6.52×10^{-10} J/m. I normalize the simulation parameters by defining three characteristic units: e^* is the characteristic energy chosen to be 10^{10} J m⁻³, l^* is the characteristic length which is equal to 10^{-9} m, and t^* is the characteristic time taken to be 10^{-8} s. Using these characteristic units, one can define dimensionless quantities for the free energy density ($f^* = \frac{f}{e^*}$),

the elastic moduli ($C_{ij}^* = \frac{C_{ij}}{e^*}$), the strain energy density ($W^* = \frac{W}{e^*}$), the gradient energy coefficient ($\varepsilon^{*2} = \frac{\varepsilon^2}{l^{*2} \cdot e^*}$) and the mobility ($M^* = \frac{M \cdot t \cdot e^*}{l^{*2}}$). Finally, the non-dimensional form of the Cahn-Hilliard equation is

$$\frac{\partial c}{\partial \hat{t}} = \nabla \cdot \left[M^* \nabla \left(\frac{\partial f^*}{\partial c} + \frac{\partial W^{el^*}}{\partial c} - \nabla \cdot (\varepsilon^{*2} \nabla c) \right) \right] \quad 5-14$$

where \hat{t} is the computational time step and ∇ represents gradient with respect to non-dimensional variables \hat{x} and \hat{y} .

The results shown in this paper are generated using a 2D axisymmetric model of the nanowire because such model is computationally less expensive than a full 3D model. I have compared and validated the results of the 2D model against a full 3D model for selected cases and found the results to be similar. Specifically, the phase separation in both models starts at the free surface and then propagates inside the material. Also, in both models I observed that the phase separation is delayed when there is a thin shell around the core and by increasing the thickness of the shell the phase separation is suppressed. Comparison between 2D and 3D models is more qualitative since some of the parameters such as the interfacial energy coefficient have different values in 2D and 3D models and hence a quantitative comparison is difficult.

5.4 Results

I first use my model to understand the role of free surfaces in phase separation of semiconductor nanowires and therefore I simulate annealing of a core-only nanowire (i.e., shell thickness $t_s=0$). I begin the simulation with a homogenous GaAs_{0.6}Sb_{0.4} nanowire on a GaAs substrate (Fig. 5.2a). After annealing for 7×10^4 s, compositional modulations develop at the free surface, as shown in Fig. 5.2b. At this point in time, only 60% of the alloy is phase separated (the cutoff for phase separation in this study is chosen to be $\pm 2.5\%$ of the initial composition). There are two driving forces for phase separation. The first driving force is the relaxation of the stress

(and the strain energy) near the substrate as the GaAs-rich phase newly formed at the bottom of the nanowire has a lower misfit strain with the substrate. The second driving force is the reduction in bulk free energy, since phase separation is thermodynamically favorable. Formation of LCM during annealing has been previously observed experimentally in III-V semiconductors by Hsieh *et al.* [9] and studied theoretically by Tang *et al.* [10]. After annealing for a longer time, my simulations reveal that phase separation propagates toward the center of the nanowire and, for instance, at 5×10^5 s about 93% of the original homogenous alloy is phase separated into GaAs-rich and GaSb-rich phases (Fig. 5.2c). Propagation of compositional modulation into the bulk is driven by relaxation of alloy's bulk free energy. Although, the strain energy cost for formation of axial heterostructures acts as a counterbalance force that slows down the propagation process, this energy cost is relatively low. Specifically, due to phase separation, strain energy increases by 0.106×10^{-8} J while bulk free energy decreases by 1.495×10^{-8} J (Fig. 5.2d). In addition, the difference between lattice parameters (and hence volumes) of GaAs-rich and GaSb-rich phases causes formation of undulations at the free surface, as shown in the magnified view in Fig. 5.2c. These undulations partially relax the epitaxial stress.

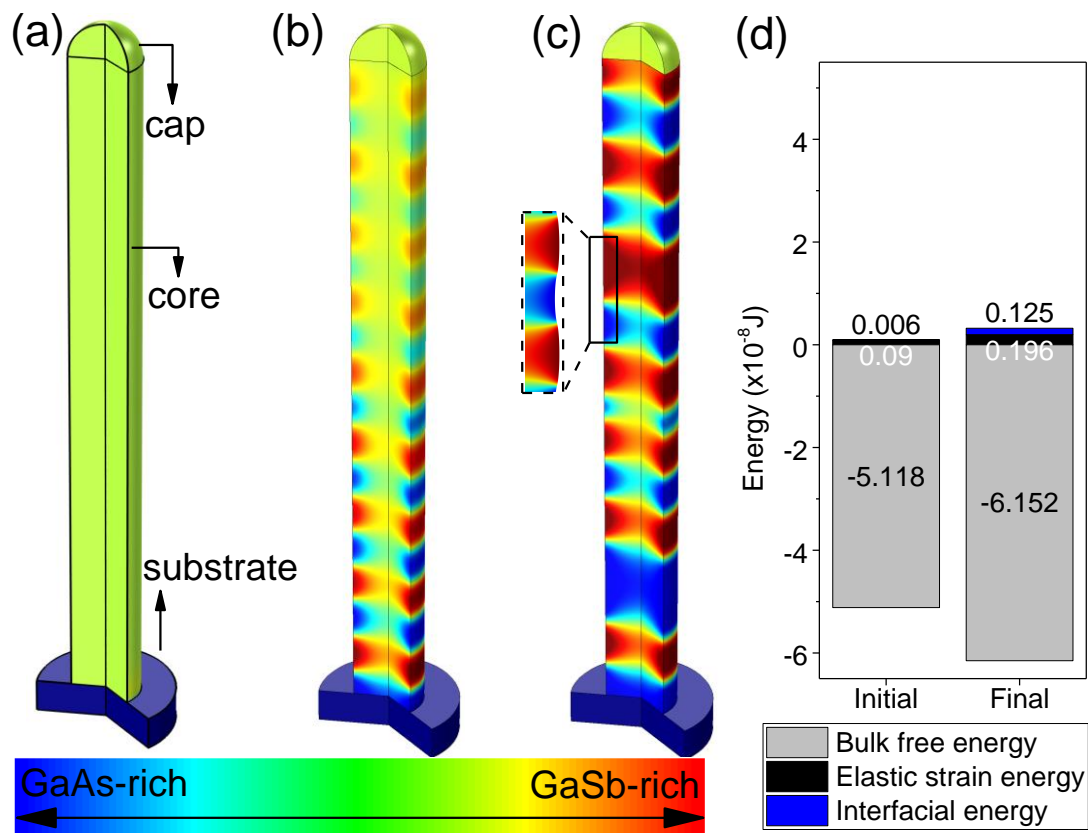


Fig. 5.2 GaAsSb core-only nanowire during annealing a) before annealing, b) after 7×10^4 s and c) after 5×10^5 s of annealing at 650°C . Separated phases are GaSb-rich phase (red) and GaAs-rich phase (blue). d) Contribution of different energy components before annealing and after annealing for 5×10^5 s.

Keeping in mind that phase separation is usually not desirable for opto-electronic applications of III-V semiconductors, I next focus on possible pathways for suppressing it. Specifically, I investigate whether including a shell around the nanowire's core can allow for control of phase separation in the regime where phase separation is thermodynamically favorable. To answer this question, I consider two specific cases. First, I include a thin shell ($t_s=0.5$ nm) made of GaAs around the core as shown in Fig. 5.3a. The 0.5 nm thickness corresponds to approximately 1

monolayer. Given that the lattice parameter of GaAs is smaller than GaAsSb, the shell imposes a compressive strain to the core. The purpose of having a thin shell around the core-nanowire is to enforce a kinetic constraint by substituting surface diffusivity with bulk diffusivity and therefore to determine the effect of surface diffusion on compositional modulation. My results (Fig. 5.3) show that a thin shell only delays phase separation, but it does not suppress it entirely. This delay is due to the fact that a shell (even if it is thin) eliminates the fast surface diffusivity and as a result the kinetics is controlled by slower bulk diffusivity. Phase separation is still initiated at the core surface (which has now become the core-shell interface) and the same driving force as discussed for the core-only nanowire is active here. However, in the case of the thin-shell nanowire there is an additional force that opposes phase separation. This opposing force is associated with the misfit strain between core and the shell, but it is not large enough to suppress the separation. After annealing the nanowire for 7×10^4 s, 13% of the alloy is phase separated, which is significantly lower than 60% of phase separation observed in the nanowire that does not have a shell around it as shown in Fig. 5.2. After longer annealing time (5×10^5 s), the phase separated region extends toward the center of the nanowire (Fig. 5.3a). At this point, 90% of phase separation is observed in nanowire that is comparable to 93% that was observed for only core nanowire. Contributions of different energy components to the total energy at the beginning of the annealing process and after 5×10^5 s are shown in Fig. 5.3c. Bulk free energy (grey) is the dominant term, but it decreases slightly over time.

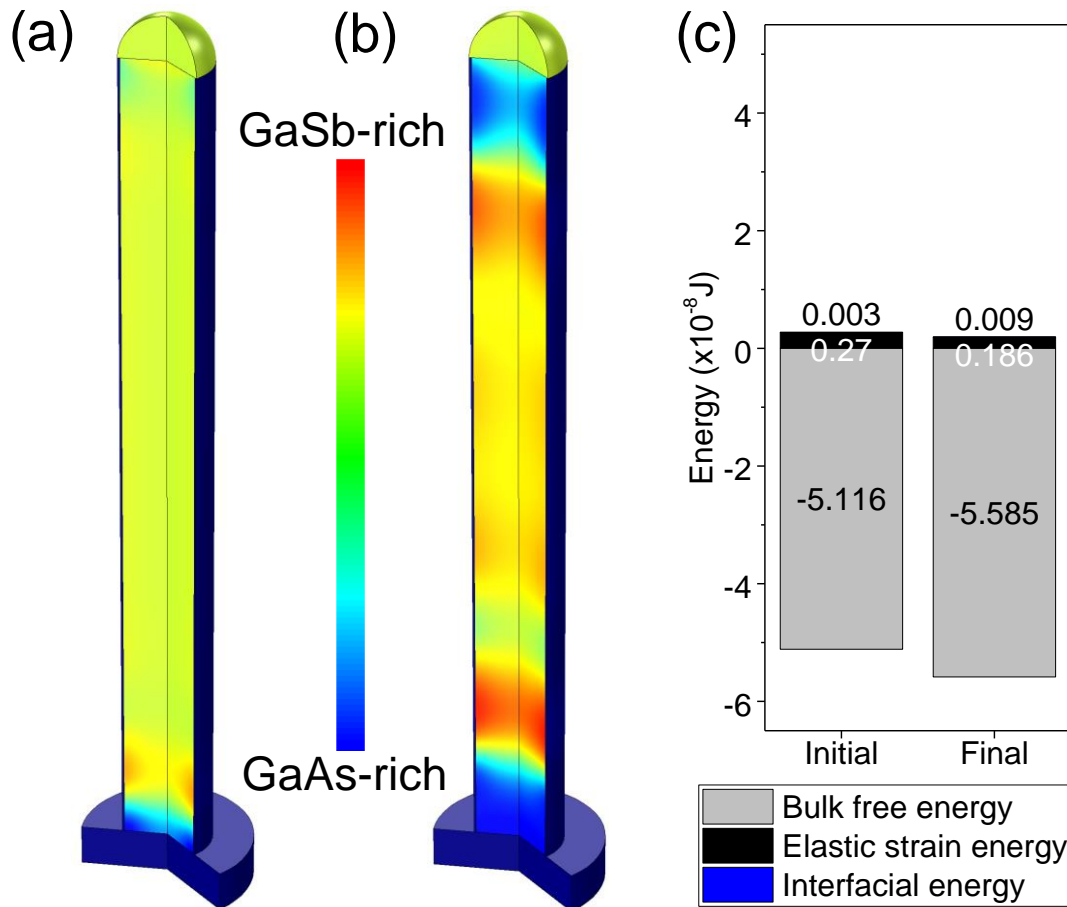


Fig. 5.3 Composition of GaAsSb alloy core-shell nanowire with a GaAs thin shell after annealing for a) 7×10^4 s and b) 5×10^5 s. Separated phases are GaSb-rich phase (red) and GaAs-rich phase (blue). c) Contributions of different energy components to the total energy before annealing and after annealing for 5×10^5 s.

I have shown that a thin shell around the core of a nanowire delays the phase separation. To explore whether such phase separation can be entirely suppressed I consider other geometries of the core-shell nanowire. In particular, it has been shown theoretically that stress and strain in the core increase when the shell thickness increases [12]. Here, I choose the shell thickness to be 5 nm as an example that illustrates my point. Similarly as in the thin shell model, GaAs is chosen as

the shell and therefore the core is under the state of a compressive strain. After annealing at the same temperature of 650 °C as in the case of no-shell and thin-shell nanowires and for the same total amount of time ($t = 5 \times 10^5$ s), I observe that LCM no longer develops (Fig. 5.4a). Although some phase separation is observed near the core-substrate and core-cap interface, the phase separation after 5×10^5 s has been reduced to about 16% which is substantially smaller than phase separation in the core-only nanowire (93%) and the thin-shell nanowire (90%) after the same annealing time. I observe a very small change in the ratio of the elastic strain energy to the bulk free energy during annealing (Fig. 5.4c). During annealing time, the total energy changes by less than 0.5%.

So far I discussed the effects of thin (0.5 nm) and thick (5 nm) shells on delay/suppression of the phase separation. In order to have a better understanding of the role of the shell thickness in phase separation, in Fig. 5.4d I report the results of annealing simulations for nanowires with a range of shell thicknesses. I found that in general when the shell thickness increases, the phase separation is suppressed but it does not decay all the way to zero. The reason for this behavior is that while the presence of the shell suppresses phase separation that starts from the core/shell interface, the phase separation can still be initiated at both ends of the nanowire. To demonstrate the effect of the nanowire ends on phase separation, in Fig. 5.4d I show the amount of phase separation in different sections of the nanowire. For instance, by removing 30% of the nanowire length, phase separation in the remaining 70% of the nanowire approaches 6% for a 10 nm shell. This suppression of phase separation in the mid-section of the nanowire can be attributed to the increase of the strain energy cost associated with lattice mismatch between the phase-separated core and the shell. This energy term increases as the shell thickness increases. The only other contribution to the cost in energy is the strain energy arising from the lattice mismatch between the layers in the phase-separated core, but this energy contribution is not expected to depend on the thickness of the shell and, as shown in Fig. 5.2, it is quite small. These results demonstrate

that geometry and strain can be exploited in nanowire heterostructures as means for suppressing phase separation in an alloy with a thermodynamic driving force to separate at relatively high annealing temperatures. All the results in this paper have been generated for nanowires with diameters equal to 20 nm because of the computational efficiency. However, for selected cases I have also performed simulation for thinner (10 nm in diameter) and thicker (40 nm in diameter) nanowires and I have found the results to be qualitatively the same as in the case of the 20 nm nanowire. For instance, the effect of shell thickness on suppression of phase separation (similar to that shown in Fig. 5.4d) has been observed both in thinner and in thicker nanowires.

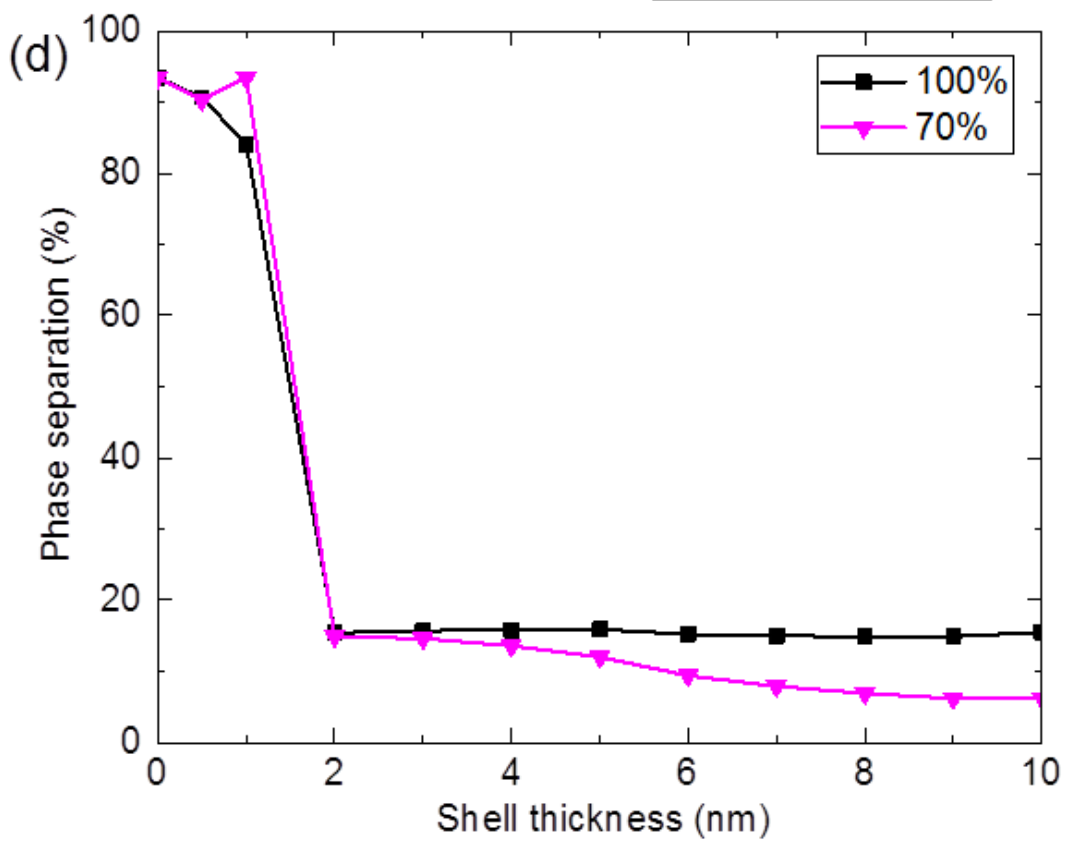
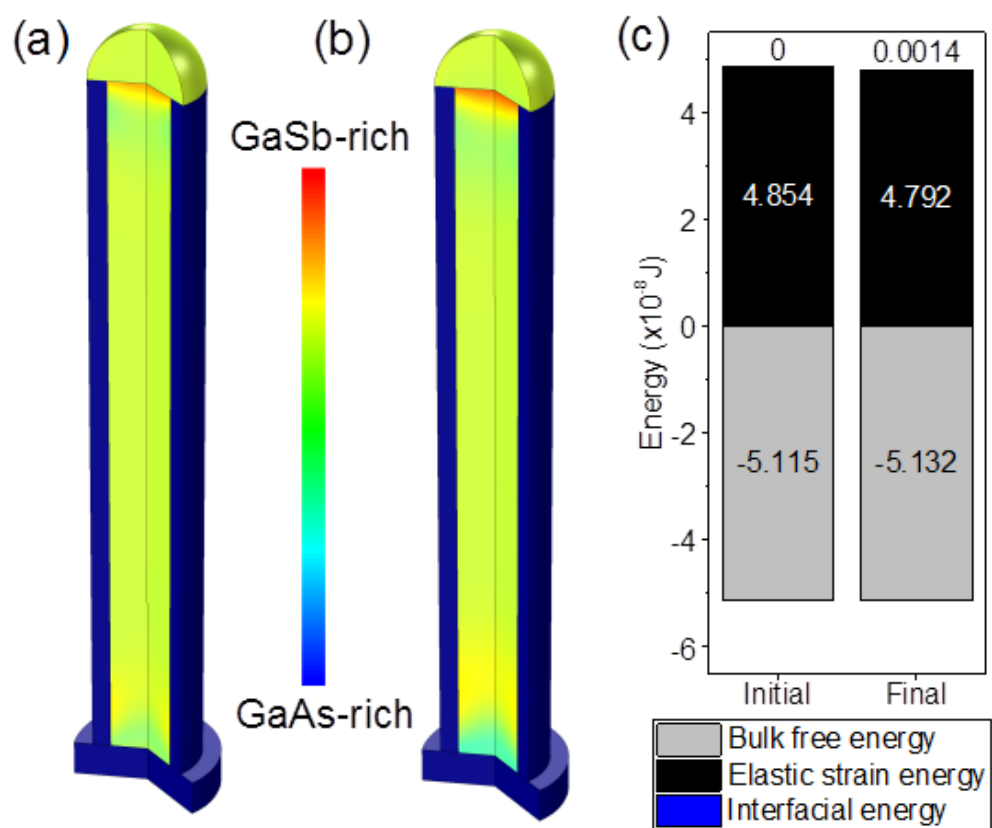


Fig. 5.4 Composition of GaAsSb core-shell nanowire with GaAs thick shell after annealing for a) 7×10^4 s and b) 5×10^5 s. Separated phases are GaSb-rich phase (red) and GaAs-rich phase (blue). c) Contribution of different energy components before annealing and after annealing for 5×10^5 s. d) Effect of shell thickness on suppression of phase separation. The thicker the shell, the lower the phase separation.

Up until now I have considered the effects of a compressive strain imposed by the GaAs shell (GaAs has -3.13% misfit strain with the $\text{GaAs}_{0.6}\text{Sb}_{0.4}$ core before annealing). It is interesting to investigate the effect of misfit strain between core and shell on phase separation in the core. For this reason I model high temperature annealing in a nanowire with shells made of GaSb (+4.69% misfit strain with $\text{GaAs}_{0.6}\text{Sb}_{0.4}$ core before annealing), $\text{GaAs}_{0.28}\text{Sb}_{0.73}$ (+2.58% misfit strain with the $\text{GaAs}_{0.6}\text{Sb}_{0.4}$ core before annealing), $\text{GaAs}_{0.6}\text{Sb}_{0.4}$ (lattice matched with the GaAsSb core before annealing) and $\text{GaAs}_{0.922}\text{Sb}_{0.078}$ (-2.53% misfit strain with the $\text{GaAs}_{0.6}\text{Sb}_{0.4}$ core before annealing). Comparison of the amount of phase separation under compressive, no misfit strain, and tensile strain during the same period of annealing (5×10^5 s) is shown in Fig. 5.5a. My results show that compressive strain suppresses the phase separation more than tensile strain. However for a case where there is a compressive misfit strain between core and shell (-2.53%), the model predicts that the phase separation is minimized. The high cost of strain energy between separated phases and the compressive $\text{GaAs}_{0.922}\text{Sb}_{0.078}$ shell compared to low gain in bulk free energy during phase separation is the reason for the suppression of such separation. Although the strain energy cost due to the lattice mismatch between the core and the shell cannot be easily isolated in my simulations, it must be lower when the core is under tensile stress (GaSb and $\text{GaAs}_{0.28}\text{Sb}_{0.73}$ shells) than when it is under compression (GaAs and $\text{GaAs}_{0.922}\text{Sb}_{0.078}$ shell) or no strain ($\text{GaAs}_{0.6}\text{Sb}_{0.4}$) since more phase separation has been observed in these cases. In general, the exact amount of elastic strain energy arising from lattice mismatch between the core and the shell will

depend on the specific thermodynamic phases to which the multicomponent alloy separates, on their lattice parameters and elastic constants, as well as on the properties of the shell.

Finally, I have investigated the effect of intermixing between the core and the shell on suppression of phase separation in the core. In Fig. 5.5b I compare the effect of shell thickness on phase separation of 5 nm GaAs shells with and without intermixing between the core and the shell after annealing for 5×10^5 s (material properties such as elastic constants, free energies, and diffusivities are kept constant). Similarly as in the case of when no intermixing is allowed, phase separation is significantly suppressed. However, the suppression of phase separation is less pronounced when intermixing is allowed. The effect of shell thickness on phase separation in the two cases is similar when the shell thickness is small; in this regime phase separation decreases with an increasing shell thickness. When the shell thickness is sufficiently large (here larger than 3 nm), phase separation saturates for the no-intermixing case (due to the end effects of a nanowire as discussed earlier) and it increases slightly with shell thickness for the case when intermixing is allowed. The reason for the latter trend is that strain energy in the core-shell structure increases as a function of the shell thickness and intermixing can relax this strain energy at the cost of increasing the bulk free energy in both the core and the shell. One should note that the intermixing occurs only in a relatively small fraction of the nanowire at the interface between the core and the shell (this intermixed region has the thickness of 2.0-2.5 nm).

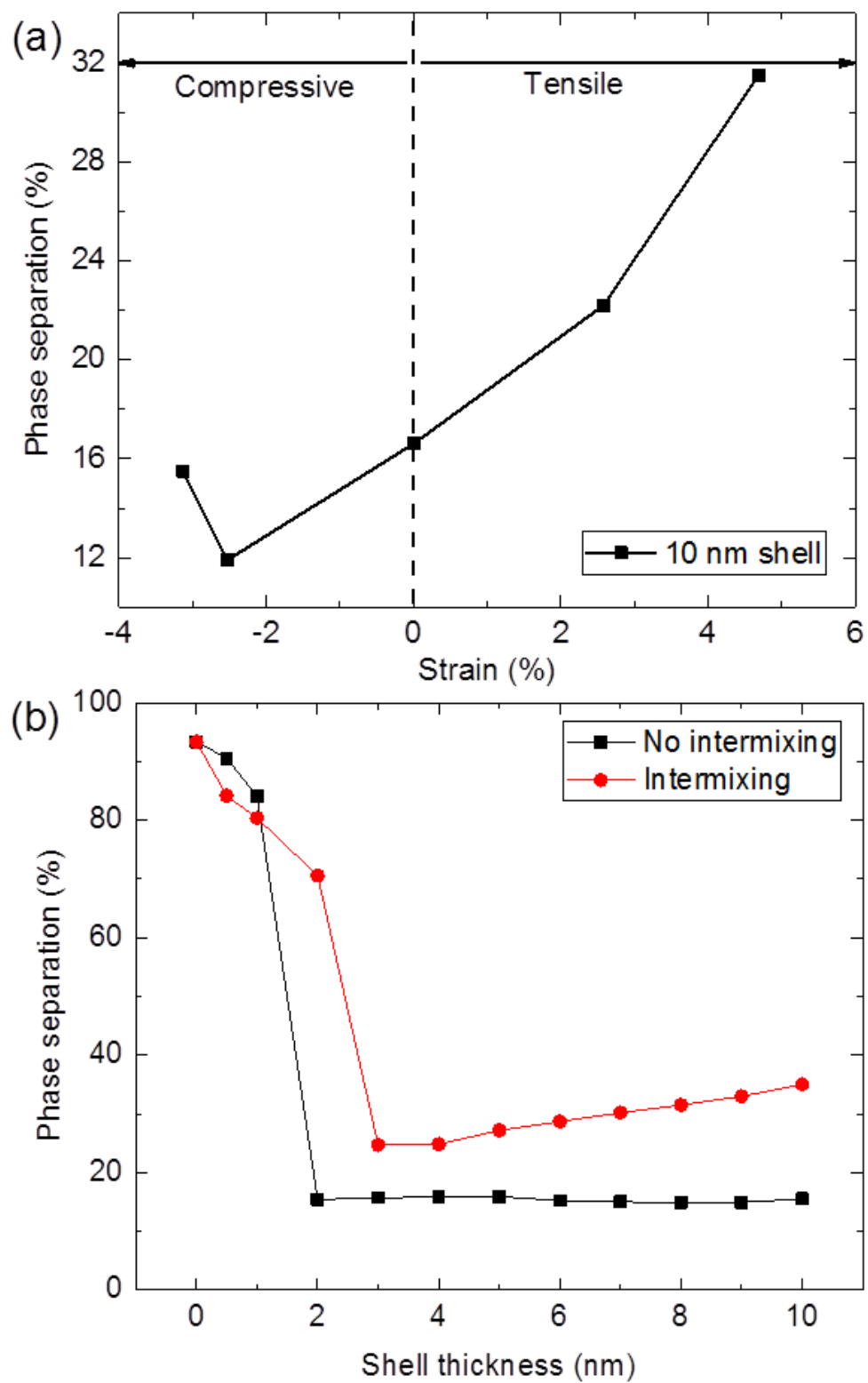


Fig. 5.5 a) Effect of misfit strain between the core and the shell on phase separation in the core. Compressive strain suppresses phase separation more than tensile strain. Maximum suppression of phase separation happens for -2.53% misfit strain. b) Comparison between the effect of shell thickness on phase separation with and without intermixing allowed between the core and the shell. Intermixing increases the amount of phase separation taking place in the core when shells are sufficiently thick, but even in that case the shell is still able to suppress a significant amount of phase separation.

5.5 Summary and conclusions

I demonstrated that during annealing, a core-only nanowire develops surface-induced compositional modulations that take the form of axial heterostructures. Including a shell around the core-nanowire controls phase separation by two mechanisms. The first mechanism involves kinetics where phase separation is suppressed by removing surface diffusion as a pathway for mass transport. The second mechanism involves thermodynamics where the thicker the shell, the higher the elastic energy cost associated with lattice mismatch between the separated phases of the core and the shell. Both lattice matched and lattice mismatched shells suppress phase separation in the core. However, the effect is not necessarily symmetric and depends on the difference between lattice constants on the phases formed in the core during phase separation and the material of the shell.

5.6 References

- [1] R. X. Yan, D. Gargas, and P. D. Yang, *Nat Photonics* **3**, 569 (2009).
- [2] X. F. Duan, Y. Huang, Y. Cui, J. F. Wang, and C. M. Lieber, *Nature* **409**, 66 (2001).
- [3] X. F. Duan, C. M. Niu, V. Sahi, J. Chen, J. W. Parce, S. Empedocles, and J. L. Goldman, *Nature* **425**, 274 (2003).
- [4] M. C. McAlpine, H. Ahmad, D. W. Wang, and J. R. Heath, *Nat Mater* **6**, 379 (2007).
- [5] Q. Gao, H. H. Tan, H. E. Jackson, L. M. Smith, J. M. Yarrison-Rice, J. Zou, and C. Jagadish, *Semicond. Sci. Technol.* **26**, 014035 (2011).
- [6] Y. N. Guo *et al.*, *Nano Lett.* **13**, 643 (2013).
- [7] C. A. Wang, *J. Electron. Mater.* **29**, 112 (2000).
- [8] E. Luna, M. Wu, J. Puustinen, M. Guina, and A. Trampert, *J. Appl. Phys.* **117**, 185302 (2015).
- [9] K. C. Hsieh, K. Y. Hsieh, Y. L. Hwang, T. Zhang, and R. M. Kolbas, *Appl. Phys. Lett.* **68**, 1790 (1996).
- [10] M. Tang and A. Karma, *Phys. Rev. Lett.* **108**, 265701 (2012).
- [11] M. Arjmand, J. Deng, N. Swaminathan, D. Morgan, and I. Szlufarska, *J. Appl. Phys.* **116**, 114313 (2014).
- [12] Y. Liang, W. D. Nix, P. B. Griffin, and J. D. Plummer, *J. Appl. Phys.* **97**, 043519 (2005).
- [13] O. Salehzadeh, K. L. Kavanagh, and S. P. Watkins, *J. Appl. Phys.* **113**, 134309 (2013).
- [14] K. L. Kavanagh, *Semicond. Sci. Technol.* **25**, 024006 (2010).
- [15] L. J. Lauhon, M. S. Gudiksen, C. L. Wang, and C. M. Lieber, *Nature* **420**, 57 (2002).
- [16] K. M. Varahramyan, D. Ferrer, E. Tutuc, and S. K. Banerjee, *Appl. Phys. Lett.* **95**, 033101 (2009).
- [17] L. Chen, W. Lu, and C. M. Lieber, in *Semiconductor Nanowires: From Next-Generation Electronics to Sustainable Energy* (The Royal Society of Chemistry, 2015), pp. 1.

- [18] H. L. Zhou, T. B. Hoang, D. L. Dheeraj, A. T. J. van Helvoort, L. Liu, J. C. Harmand, B. O. Fimland, and H. Weman, *Nanotechnology* **20**, 415701 (2009).
- [19] D. W. Wang, R. Tu, L. Zhang, and H. J. Dai, *Angew Chem Int Edit* **44**, 2925 (2005).
- [20] O. M. Khreis, K. P. Homewood, W. P. Gillin, and K. E. Singer, *J. Appl. Phys.* **84**, 4017 (1998).
- [21] K. Ishida, T. Shumiya, T. Nomura, H. Ohtani, and T. Nishizawa, *J Less-Common Met* **142**, 135 (1988).
- [22] A. Boyne, M. D. Rauscher, S. A. Dregia, and Y. Wang, *Scripta Mater.* **64**, 705 (2011).
- [23] N. Moelans, B. Blanpain, and P. Wollants, *Computer Coupling of Phase Diagrams and Thermochemistry* **32**, 268 (2008).
- [24] Y. Tu and J. Tersoff, *Phys. Rev. Lett.* **98**, 096103 (2007).
- [25] W. F. Boyle and R. J. Sladek, *Phys Rev B* **11**, 2933 (1975).
- [26] E. Placidi *et al.*, in *Self-Assembly of Nanostructures: The INFN Lectures*, edited by Springer (2012).
- [27] G. Guisbiers, M. Wautelet, and L. Buchaillot, *Phys Rev B* **79**, 155426 (2009).
- [28] R. T. Hao, Y. Q. Xu, Z. Q. Zhou, Z. W. Ren, H. Q. Ni, Z. H. He, and Z. C. Niu, *J Phys D Appl Phys* **40**, 1080 (2007).
- [29] J. W. Cahn and J. E. Hilliard, *J. Chem. Phys.* **28**, 258 (1958).

Chapter 6 Analytical elastoplastic analysis of heteroepitaxial core-shell nanowires

6.1 Abstract

Semiconductor nanowires, grown heteroepitaxially, have many unique properties compared to heteroepitaxial thin films: e.g., the possibility of lateral relaxation, high surface to volume ratio and lower strain energy. While the onset of plastic deformation in thin films has been studied extensively, much less is understood about this phenomenon in the nanowire geometry. Here, I report results of a continuum analytical model that predicts not only the onset of plastic deformation, but also evolution of stress and strain fields beyond initial yield. This is the first analytical elastoplastic study of heteroepitaxial core-shell nanowires. The analytical model is validated via finite element simulations. To illustrate trends predicted by the model I chose the InAs-GaAs core-shell system as an example. My results show that the thickness of the plastically deformed region is proportional to the core radius and it has a non-monotonic dependence on the shell thickness. I find that there is a critical ratio, χ , of shell thickness to core radius that maximizes the thickness of the elastoplastic region. This critical ratio is independent of geometry and only depends on material properties such as elastic moduli and yield strength of the heterostructure.

6.2 Introduction

Semiconductor heterostructures have attracted much attention in the past few decades because one can tailor their electronic properties, such as electron and carrier mobility, by tuning their strain [1,2]. Strain in heterostructures is mainly caused by the difference between the lattice parameter of the film and of the substrate; this is called the misfit strain. The strain energy associated with the misfit strain can be relaxed via different mechanisms. One relaxation method involves bending and deforming the substrate [3]. This mechanism is only effective when the substrate is sufficiently thin and compliant. Other methods found to relax strain in a multi-

component semiconductor can involve (i) phase separation [4,5], (ii) transition from 2D to 3D structure by forming undulations (islands) at the surface, [6,7] and (iii) plastic deformation (i.e., nucleation of misfit dislocations).

Formation of misfit dislocations is highly undesirable in the fabrication of highly mismatched heterostructures since these defects significantly deteriorate electronic and optoelectronic properties of semiconductor heterostructures such as the electron field-effect mobility [8]. To eliminate or at least to partially reduce defect densities, many authors have focused on different approaches to reduce the strain energy in the system [3,9,10]. One of the methods that has been extensively studied is the use of compliant substrates that accommodate the high misfit strain between the film and the substrate [3]. Although this method has been shown to be promising, it is not always possible to use sufficiently thin or compliant substrates in practice. Another method to reduce the density of defects in a heterostructure is by changing the geometry. Studies have shown that heterostructures in the form of nanowires have less strain energy than epitaxial thin films [9,10]. The advantageous properties of nanowires have led to fabrication of nanowire-based devices such as lasers [11], light emitting diodes [11,12], transistors [13] and sensors [14]. Lateral relaxation of strains [15,16] with respect to the substrate and partial relaxation of strain in core-shell structures due to nanowire geometry allow reduction in the density of structural defects such as dislocations. Nonetheless, when the misfit strain in nanowires is high enough, defects can still form and the structure deforms plastically. These defects have been observed in experiments [17,18] and theoretical studies have provided new insights into how elastic stresses can lead to formation of these defects at the onset of plasticity [9,10,17,18]. It remains an open question how the stress and strain fields are affected in the elastoplastic regime, beyond the onset of yield.

A number of theoretical studies have been dedicated to understanding the strain and stress fields in nanowires before and at the onset of defect formation. For instance, Liang *et al.* [10] reported an analytical model of the critical thickness of the shell at which defects begin to form.

The authors assumed isotropic elastic properties for both the core and the shell material and they used a thick-walled cylinder theory to determine the stress and strain field in the structure. Another approach was reported by Trammell *et al.* [9], who developed analytical models for heterostructures in the form of thin films and nanowires. The authors showed that the strain energy per interfacial area of core and shell is lower in the nanowire structure than in the thin film geometry. Zhao *et al.* [19] investigated the effect of material properties and surface stress on the formation of an edge dislocation in core-shell nanowires. They showed that by increasing the ratio of shear moduli of the core and the shell, the critical film thickness first decreases and then increases again. In addition, the authors found that a negative (i.e., compressive) surface stress could decrease the formation energy of an edge misfit dislocation, making it easier for the defect to form. Gutkin *et al.* [20] used the theory of elasticity to investigate the elastic behavior of an edge dislocation inside the core of a core-shell structure and found the equilibrium position for the dislocation. They also studied the effect of core radius and shell thickness on forces acting on the dislocation. However, none of the above studies considered the evolution of the strain and stress fields in these heterostructures beyond initial yield.

In this paper I derive a continuum analytical model of plastic deformation in highly mismatched core-shell nanowires. I choose InAs/GaAs core-shell nanowire as a specific example for parameters of the model, although there is nothing in the formulation of the model that limits it to a given material. In my formalism, I have included elastic constants and the presence of the misfit strain, and the diameters of the core and the shell are treated as parameters. I assume the Tresca yield criterion with the associated flow rule and a perfectly plastic material (with no work hardening). In addition, I have developed a finite element (FE) model to confirm the predictions of the analytical model. In the FE simulations, I have used both Tresca and Von Mises yield criteria with the associated flow rules. Two of the key questions I answer in this study are how

strain and stress fields evolve due to plastic deformation and how plastic strain can be minimized by designing the geometry of the nanowire.

6.3 Model

Fig. 6.1a and Fig. 6.1b show a schematic view of the core-shell nanowire cross-section.

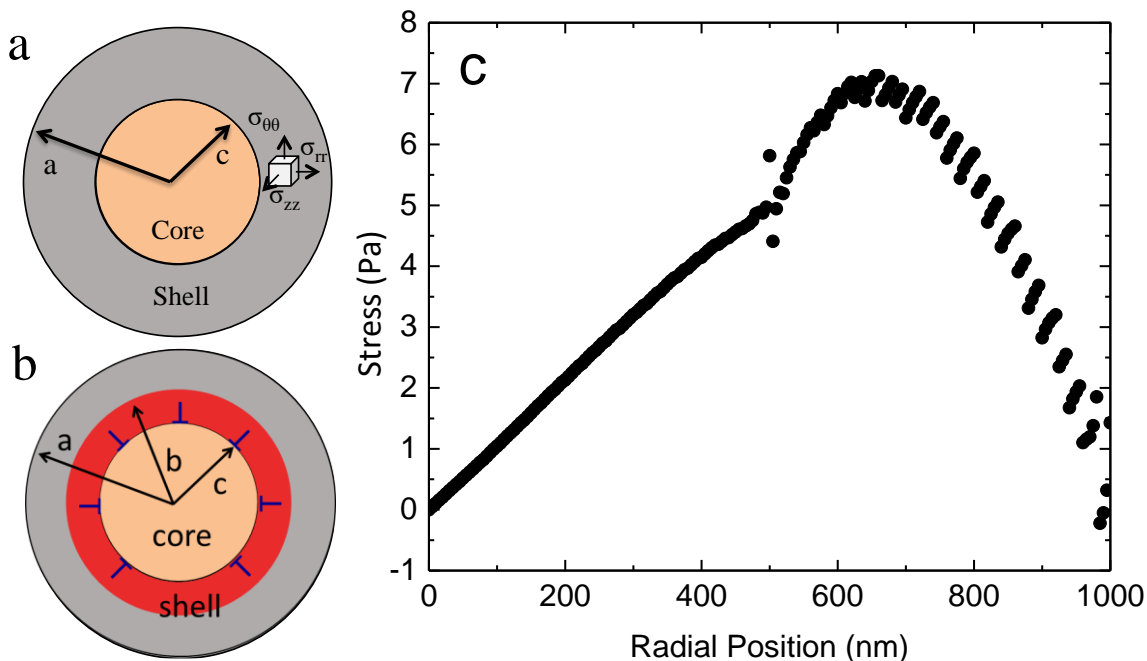


Fig. 6.1 (Color online) Schematic view of a nanowire cross-section: a) Before yield: due to symmetry, only normal components of stress (σ_{rr} , $\sigma_{\theta\theta}$, and σ_{zz}) are nonzero. b) After yield: under high misfit strain, plastic deformation takes place in the structure. Elastoplastic region in the shell is shown in red while misfit dislocations at the core-shell interface are shown in dark blue. c) Shear stress S_{rz} as a function of radial position. Zero on the horizontal axis is defined at the center of the nanowire.

In order to find an analytical solution for strain and stress fields in this geometry, I use the elastoplastic governing equations for a homogeneous isotropic/cubic linear elastic-ideally plastic

core-shell nanowire in cylindrical coordinates. My analysis proceeds as follows: I employ a cylindrical coordinate system with polar coordinates r, θ centered at the wire core and z directed along its axis. The problem's axisymmetry requires that the stress components $\sigma_{r\theta}$ and $\sigma_{\theta z}$ are identically zero, and that stresses, strains and displacements are independent of θ . A typical wire is long compared to its radius; thus, neglecting end effects, I assume all stresses and strains are independent of z . My numerical FE simulations have shown that, in all cases, σ_{rz} , and while nonzero in general due to the axial core-shell misfit, is at least nine orders of magnitude smaller than all other nonzero stresses (Fig. 6.1c); therefore, I neglect it in my analytical model. Thus, the only nonzero stresses are the three normal ones, $\sigma_{rr}, \sigma_{\theta\theta}, \sigma_{zz}$, and these depend only on r . Finally, I assume ε_{zz} to be independent of r in the core and the shell, although one should note that in general ε_{zz} is not continuous across the core-shell boundary.

With the above considerations, the three-dimensional governing equations can be simplified as follows:

- i. Equilibrium – satisfied in all regions

$$\frac{d\sigma_{rr}}{dr} + \frac{\sigma_{rr} - \sigma_{\theta\theta}}{r} = 0. \quad 6-1$$

- ii. Strain-displacement – satisfied in all regions

$$\varepsilon_{rr} = \frac{\partial u_r}{\partial r}, \varepsilon_{\theta\theta} = \frac{u_r}{r}, \varepsilon_{zz} = \frac{\partial u_z}{\partial z} . \quad 6-2$$

- iii. Stress-strain equations – satisfied in all regions

$$\varepsilon^e = \frac{1+\nu}{E} \boldsymbol{\sigma} - \frac{\nu}{E} \text{Itr} \boldsymbol{\sigma}, \quad 6-3$$

where E is Young's modulus and ν is Poisson's ratio, and $\boldsymbol{\varepsilon}^e$ is the elastic part of the strain tensor, which is equal to the difference between the total strain and the plastic strain:

$$\varepsilon^e = \varepsilon - \varepsilon^p. \quad 6-4$$

E , ν , μ are defined in terms of elastic constants C_{11} , C_{12} and C_{44} as follows:

$$E = \frac{(C_{11}^2 + C_{11}C_{12} - 2C_{12}^2)}{(C_{11} + C_{12})}, \quad 6-5$$

$$\nu = \frac{C_{12}}{(C_{11} + C_{12})}, \quad 6-6$$

$$\mu = C_{44}. \quad 6-7$$

Equation (6-3) assumes isotropic elasticity, that is $C_{44} = (C_{11} - C_{12})/2$. This choice is made to simplify the analytical derivation. However, it is also justified by the fact that $\sigma_{r\theta}$ and $\sigma_{\theta z}$ are zero and σ_{rz} is negligible, and therefore the value of the elastic constant C_{44} does not impact my solution. This fact has been confirmed by performing FE simulations with isotropic and cubic elastic constants, where I found that all the components of the stress field are the same.

iv. Yield condition

In yielded regions, I adopt the Tresca yield criterion. According to this criterion, yield occurs when the maximum shear stress attains a critical value, which is equal to half the uniaxial yield strength σ_Y . Yielding is found to occur only in the shell. Since the normal cylindrical stress components are the principal stresses and the maximum and minimum stresses are $\sigma_{\theta\theta}$ and σ_{rr} , respectively, the Tresca condition can be written as

$$F(\boldsymbol{\sigma}) = \sigma_{\theta\theta} - \sigma_{rr} = \sigma_Y. \quad 6-8$$

I assume proportional stressing everywhere, which assumption has been validated by my numerical FE simulations. Consequently, the flow rule has the following form derived from the deformation-theory plasticity

$$\boldsymbol{\varepsilon}^p = \Lambda \frac{\partial F(\boldsymbol{\sigma})}{\partial \boldsymbol{\sigma}}. \quad 6-9$$

With the above considerations and governing equations I am now ready to derive the solution forms for the displacement field u_r . In purely elastic regions, $\boldsymbol{\varepsilon}^e = \boldsymbol{\varepsilon}$. By substituting Eq. (6-2) into Eq. (6-3) and then into Eq. (6-1), one can find the following governing equation for u_r :

$$\frac{d^2 u_r}{dr^2} + \frac{1}{r} \frac{du_r}{dr} - \frac{u_r}{r^2} = 0. \quad 6-10$$

The general solution to Eq. (6-10) is

$$u_r = Ar + B \frac{1}{r} \quad 6-11$$

where A and B arbitrary constants. This is the general form u_r can take in the shell elastic region. In the elastic core, I must take $B = 0$ to satisfy finite displacement at $r = 0$, and of course A is different from that in the shell.

In the region of the shell that yielded plastically, the stress governing equations are given by Eq. (6-1) and Eq. (6-8). By plugging in Eq. (6-8) into Eq. (6-1), one can find the general form of the stress field

$$\sigma_{rr} = \sigma_Y \ln r + C, \quad 6-12$$

$$\sigma_{\theta\theta} = \sigma_Y + \sigma_{rr}. \quad 6-13$$

where C is an arbitrary constant. Following an analysis by Koiter [21] of an elastic-plastic pressure vessel, I assume plastic incompressibility which means that the volumetric strain is purely elastic. Consequently:

$$\varepsilon_{rr} + \varepsilon_{\theta\theta} + \varepsilon_{zz} = \frac{du_r}{dr} + \frac{u_r}{r} + \varepsilon_{zz} = \frac{1-2\nu}{E} (\sigma_{rr} + \sigma_{\theta\theta} + \sigma_{zz}). \quad 6-14$$

Equations (6-8 - 6-9) show that ε_{zz} is purely elastic and thus one can write it as $\varepsilon_{zz} = [\sigma_{zz} - \nu(\sigma_{rr} + \sigma_{\theta\theta})]/E$. By substituting this equation into Eq. (6-14) I get

$$\frac{1}{r} \frac{d(ru_r)}{dr} = \frac{(1-2\nu)(1+\nu)}{E} (\sigma_{rr} + \sigma_{\theta\theta}) - 2\nu\varepsilon_{zz}. \quad 6-15$$

Using Eqs. (6-12 - 6-13), one can write Eq. (6-15) as follows

$$\frac{1}{r} \frac{d(ru_r)}{dr} = \frac{(1-2\nu)(1+\nu)}{E} (2\sigma_Y \ln er) - 2\nu\varepsilon_{zz}. \quad 6-16$$

Multiplying Eq. (6-16) by r , integrating with respect to r , and then dividing by r shows that in the yielded shell region u_r has the form

$$u_r = C_1 r + \frac{C_2}{r} + C_3 r \ln r, \quad 6-17$$

where C_1 , C_2 and C_3 are constants. Thus, the displacement field in the elastic core (superscript “c”), the plastic shell region (superscript “sp”) and the elastic shell region (superscript “se”) will be as follows:

$$u_r^c = A_c r, \quad 6-18$$

$$u_z^c = E_c z, \quad 6-19$$

$$u_r^{sp} = A_{sp} r + \frac{B_{sp}}{r} + D_{sp} r \ln r, \quad 6-20$$

$$u_z^{sp} = E_{sp} z, \quad 6-21$$

$$u_r^{se} = A_{se} r + \frac{B_{se}}{r}, \quad 6-22$$

$$u_z^{se} = E_{se} z. \quad 6-23$$

Using Eqs. (6-1 - 6-9), one can find the general form of stress and strain fields both in the elastic and elastoplastic regions of the nanowire. Generally, there are two different approaches to solve for the strain and stress fields in heteroepitaxial nanowires. One approach is to define the misfit strain between core and shell and then apply it as a boundary condition to the displacement field [10]. Another approach is to define an arbitrary reference state and then to define the misfit strain with respect to the reference state [9]. The strain and stress fields are expressed in terms of ten unknowns: the nine constants appearing in Eqs. (6-18 – 6-23), A_c , E_c , A_{sp} , B_{sp} , D_{sp} , E_{sp} , A_{se} , B_{se} ,

E_{se} , and b , which is the radius of the elastoplastic zone. To solve for these unknowns, I need 10 equations, which are as follows

- i. Along the axial direction, the gap (equal to the difference in displacements) between the core and the shell (in stress-free state) depends on the misfit strain as

$$u_z^c|_{r=c} - u_z^{sp}|_{r=c} = (z \cdot e_{zz}^*)|_{r=c}. \quad 6-24$$

In the above equation \mathbf{e}^* is the eigenstrain tensor associated with the misfit strain, which in turn is defined as the difference between lattice parameters of the core and the shell

$$\mathbf{e}^* = \frac{a_{core} - a_{shell}}{a_{shell}} \mathbf{I}, \quad 6-25$$

where \mathbf{I} is the identity matrix.

- ii. The axial displacement field must be continuous across the elastic-plastic boundary

$$u_z^{sp}|_{r=b} = u_z^{se}|_{r=b}. \quad 6-26$$

- iii. In the radial direction, the gap between the core and the shell (in the stress-free state) depends on the misfit strain as

$$u_r^c|_{r=c} - u_r^{sp}|_{r=c} = (r \cdot e_{rr}^*)|_{r=c}. \quad 6-27$$

- iv. The radial displacement field must be continuous across the elastic-plastic boundary

$$u_r^{sp}|_{r=b} = u_r^{se}|_{r=b}. \quad 6-28$$

- v. The net force on the surface perpendicular to the z direction is zero

$$\int_0^{2\pi} \int_0^c \sigma_{zz}^c r \, dr d\theta + \int_0^{2\pi} \int_c^b \sigma_{zz}^{sp} r \, dr d\theta + \int_0^{2\pi} \int_b^c \sigma_{zz}^{se} r \, dr d\theta = 0, \quad 6-29$$

where σ_{zz} is the axial stress.

- vi. At the core-shell interface, the radial component of stress σ_{rr} must be continuous

$$\sigma_{rr}^c|_{r=c} = \sigma_{rr}^{sp}|_{r=c}. \quad 6-30$$

vii. The radial component of stress must be continuous across the elastic-plastic boundary

$$\sigma_{rr}^{sp} |_{r=b} = \sigma_{rr}^{se} |_{r=b}. \quad 6-31$$

viii. The traction vector is zero at the surface

$$\sigma_{rr}^{se} |_{r=a} = 0. \quad 6-32$$

ix. The Tresca yield criterion is enforced at the elastic-plastic boundary (and everywhere in the yielded region)

$$\sigma_{\theta\theta}^{se} |_{r=b} - \sigma_{rr}^{se} |_{r=b} = \sigma_Y, \quad 6-33$$

where $\sigma_{\theta\theta}$ is the tangential (hoop) stress.

x. The radial equilibrium equation is already satisfied in the core and in the elastic part of the shell but it must also be satisfied in the yielded region

$$\frac{d\sigma_{rr}^{sp}}{dr} + \frac{\sigma_{rr}^{sp} - \sigma_{\theta\theta}^{sp}}{r} = 0. \quad 6-34$$

By solving the above system of equations, I find the unknown coefficients in terms of material properties and geometry. Then I employ these coefficients in Eqs. (6-10) and substitute these into the governing equations (Eqs. 6-1 - 6-9) to find an analytical solution for stress and strain fields. The solution for the strain components is

$$\varepsilon_{rr}^{\alpha} = \frac{du_r^{\alpha}}{dr}, \quad 6-35$$

$$\varepsilon_{\theta\theta}^{\alpha} = \frac{u_r^{\alpha}}{r}, \quad 6-36$$

$$\varepsilon_{zz}^{\alpha} = \frac{du_z^{\alpha}}{dz}, \quad 6-37$$

where “ α ” can be “c”, “sp” or “se”. Assuming proportional loading and using Eq. (6-9), the

plastic strain field $\boldsymbol{\varepsilon}^p$ is found to be

$$\varepsilon_{rr}^p = \frac{-2B_{sp}(C_{11}^s - C_{12}^s) + r^2(C_{11}^s D_{sp} - C_{12}^s D_{sp} + \sigma_Y)}{2r^2(C_{11}^s - C_{12}^s)} = \frac{1}{2} \left(D_{sp} - \frac{2B_{sp}}{r^2} + \frac{(1+\nu^s)\sigma_Y}{E^s} \right), \quad 6-38$$

$$\varepsilon_{\theta\theta}^p = -\frac{1}{2} \left(D_{sp} - \frac{2B_{sp}}{r^2} + \frac{(1+\nu^s)\sigma_Y}{E^s} \right) = -\varepsilon_{rr}^p, \quad 6-39$$

$$\varepsilon_{zz}^p = 0. \quad 6-40$$

here C_{11}^s , C_{12}^s , E^s , and ν^s are components of the stiffness matrix in the shell. Now using Eqs. (6-35 - 6-40) in Eq. (6-4) gives the elastic strain field. Finally I substitute the elastic strain field into Eq. (6-3) to find the stress field in the core, the elastoplastic part of the shell and the elastic part of the shell. These are

$$\sigma_{rr}^\alpha = C_{11}^\alpha e_{rr}^\alpha + C_{12}^\alpha e_{\theta\theta}^\alpha + C_{12}^\alpha e_{zz}^\alpha, \quad 6-41$$

$$\sigma_{\theta\theta}^\alpha = C_{12}^\alpha e_{rr}^\alpha + C_{11}^\alpha e_{\theta\theta}^\alpha + C_{12}^\alpha e_{zz}^\alpha, \quad 6-42$$

$$\sigma_{zz}^\alpha = C_{12}^\alpha e_{rr}^\alpha + C_{12}^\alpha e_{\theta\theta}^\alpha + C_{11}^\alpha e_{zz}^\alpha. \quad 6-43$$

Similarly as in Eq. (6-35 – 6-37), here “ α ” represents “c”, “sp” or “se”. Also, e_{rr}^α , $e_{\theta\theta}^\alpha$, and e_{zz}^α are the radial, the tangential and the axial components of the elastic strain tensor, respectively. This system of equations (Eqs. 6-9 and 6-24 – 6-34) will be solved analytically for the example of InAs and GaAs core-shell nanowire and the results will be discussed in Section 6.4.

After finding the stress and strain fields, one can find the strain energy density W_d as

$$W_d = \int_0^e \sigma_{ij} d\varepsilon_{ij}, \quad 6-44$$

where S_{ij} and e_{ij} are components of the stress and the strain tensors, respectively, and the summation convention is employed for repeated subscripts. The elastic strain energy density W_d^e is

$$W_d^e = \frac{1}{2} \sigma_{ij} e_{ij}^e, \quad 6-45$$

In the elastoplastic region of the shell the strain energy density W_d^P is calculated from

$$W_d^e = \sigma_Y e_{eff}^p. \quad 6-46$$

Here e_{eff}^p is the effective plastic strain

$$e_{eff}^p = \sqrt{\frac{2}{3} \left\{ (e_{rr}^p)^2 + (e_{\theta\theta}^p)^2 + (e_{zz}^p)^2 \right\}}, \quad 6-47$$

where e_{rr}^p , $e_{\theta\theta}^p$ and e_{zz}^p are the radial, the tangential and the axial components of the plastic strain tensor. One can also find the strain energy per interfacial area between the core and the shell (in the units of J/m²). Strain energy per interfacial area W_a^C in the core is given by

$$W_a^c = \frac{W_d^e}{A_i} = \frac{1}{2c} \int_0^c \sigma_{ij} e_{ij}^e r dr, \quad 6-48$$

where $A_i = 2\pi cL$ is the interfacial area between the core and the shell. Here L is the length of the nanowire. Similarly, the plastic strain energy per unit area in the shell W_a^{sp} and the elastic strain energy per unit area in the shell W_a^{se} are defined as

$$W_a^{sp} = \frac{W_d^p}{A_i} = \frac{1}{2c} \int_c^b \sigma_Y e_{eff}^p r dr, \quad 6-49$$

$$W_a^{se} = \frac{W_d^e}{A_i} = \frac{1}{2c} \left[\int_c^b \sigma_{ij} e_{ij}^e r dr + \int_b^a \sigma_{ij} e_{ij}^e r dr \right]. \quad 6-50$$

6.4 Results

I demonstrate validity of the analytical solution by comparing its predictions to results from FE simulations performed on the same material system. The FE model is developed in commercial framework software, COMSOL. The model is axisymmetric due to the symmetry of the nanowire. In the FE model the radius of the core is 500 nm, the thickness of the shell is also 500 nm, and the length of the wire is taken to be 10 μ m. I use a mesh composed of quadratic elements with dimensions of 20 \times 20 nm². Similarly to the analytical model, I employ the Tresca

yield criterion with the associated flow rule for the elastoplastic model. For the purpose of illustration, I use parameters corresponding to InAs as core and GaAs as shell. Material properties for the GaAs and InAs are listed in Table 6.1.

Table 6.1 Elastic constants, yield strength, and lattice mismatch for different InAs and GaAs.

Input parameters	Core (InAs)	Shell (GaAs)
C_{11} (GPa)	83.4 [22]	118.8 [22]
C_{12} (Gpa)	45.4 [22]	53.4 [22]
C_{44} (Gpa)	39.5 [22]	59.6 [22]
Yield strength σ_{Y0} (Gpa)	2.5 [23]	5 [23]
Lattice mismatch (%)	-	6.68

I first validate stress field (Eq. (6-30)) predicted by my analytical model for the case of no plasticity against FE results. In this case, my analytical model reduces to the analytical solutions reported in Refs. [9,10]. I then apply my analytical model to study plastic behavior. I begin with the purely elastic case and in Fig. 6.2a I plot different components of stress along the radial direction of the nanowire. One can see that the numerical results match very well with the analytical predictions. σ_{rr} is continuous across the interface whereas both $\sigma_{\theta\theta}$ and σ_{zz} have jumps across the interface. In Fig. 6.2b, I compare the Von Mises and Tresca effective stresses to the yield strength of the material. This graph shows that there is a region in the shell near the core/shell interface where the effective stress is higher (by up to 100%) than the yield strength of the material and therefore the analytical solution for the stress and the strain fields derived assuming elastic material models [9,10] is not valid in this regime. Therefore in order to

accurately determine stresses and strains in the shell, one needs to consider elasto-plastic constitutive equations for deformation.

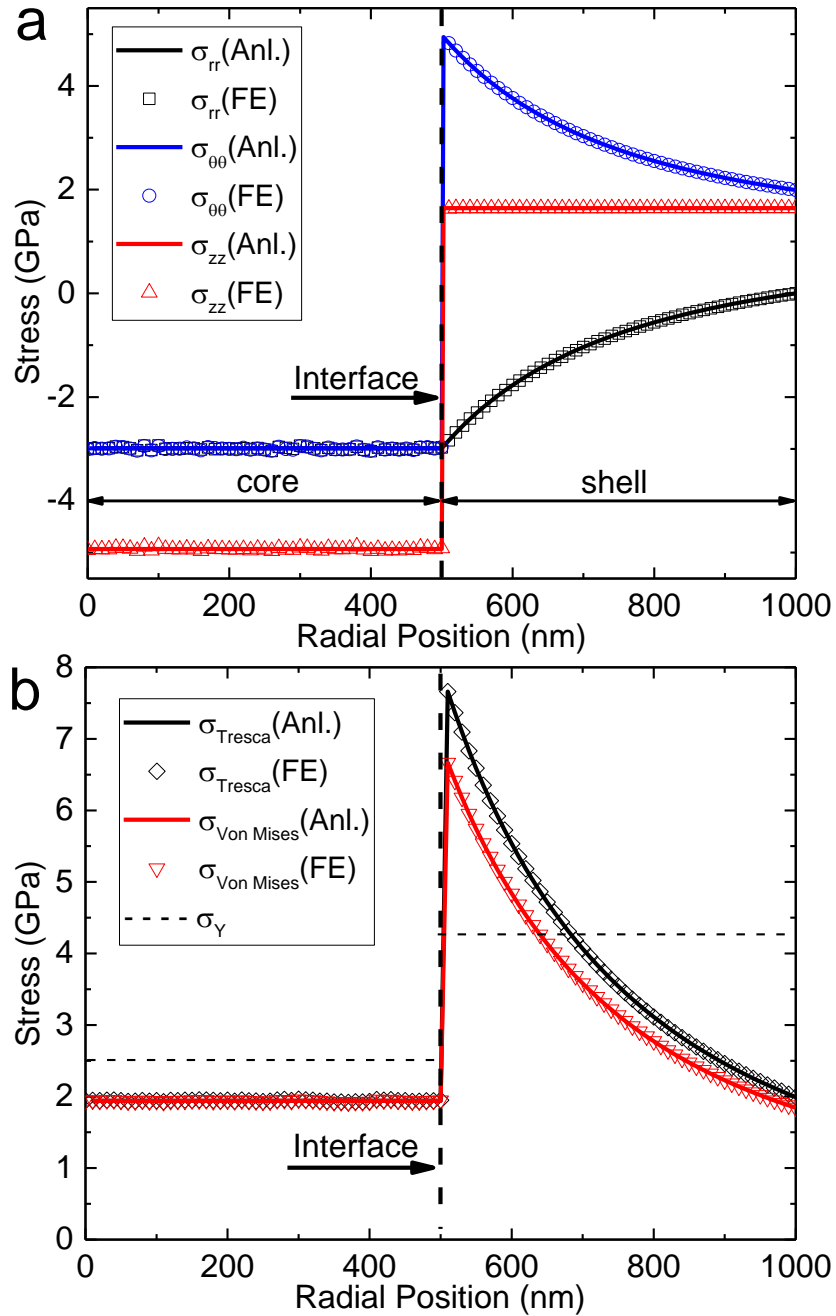


Fig. 6.2 (Color online) Comparison of analytical solution (no plasticity) with FE simulations. a) Radial σ_{rr} , circumferential $\sigma_{\theta\theta}$ and axial σ_{zz} components of stress. b) Tresca and Von Mises

effective stress compared with the yield strength. Zero radial position corresponds to the center of the core and 1000 nm corresponds to the surface of the shell.

Next, I test the analytical results for the elastoplastic model against results of the FE simulations. As shown in Fig. 6.3, there is a very good agreement between plastic stresses and strains in the core-shell structure. Fig. 6.3a shows that in the shell near the interface, circumferential ($\sigma_{\theta\theta}$) and axial (σ_{zz}) components of stress are partially relaxed as compared to the stress components in only elastic case (Fig. 6.2a). In contrast, plastic deformation does not have a significant effect on the radial (σ_{rr}) component of stress. The region where stress is partially relaxed and the plastic strain is non-zero will be referred to as the elastoplastic region. Elastoplastic region is labeled in Fig. 6.3a as *b-c* and in Fig. 6.3b as shell-elastoplastic. Variation of plastic strain with the radius of the nanowire is shown in Fig. 6.3b. No plastic deformation takes place in the core since the effective stress in the core is lower than the yield strength of the material. Inside the shell, plastic deformation occurs in a region near the core-shell interface where the effective stress is higher than yield strength. Plastic strain vanishes at some distance from the core-shell interface.

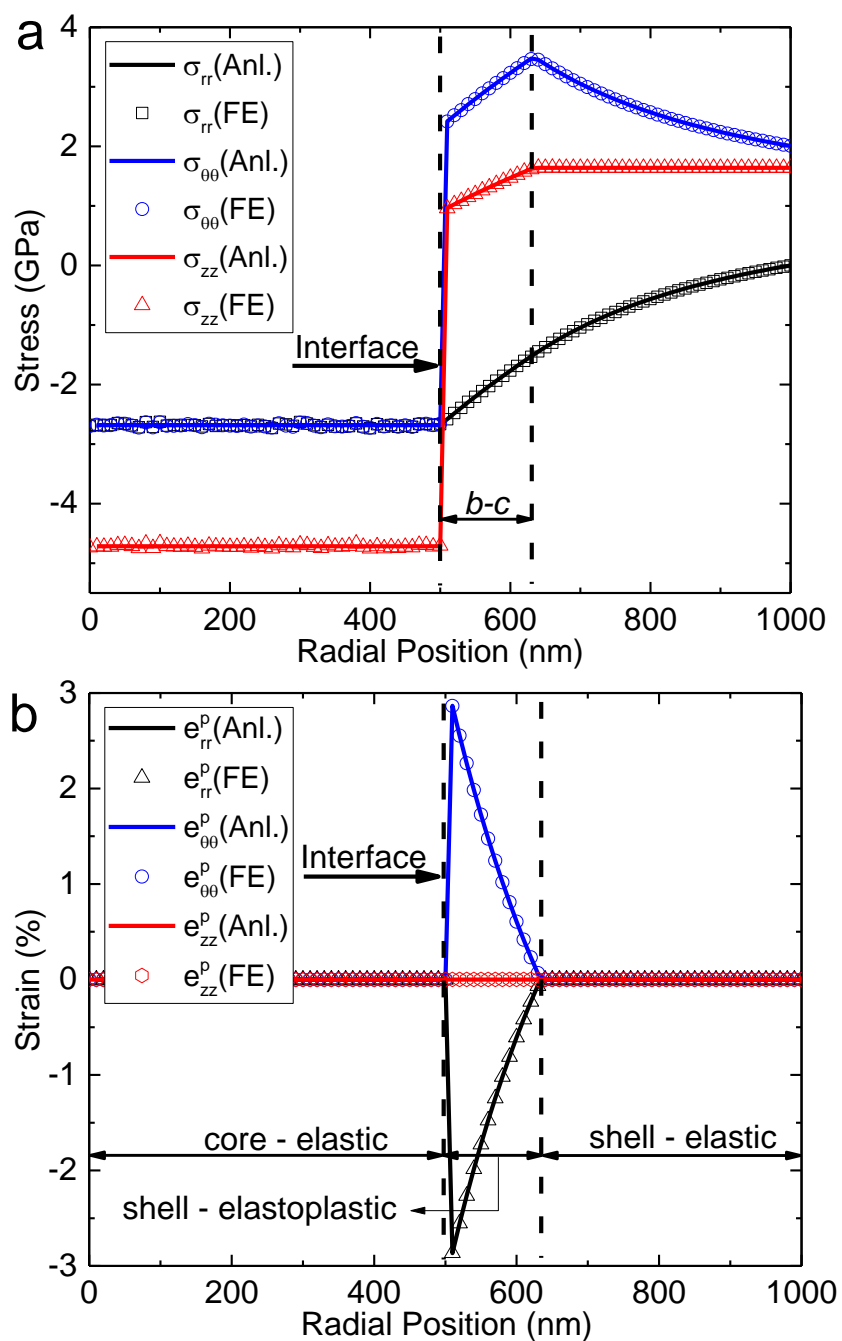


Fig. 6.3 (Color online) Comparison of a) stress components b) plastic strain components between analytical solutions (Anl.) and FE simulations. Radial position of zero nanometers corresponds to the center of the core and 1000 nm corresponds to the surface of the shell.

Tresca and Von Mises yield criteria are commonly used for plastic deformation. The Tresca criterion is more conservative whereas the Von Mises criterion in general shows a better agreement with experimental results. Due to nonlinearity of stress components in the Von Mises yield criterion, finding a closed-form analytical solution for the elastoplastic deformation in core-shell nanowire does not seem possible and therefore in my analytical approach I use the Tresca yield criterion. To show how the results will be affected if I use the Von Mises yield criterion instead of the Tresca yield criterion, I compare analytical results (which employ the Tresca yield criterion) with FE simulations (where in this case I employ the Von Mises yield criterion). Among the stress components shown in Fig. 6.4a, the largest difference between predicted values is observed for tangential component of stress ($\sigma_{\theta\theta}$). The magnitudes of stress components are affected by the choice of the yield criterion mainly in the elastoplastic region, but even in this region stress components follow the same qualitative trends. The Von Mises criterion predicts a smaller thickness $b-c$ of the plastic region, which is the thickness between the core-shell interface and the elastic region in the shell (Fig. 6.4b). Another difference between these two criteria is that the axial component of the plastic strain is predicted to be non-zero based on the Von Mises criterion, whereas it is equal to zero when the Tresca criterion is applied (Fig. 6.4b).

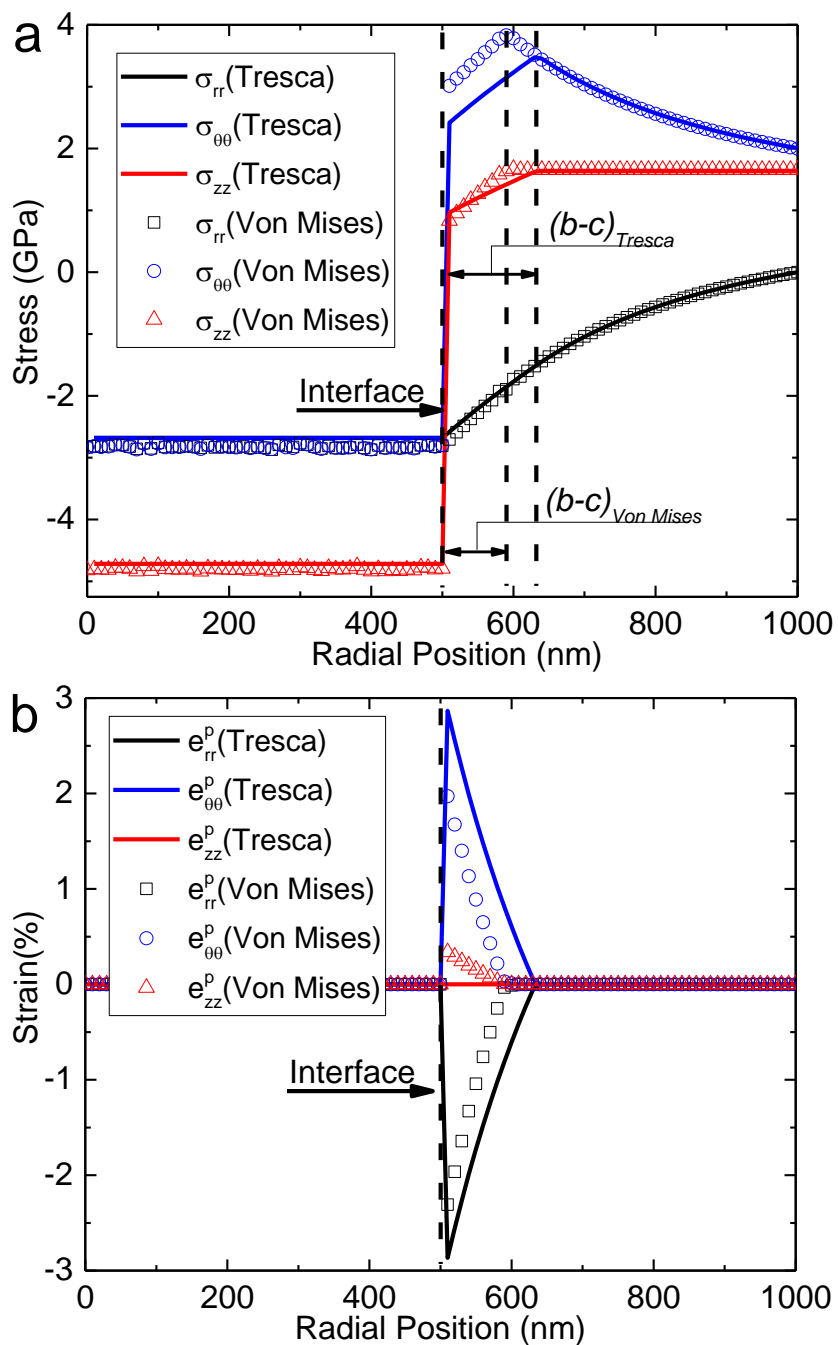


Fig. 6.4 (Color online) Von Mises vs. Tresca yield criteria: a) Stress field. b) Plastic strain field. Radial position of zero nanometers corresponds to the center of the core and 1000 nm corresponds to the surface of the shell.

The elastoplastic region in the core-shell nanowire is formed due to high misfit strain between core and shell. However, formation of this region is usually not desirable as it leads to deterioration of opto-electronic properties of devices. Using my newly developed analytical model, I wish to investigate the relationship between the thickness of the elastoplastic region and the geometry of the nanowire in order to determine if it is possible to minimize the thickness of the yielded region. In Fig. 6.5a, I plot the thickness of the elastoplastic region as a function of the core radius while the thickness of the shell is kept constant. A linear relationship between the thickness of the elastoplastic region and core radius is observed. Fig. 6.5a also shows that for a constant core radius, the thickness of the elastoplastic zone decreases as the shell thickness increases. Fig. 6.5b shows the change in the thickness of the elastoplastic region due to the change in the shell thickness for two different core radii. Regardless of the choice of the core radius, one can see an initial linear increase in the thickness of the elastoplastic region with increasing shell thickness. In this regime, the shell thickness is small enough so that the entire shell deforms plastically. By increasing the shell thickness, one can find critical values (points P and Q) after which the radius of the elastoplastic region starts to decrease with a further increase in the shell thickness. This critical shell thickness depends on the core radius as well as a number of material properties, such as elastic moduli and yield strength of core and shell. For instance, as shown in Fig. 6.5b the critical shell thickness for core radius of 1000 nm is about 270 nm whereas the critical value for nanowire with a smaller core radius (100 nm) is about 50 nm.

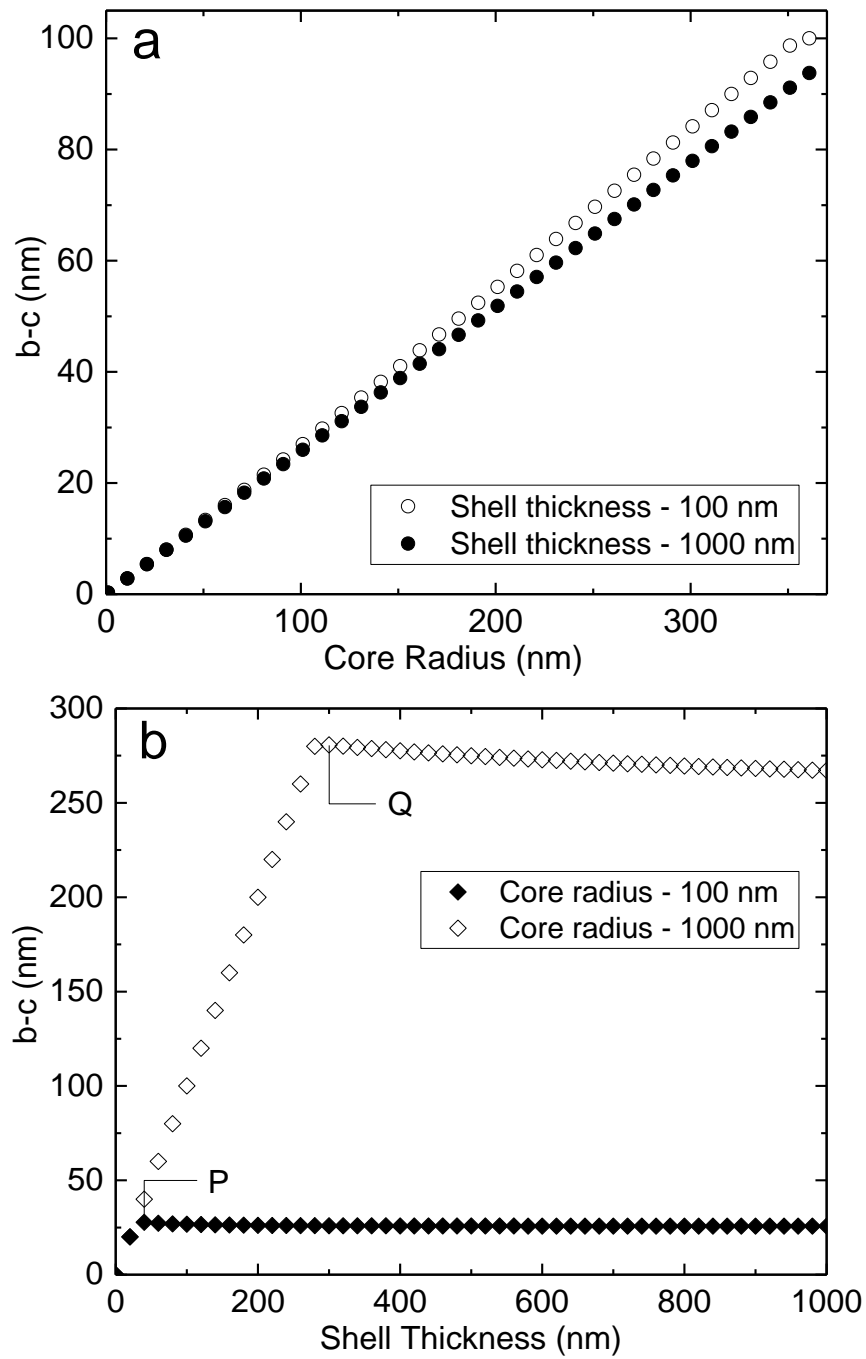


Fig. 6.5 Dependence of the thickness of the elastoplastic region ($b-c$) on a) the core radius, b) the shell thickness.

In Fig. 6.6a-b, I plot the thickness ($b-c$) of the elastoplastic region against χ , defined as the ratio of the shell thickness over the core radius. I report results for two different core radii. Similarly to Fig. 6.5b, two regimes are observed. In the first regime the thickness of the elastoplastic region increases linearly with χ and in the second regime the thickness decreases with χ and this decrease is non-linear. An interesting phenomenon that is observed here is that the critical ratio χ_{cr} (corresponding to the transition between the two regimes) has the same value for both core radii and it is equal to 0.29. This critical ratio does not depend on the nanowire geometry (core and shell thicknesses) and only depends on material properties of both the core and the shell. For instance, reducing the yield strength of the shell from 5 GPa to 3 GPa increases χ_{cr} from 0.29 to 0.66.

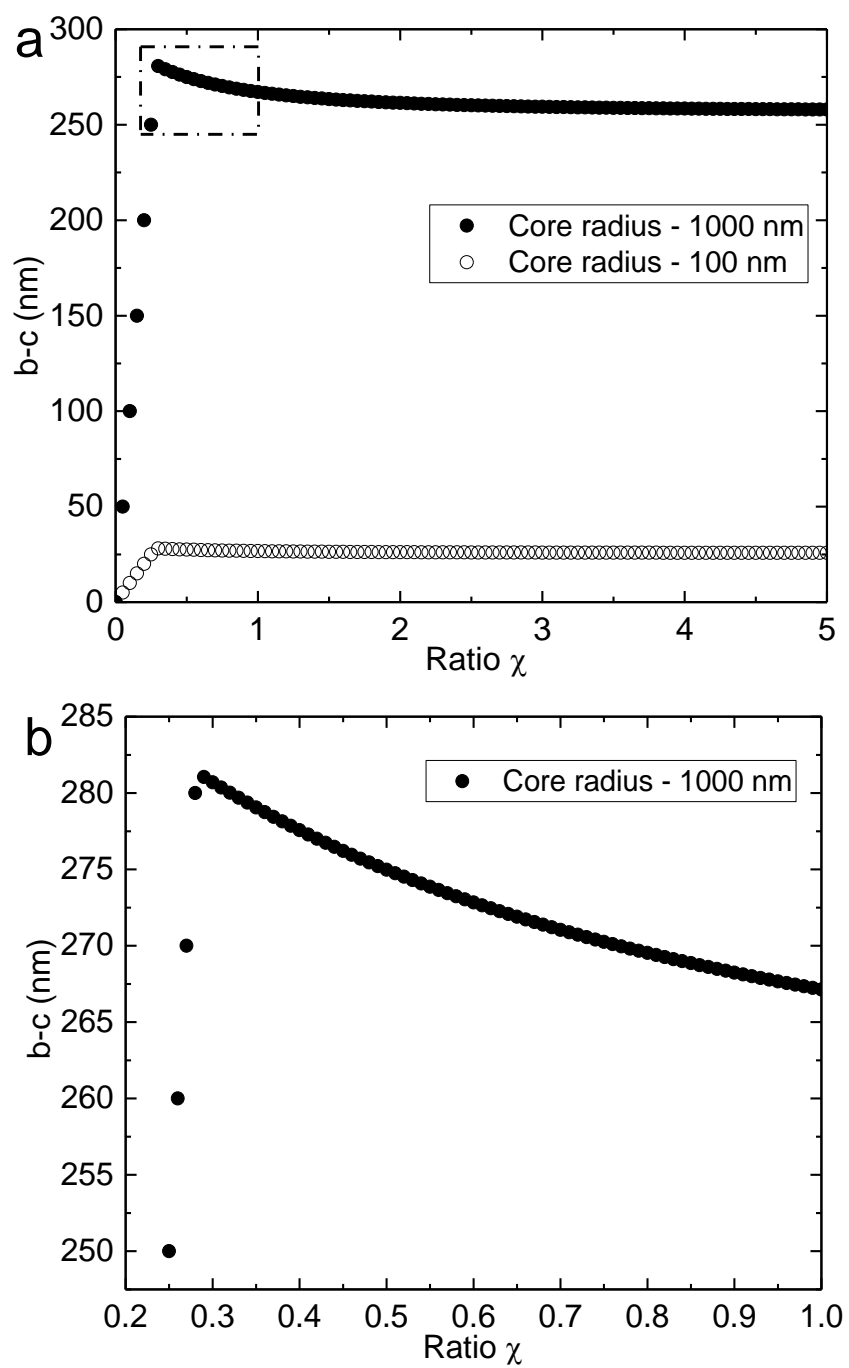


Fig. 6.6 Dependence of thickness of the elastoplastic region on the ratio χ (defined in text). a) χ varies between 0 to 5. b) χ varies between 0.25 to 1.

It is also interesting to ask what the effect of the nanowire geometry on the strain energy is. To understand that in Fig. 6.7a I plot the elastic and plastic strain energies per interfacial area (Eqs. (6-35 - 6-43)) as a function of χ . I find that the elastic strain energy increases with increasing χ (both in the core and the shell) whereas plastic strain energy decreases with χ . The increase of elastic strain energies with χ is nonlinear. Specifically, this increase is rapid at the beginning until $\chi \approx 1.5-2$ and then it levels off. For $\chi < 5$, elastic strain energy per unit area in the shell is larger in magnitude than the strain energy in the core. In the same regime of χ , plastic strain energy per interfacial area shows a decrease with χ , but the rate of this decrease is very small. For $\chi > 5$, the magnitude of elastic strain energy per unit area in the core is larger than the strain energy in the shell. In this regime, the rate of increase in elastic strain energy and decrease in plastic strain energy are very small. Strain energy density across a core-shell nanowire (along the radial direction) is plotted in Fig. 6.7b. The elastic strain energy density is constant throughout the core, which is consistent with the fact that both the stress field and the elastic strain field are constant in the core and there is no plastic deformation in this region of the nanowire. In the shell, both the elastic and the plastic strain energy densities vary nonlinearly with the radial position. Plastic strain energy density decreases with the radial distance from the core-shell interface and it reaches zero at the elastoplastic region boundary.

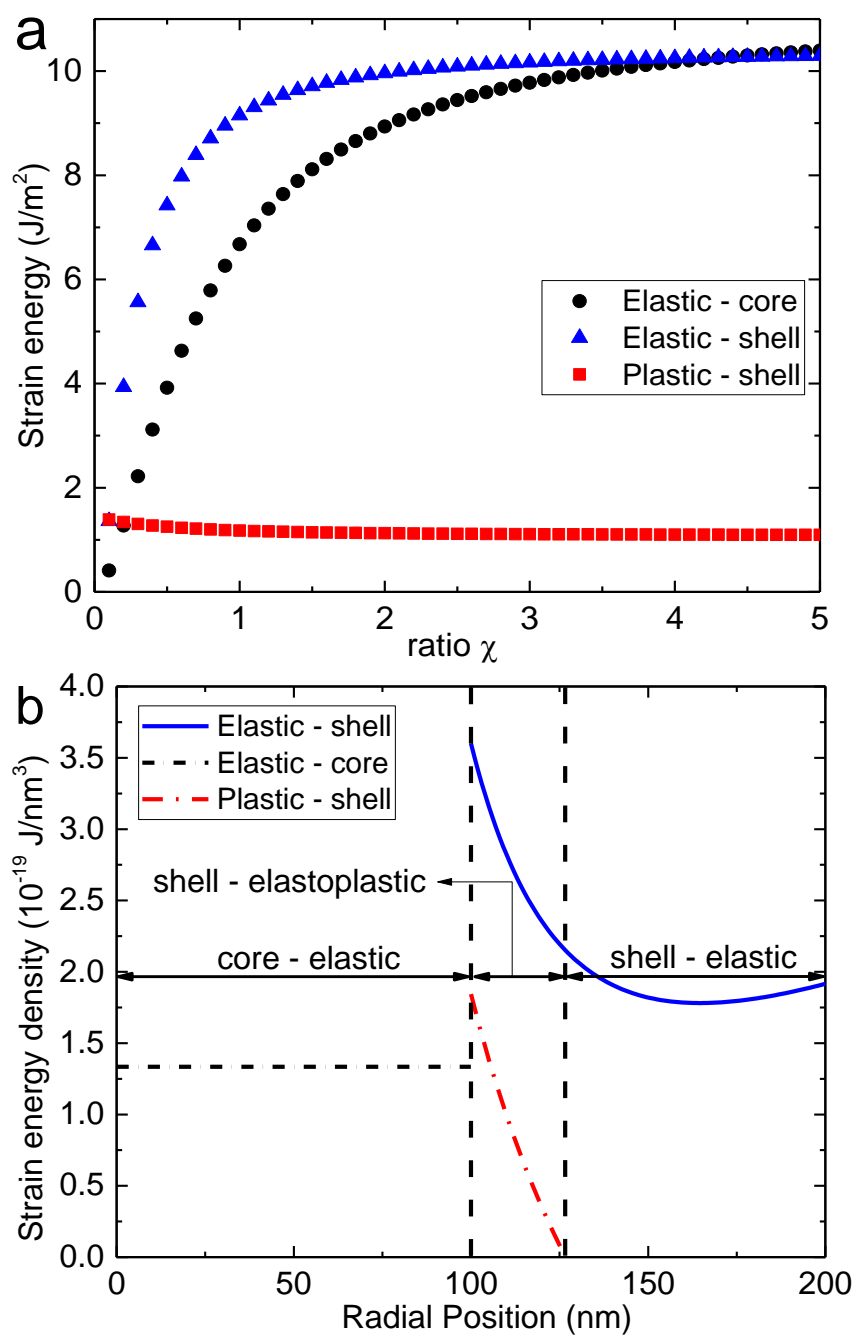


Fig. 6.7 (Color online) a) Dependence of strain energy per interfacial area on ratio χ (defined in text). b) Strain energy density across the nanowire. Zero radial position corresponds to the center of the core and 1000 nm corresponds to the surface of the shell.

Since the misfit energy depends on the specific choice of core and shell materials, it is instructive to consider the role of the misfit strain on the thickness of the elastoplastic region and on the strain energy stored in the nanowire. In Fig. 6.8a, I investigate dependence of thickness (b - c) of the elastoplastic region on the misfit strain. For small misfit strains (less than 0.04%), there is no plastic deformation. Increasing the misfit strain leads to a linear increase in the thickness of the elastoplastic regime. Strain energy per interfacial area shows a nonlinear dependence on the misfit strain, as illustrated for the case of $\chi = 1$ in Fig. 6.8b. Elastic strain energies (in the core and in the shell) increase nonlinearly and the energy in the core is larger than in the shell. Plastic strain energy per interfacial area is equal to zero for misfit strains smaller than 4% and then starts to increase nonlinearly with increasing misfit strain (Fig. 6.8b).

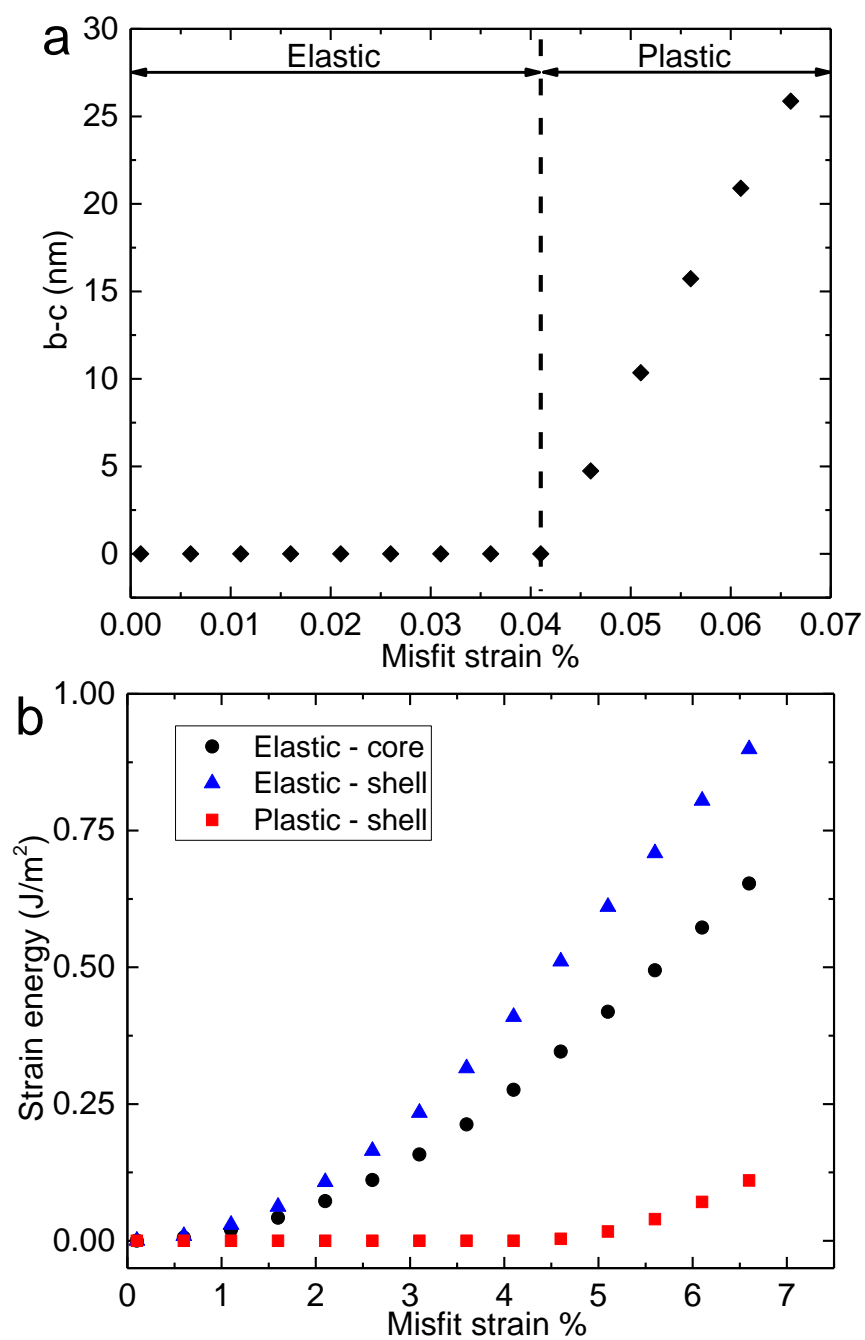


Fig. 6.8 (Color online) Dependence of a) the thickness of the elastoplastic region and b) strain energies on the misfit strain.

6.5 Conclusions

I developed an analytical model to study heteroepitaxially grown core-shell nanowires where the misfit strain between the core and the shell is large enough to produce plastic deformation in the shell. My model assumes infinitesimal strains and uses linear elasticity governing equations for the elastically deformed regions of the nanowire. For the elastoplastic regions, in addition to the linear elasticity governing equations I used the Tresca yield criterion with its associated flow rule and I assumed perfectly plastic behavior for the material (no work hardening). My results are validated against numerical simulations based on the elastoplastic FE analysis. Assuming InAs and GaAs as the core and the shell materials, respectively, I investigated the role of geometry (i.e., core and shell thicknesses) on the size of the elastoplastic zone. My results show that for a constant shell thickness, the elastoplastic region is larger for a larger core radius. Interestingly, I found that when the core radius is kept constant, there is a non-monotonic relationship between the shell thickness and the thickness of the plastically deformed region in the nanowire. For shell thickness up to a certain critical value, the entire shell has yielded plastically. By increasing the shell thickness above the critical value, the plastically deformed region shrinks, indicating that a thicker shell suppresses the amount of plastic deformation. In the case of InAs-GaAs core-shell nanowire, the critical ratio (shell thickness/core radius) of 0.29 maximizes the thickness of the plastically deformed region.

6.6 Reference

- [1] R. J. H. Morris, D. R. Leadley, R. Hammond, T. J. Grasby, T. E. Whall, and E. H. C. Parker, *J. Appl. Phys.* **96**, 6470 (2004).
- [2] S. F. Nelson, K. Ismail, J. O. Chu, and B. S. Meyerson, *Appl. Phys. Lett.* **63**, 367 (1993).
- [3] C. H. Hsueh, *J. Cryst. Growth* **258**, 302 (2003).
- [4] V. Pena, Z. Sefrioui, D. Arias, C. Leon, J. Santamaria, M. Varela, S. J. Pennycook, M. Garcia-Hernandez, and J. L. Martinez, *J. Phys. Chem. Solids* **67**, 472 (2006).
- [5] M. Arjmand, J. H. Ke, I. Szlufarska, *Comp. Mater. Sci.* **130**, 50 (2016).
- [6] M. Arjmand, J. Deng, N. Swaminathan, D. Morgan, and I. Szlufarska, *J. Appl. Phys.* **116**, 114313 (2014).
- [7] Z. Y. Zhang and M. G. Lagally, *Science* **276**, 377 (1997).
- [8] K. L. Kavanagh, J. Salfi, I. Savelyev, M. Blumin, and H. E. Ruda, *Appl. Phys. Lett.* **98**, 152103 (2011).
- [9] T. E. Trammell, X. Zhang, Y. L. Li, L. Q. Chen, and E. C. Dickey, *J. Cryst. Growth* **310**, 3084 (2008).
- [10] Y. Liang, W. D. Nix, P. B. Griffin, and J. D. Plummer, *J. Appl. Phys.* **97**, 043519 (2005).
- [11] R. X. Yan, D. Gargas, and P. D. Yang, *Nat Photonics* **3**, 569 (2009).
- [12] X. F. Duan, Y. Huang, Y. Cui, J. F. Wang, and C. M. Lieber, *Nature* **409**, 66 (2001).
- [13] X. F. Duan, C. M. Niu, V. Sahi, J. Chen, J. W. Parce, S. Empedocles, and J. L. Goldman, *Nature* **425**, 274 (2003).
- [14] M. C. McAlpine, H. Ahmad, D. W. Wang, and J. R. Heath, *Nat Mater* **6**, 379 (2007).
- [15] M. T. Bjork, B. J. Ohlsson, T. Sass, A. I. Persson, C. Thelander, M. H. Magnusson, K. Deppert, L. R. Wallenberg, and L. Samuelson, *Appl. Phys. Lett.* **80**, 1058 (2002).
- [16] M. W. Larsson, J. B. Wagner, M. Wallin, P. Hakansson, L. E. Froberg, L. Samuelson, and L. R. Wallenberg, *Nanotechnology* **18**, 015504 (2007).

- [17] C. M. Haapamaki, J. Baugh, and R. R. LaPierre, *J. Appl. Phys.* **112**, 124305 (2012).
- [18] O. Salehzadeh, K. L. Kavanagh, and S. P. Watkins, *J. Appl. Phys.* **114**, 054301 (2013).
- [19] Y. X. Zhao, Q. H. Fang, and Y. W. Liu, *Int J Mech Sci* **74**, 173 (2013).
- [20] M. Y. Gutkin, C. Enzevae, and H. M. Shodja, *Int J Solids Struct* **50**, 1177 (2013).
- [21] W. Koiter, *Quarterly of applied mathematics* **11**, 350 (1953).
- [22] E. Placidi *et al.*, in *Self-Assembly of Nanostructures: The INFN Lectures*, edited by Springer (2012).
- [23] S. Korte, I. Farrer, and W. J. Clegg, *J Phys D Appl Phys* **41**, 205406 (2008).

Chapter 7 **Concluding remarks and future directions**

7.1 **Implication of modeling on growth and annealing of heterostructures**

Modeling provides an important frame work to understand different strain induced phenomena in semiconductor heterostructures and to be able to control them. Here are my key findings:

- I found that different regimes during the growth of self-assembled islands are mainly controlled by strain and deposition flux.
- Surface induced compositional modulation in nanowires can be suppressed by thick coating around the core.
- Plastic deformation in heterostructures causes stress relaxation, specially at the interfaces.

7.2 **Possible improvements in future modeling efforts**

Here, I briefly discuss some of the ideas about future work of my research. The ideas are categorized in three groups based on the order of the chapters in this document.

1. Growth of thin films inside patterned surfaces:

- **3D model to study the growth of thin films inside surface patterns:** As shown in the thesis, I have used a plane strain assumption to study the growth of thin films. Although this assumption makes sense for the case that patterns are strip-shaped, but it does not consider any changes in some parameters such as diffusivity in the perpendicular direction to the cross-section. Hence a 3D model can elaborate more details about the growth of thin films and may provide some new understanding on how to control the morphology.
- **Study phase segregation in multi-component thin films during growth inside surface patterns:** many of the III-V semiconductors have miscibility gap in their phase

diagram. Depending on growth or annealing temperature, phase separation may also happen to relax bulk free energy or strain energy of the heterostructure. It will be interesting to study the coupling between phase segregation and strain relaxation during growth and investigate if this phase segregation plays any role to control the morphology.

2. Phase segregation in III-V nanowires during annealing process:

- **Study growth of nanowires:** Interesting phenomena have been observed during the growth of nanowires such as direction of the growth, stacking fault and instantaneous phase segregation during growth where there is no clear explanation for them. Given that phase field model can capture the effects of both thermodynamics and kinetics, it will be a good framework to investigate the growth of nanowires.
- **Study surface instability in core-shell nanowires:** Similar to thin films, morphological changes at the surface of nanowire heterostructures are one of the methods to relax the strain energy of the system. Given that nanowire heterostructures store less strain energy compared to thin films, it will be interesting to investigate the role of misfit strain and geometry on surface instabilities.

3. Analytical elastoplastic study of strain and stress fields in core-shell nanowires:

- **Investigate the role of different yield criterion, flow rule and hardening rule:** I have developed an analytical solution for elastoplastic deformation in nanowire heterostructures using Tresca yield criterion and its associated flow rule and assumed no work hardening. It will be interesting if one can analytically solve the governing equations for other yield criterion such as Von Mises and Hill and their associated flow rules. Also it will be interesting to find analytical solution for a work hardening material.

7.3 Papers and manuscripts

- **M. Arjmand**, J. Deng, N. Swaminathan, D. Morgan, I. Szlufarska, “Effects of confinements on morphology of $\text{In}_x\text{Ga}_{1-x}\text{As}$ thin film grown on sub-micron patterned GaAs substrate: Elastoplastic phase field model”. *J. of Appl. Phys.* 116, 114313 (2014)
- S. Yang, G. Luo, J. Li, **M. Arjmand**, I. Szlufarska, A. Brown, T. F. Kuech, D. Morgan, “First-principles Studies on the Molecular Beam Epitaxy Growth of $\text{GaAs}_{1-x}\text{Bi}_x$ ”. *Phys. Rev. B* 92, 035415 (2015)
- **M. Arjmand**, I. Szlufarska, “Control of surface induced phase separation in immiscible semiconductor alloy core-shell nanowires”. *Comput. Mater. Sci.*, 130 50 (2017)
- **M. Arjmand**, W. J. Drugan, I. Szlufarska, “Elastoplastic analysis of heteroepitaxial core-shell nanowires: Analytical study”. In preparation (2017)

7.4 Conference presentations

7.4.1 Oral presentations

- **M. Arjmand**, I. Szlufarska, “Stress relaxation in III-V Semiconductor Nanowires: Phase Segregation and Plastic Deformation” Oral, Stress Evolution in Thin Films and Coatings, Chicago, IL (2016)
- **M. Arjmand**, I. Szlufarska, “Elastoplastic study of incoherent semiconductor core-shell nanowires” Materials Research Society, Phoenix, AZ (2016)
- **M. Arjmand**, J. Deng, N. Swaminathan, D. Morgan, I. Szlufarska, “*Heteroepitaxial Growth Of Strained Thin Film In Sub-micron Patterned Substrates: An Elastoplastic Phase Field Model*”. Engineering Mechanics Institute conference, Stanford, CA (2015)

7.4.2 Poster presentations

- **M. Arjmand**, I. Szlufarska, “Growth of strained thin film heterostructures in sub-micron patterned substrates: an elastoplastic phase field model” Poster, Stress Evolution in Thin Films and Coatings, Chicago, IL (2016)
- **M. Arjmand**, I. Szlufarska, “Control of surface induced phase segregation in III-V semiconductor heterostructures” Poster, Materials Research Society, Boston, MA (2015)
- **M. Arjmand**, I. Szlufarska, “Control of morphology and phase separation of III-V semiconductor surface structures: Phase field approach” Poster, Gordon Research Conference, Portland, ME (2015)
- **M. Arjmand**, J. Deng, N. Swaminathan, D. Morgan, I. Szlufarska, “Effects of confinements on morphology of $\text{In}_x\text{Ga}_{1-x}\text{As}$ thin film grown on a patterned GaAs substrate”. Poster, Transformational Technologies in Molecular Simulations, Madison, WI (2014)